This is to certify that the
dissertation entitled

Poly(ethylene oxide) based polymer brushes:
Synthesis, properties and applications

presented by

Ying Zheng

has been accepted towards fulfillment
of the requirements for the

Ph.D. degree in Chemistry

Major Professor's Signature

23 August 2006

Date

MSU is an Affirmative Action/Equal Opportunity Institution

POLY(ETHYLENE OXIDE) BASED POLYMER BRUSHES: SYNTHESIS, PROPERTIES AND APPLICATIONS

By

Ying Zheng

A Dissertation

Submitted to
Michigan State University
in partial fulfillment of the requirements
for the degree of

DOCTOR OF PHILOSOPHY

Department of Chemistry

2006

ABSTRACT

POLY(ETHYLENE OXIDE) BASED POLYMER BRUSHES:

SYNTHESIS, PROPERTIES AND APPLICATION

By

Ying Zheng

Surface-initiated atom transfer radical polymerization (ATRP) of poly (ethylene glycol) methyl ether methacrylate (PEGMA) macromonomers from gold substrates leads to thin films of comb-like polymer brushes. Polymerization of these monomers in water resulted in essentially constant polymerization rates and yielded coatings with thicknesses as high as 400 nm. Polymers with side chains consisting of 22-23 ethylene oxide repeating units aligned to form crystalline polymers analogous to their non-brush analogs. However, polarized optical microscopy confirmed their crystallization as two-dimensional spherhulites, and the film morphologies, crystallization rates and lamellae orientations all depended on the film thickness. The crystallization rate decreased with the film thickness, as reflected by the film morphology changes. An Avrami analysis of growth rates indicated heterogeneous nucleation and one-dimensional growth. Both AFM images and reflectance FT-IR spectra of the films were consistent with crystalline lamellae preferentially oriented normal to the surface for brushes with thicknesses above 100 nm. As the film thickness decreased, the favored orientation shifted to crystalline lamellae parallel to the surface, with the PEO side-chains oriented perpendicular to the

surface. The lamellae orientations are related to polymer-surface interactions as well as to the "comb-like" polymeric structure.

Polymerizations were optimized to grow comb-like polymer brushes on flat surfaces and on silica nanoparticles. Kinetic studies of the growth of polymethacrylates with (PEG) polyethylene glycol segments of various lengths identified optimum polymerization condition for the growth of thick poly(PEGMA) films on planar substrates. These materials have potential utility as membranes, electrolytes for lithium ion batteries, and other applications.

Crosslinked brushes were grown from gold substrates by copolymerization of a macromonomer, poly(ethylene glycol) methyl ether methacrylate (PEGMA), and a crosslinker, bisphenol A ethoxylate dimethacrylate (BisA-EDMA) using surface-initiated ATRP. The crosslink density of the film was estimated from FT-IR measurements and from the aqueous swelling of the films, as measured by *in-situ* ellipsometry. These films show increased dimensional stability with cross-link while keeping high swelling in water. These crosslinked films are attractive for their mechanical stability and their ability to resist protein adsorption in biological applications.

Comb-like and crosslinked polymer brushes containing PEO segments were grafted on the surface of porous alumina membrane supports and the permeabilities of CO_2 and H_2 through the membranes were studied. These films are highly permeable to CO_2 and selectively permeate CO_2 with a CO_2 permeation coefficient as high as 300 Barrer and a CO_2/H_2 selectivity of 14 respectively for poly(PEGMA) film. The CO_2/gas permeability decreased for shorter PEG segments and for highly crosslinked films.

To My Family

ACKNOWLEDGMENTS

First, I would like to express my deep appreciation to my advisor, Professor Gregory Baker. Thank you for your guidance and constant encouragement, which built my confidence and enabled me to achieve my Ph.D. at Michigan State University. The polymer science knowledge, strict scientific attitude and initiative in research that I have learned from you will be invaluable in my future career. Professor Babak Borhan not only taught me good spectroscopic techniques and organic chemistry, but he also helped me in the first step of my Ph.D. studies in Baker's group. I greatly appreciate him for his trust and help. I learned from Professor Merlin Bruening a sincere approach to science and critical insight. I also like to thank Professor Peter Wagner for being my committee member.

I would like to give my thanks to all Baker group members: JB, Bao, Ping, Qin, Leslie, Feng, Xuwei, Jon, DJ, Erin and Sampa for useful discussions and for help in my research and my life. I also learned good surface science from Dr. Wenxi, and I enjoyed working with Lei, Tiffany, Matt and Anagi. I would like to thank all my friends for making my life in MSU enjoyable and memorable. Special thanks to Lisa Dillingham for her help during my stay in chemistry department, which made my life easier.

Finally, I want to thank my family. They have always been so supportive in every stage of my life. My life would not have been the same without their love and support. My dearest parents and my brother deserve my biggest thanks and love.

TABLE OF CONTENTS

LIST OF TABLES

Table **Page**

LIST OF FIGURES

Figure **Page**

LIST OF SCHEMES

Scheme **Page**

LIST OF ABBREVIATIONS

AFM	atomic force microscopy
AGET	activator generated by energy transfer
ATRP	atom transfer radical polymerization
BisA-EDMA	bisphenol A ethoxylate dimethacrylate (M_n =1,700g/mol)
bpy	bipyridine (or 2,2'-dipyridyl)
μCP	micro-contact printing
CRP	controlled radical polymerization
DMAEMA	dimethyl amino ethyl methacrylate
DMF	N, N-Dimethylformamide
DP	degree of polymerization
dNbpy	4,4'-di(5-nonyl)-2,2'-bipyridine
dnNbpy	4,4'-di(*n*-nonyl)-2,2'-bipyridine
DSC	differential scanning calorimetry
DPE	diphenylethylene
DPN	dip pen nanolithography
EDTA	ethylenediaminetetraacetic acid
EGDMA	ethylene glycol dimethacrylate
FESEM	field emission scanning electron microscopy
FT-IR	Fourier transform infrared spectroscopy
GMA	glycidyl methacrylate
GPC	gel permeation chromatography
GPS	3-glycidyloxypropyl trimethoxysilane
HEA	2-hydroxy ethyl acrylate
HEMA	2-hydroxy ethyl methacrylate
HMTETA	1,1,4,7,10,10-hexamethyltriethylenetetramine
k_p	propagation rate
k_t	termination rate
LCP	liquid crystalline polymer
LCST	lower critical solution temperature
LDPE	low density polyethylene
Me_4Cyclam	1,4,8,11-tetramethyl-1,4, 8,11-tetraazacyclotetradecane
Me_6TREN	*tris*[2-(dimethylamino)ethyl]amine
MA	methyl acrylate
MMA	methyl methacrylate
M_n	number average molecular weight
M_w	weight average molecular weight
NMP	nitroxide mediated radical polymerization
NMR	nuclear magnetic resonance
NPrPMI	N-propyl (2-pyridyl) methanimine
OEG	oligo(ethylene glycol)

PAA	poly(acrylic acid)
PCL	poly(ε-caprolactone)
PDI	polydispersity index calculated as M_w/M_n
PDMS	poly(dimethoxysiloxane)
PDMSA	Poly(3-(dimethoxymethylsilyl)propyl acrylate)
PEO	poly(ethylene oxide)
PEG	poly(ethylene glycol)
PEGMA	poly(ethylene glycol) methyl ether methacrylate, M_n= 300, 475, and 1100 g/mol
PEGDA	poly(ethylene glycol) diacrylate
PEGDMA	poly(ethylene glycol) dimethacrylate
PGMA	poly(glycidyl methacrylate)
PI	polyisoprene
PLA	poly(lactic acid) or poly(lactide)
PMEMA	poly((2-*N*-morpholino)ethyl methacrylate)
PMDETA	*N, N, N', N'', N'''*-pentamethyl diethylene triamine
PMMA	poly(methyl methacrylate)
PNIPAAM	poly(*N*-isopropylacrylamide)
PS	polystyrene
PtBA	poly(*tert*-butyl acrylate)
R_p	rate of polymerization
R_g	radius of gyration
RAFT	reverse addition-fragmentation transfer
ROP	ring opening polymerization
ROMP	ring opening metathesis polymerization
SAM	self-assembled monolayer
TEMPO	2, 2, 6, 6-tetramethyl-1-piperidyloxy
T_g	glass transition temperature
TGA	thermal gravimetric analysis
THF	tetrahydrofuran
T_m	melting point

Chapter I

Introduction to Polymer Brushes

Thin polymer films are useful for modifying surface properties. Common methods for the deposition of polymers on surfaces include spin and spray coating, however, physically adsorbed films are easily displaced by good solvents. In contrast, the chemical stability and mechanical robustness of polymer brushes have led to their widespread use for surface modification. The term "polymer brush" generally refers to an ensemble of polymer chains with each chain bound by one end to a surface or interface. The high tethering density forces the chains to stretch away from the surface or interface, resulting in a brush height greater than the polymer radius of gyration (R_g).[1,2]

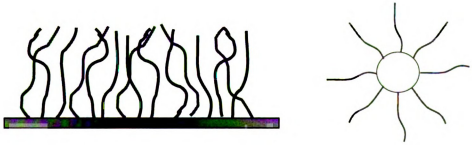

Figure 1.1. Polymer brushes on flat and curved surfaces.

In general, polymer brushes are covalently bound to surfaces by reaction of functional groups on polymer chains with surface reactive sites, or by selective adsorption of block copolymer segments that strongly interact with the surface. Non-covalently attached polymer brushes also suffer from poor stability in good solvents. This discussion will emphasize covalently bound polymer brushes.

Strategies for anchoring polymer brushes onto surfaces can generally be categorized as "*grafting to*" and "*grafting from*" methods (Figure 1.2).[3] The "*grafting to*" approach refers to tethering preformed polymer chains onto surfaces, which facilitates formation of polymer brushes with well-defined architectures. However, this method is limited in that it usually results in low polymer grafting densities and low film thickness due to the steric hindrance of previously attached polymer chains. In contrast, the "*grafting from*" method involves attaching initiators on the surface, and initiating polymerization of monomers from the surface. Since the only limit to the polymer chain propagation is the diffusion of monomers to the surface reactive sites, this method usually generates thicker polymer films with higher grafting densities than the "*grafting to*" approach.[4]

The "*grafting from*" method is also called surface-initiated polymerization. In order to achieve a high degree of control over the polymer brush architecture, the use of controlled polymerizations[5, 6] to provide well-defined polymers with low polydispersity (PDI) is highly desirable. Controlled surface-initiated polymerizations offer several advantages when forming well-defined dense and thick films including: 1) good control over the film thickness by controlling the polymerization time, 2) simplified separation and purification issues since the active radicals are confined on the surface and no polymers are formed in solution, eliminating the need for exhaustive extraction,[7] 3) tunable grafting densities by controlling the surface coverage of the initiator,[8] 4) the ability to simultaneously grow polymer chains from multifunctional cores or surfaces, and 5) the ability to control brush architectures, ranging from linear tethered polymers, graft (comb-like) copolymers, hyperbranched (star-like or dendritic) polymers, to cross-

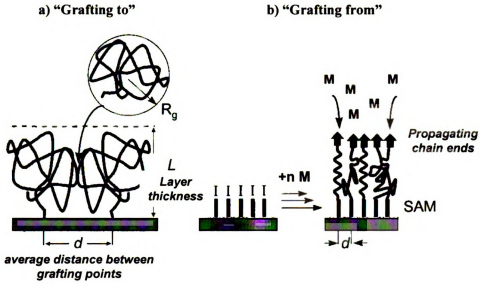

Figure 1.2. "Grafting to" (a) and "grafting from" (b) methods for the generation of polymer brushes. Adapted with permission from *J. Am. Chem. Soc.* **1999**, *121*, 1016-1022. Copyright ©1999 American Chemical Society.

linked polymer networks. Surface-initiated polymerization also provides good control over the "vertical" compositions of tethered linear polymers (normal to the surface) through the growth of block copolymers. Polymer brushes with varying compositions and dimensions have been prepared by their controlled growth from flat surfaces (gold, silica wafers, and glass slides), non-planar surfaces (gold, silica, latex particles, magnetic beads, polystyrene particles, carbon nanotubes), porous supports, chromatography media, and other materials.[9,10]

The physical properties of polymer brushes largely depend on the grafting densities, polymer chain lengths and flexibility, as well as the brush architecture. Polymer brushes have potential applications in many areas and they can greatly affect surface properties such as wettability and adhesion. Polymer brushes function as "smart" surfaces that are responsive to the environmental stimuli,[11-13] barriers for chemical etching,[14-16]

layers resistant to adsorption of cells and biomolecules,[17] dielectric layers in electronic device,[18] and other applications.

Atom transfer radical polymerization (ATRP) is one of the most popular controlled polymerization methods due to its simplicity and functional group tolerance.[19-21] ATRP also is a versatile technique for preparing well-defined (co)polymer films. In addition, ATRP of various monomers from preformed functional surfaces or colloidal initiators has provided polymer brushes with precise dimensions and functionalities. The nanoscale features or nano-objects in these films are typically characterized by various techniques, such as ellipsometry, contact angle measurements, and atomic force microscopy (AFM).

Synthesis of polymer brushes by surface-initiated polymerization

Surface-initiated polymerization generally includes anchoring initiator on the surface followed by the polymerization of monomer from the initiator. Initiators can be anchored to surfaces using well-known chemistry including the formation of self-assembled monolayers (SAM), such as thiols self-assembled on gold surfaces, silylation of silicon or glass surfaces, or by plasma treatment of substrates to directly form initiating species on polymer surfaces.

Different types of surface-initiated polymerizations have been reported, including anionic,[22-27] cationic,[28-30] conventional free radical,[31, 32] ring opening metathesis polymerization (ROMP),[33-36] and ring-opening polymerization (ROP).[37-39] Of these, controlled radical polymerization (CRP) is prominent due to its broad functional group tolerance compared to anionic and cationic polymerizations, and its ability to form polymers with high molecular weight and a PDI usually less than 1.5. Conventional

anionic polymerizations are the prototype living polymerization, but anionic polymerizations from surfaces have slow growth rates (usually days to generate a 100 nm film), and the polymerization system is sensitive to oxygen, moisture and impurities. Living cationic polymerization also can generate complex polymer architectures and polymers with low PDIs. However, the film growth rates for surface initiated cationic polymerizations are even slower than their anionic analogs, and also quite sensitive to moisture and other impurities. Much faster polymerization rates and films of predictable thicknesses are provided by traditional free radical polymerizations from surfaces, however free radical polymerization is incompatible with formation of certain architectures such as block copolymers. By maintaining a low concentration of active radicals in the system to suppress termination reactions, CRPs provide the advantages characteristic of living systems such as anionic and cationic polymerization. ATRP is tolerant of many functional groups and impurities, and because it is relatively easy to implement, it is the most popular CRP methodology for the controlled synthesis of polymer brushes. ROP has been used for preparing many commercially important polymers such as poly(ε-caprolactone) (PCL) and polylactide (PLA). Strained cyclic monomers such as norbornenes are polymerized by ROMP. Some examples of surface-initiated polymerizations will be provided before the discussion of surface-initiated ATRP.

Surface-initiated living anionic and living cationic polymerizations

Due to its lack of chain transfer and termination reactions, anionic polymerizations provide the best possible control over polymer architectures. Surface-initiated anionic polymerization has been used to grow polymer brushes from various

small particles such as silica gel, carbon black, and silicon wafers. However, the challenge of using anionic polymerization is its stringent polymerization conditions, slow film growth rates, and the limited range of monomers that are compatible with anionic polymerizations. Jordan *et al.*[24] used lithiated biphenyl SAMs and initiated the polymerization of styrene from gold substrates, obtaining uniform 18 nm thick films after a three-day reaction. Later, Advincula *et al.*[22] activated diphenylethylene (DPE) SAMs with *n*-butyllithium to initiate anionic polymerization of styrene. A 5-day reaction gave a polystyrene (PS) film only 23 nm thick. However, the formation of polystyrene-*block*-polyisoprene (PS-*b*-PI) copolymer brushes demonstrated the living nature of the polymerization. Polymer brushes have also been grown from DPE derivatives anchored through quaternary ammonium tethers to clay surfaces. Zheng *et al.*[25] grafted polybutadiene brushes to the surface of PS nanoparticles, and reported that the grafting density and degree of polymerization greatly affect the dispersion of nanoparticles in matrices and the mechanical properties of nanocomposites. Foster[26] used DPE-containing SAMs to generate polyisoprene-*block*-poly(ethylene oxide) (PI-*b*-PEO) block copolymer brushes from silicon surfaces, creating a hydrophilic surface by introducing the PEO block. Again, only thin films (24 nm) were obtained. Recently, Advincula *et al.*[27] grew 14 nm thick PEO homopolymers and polyisoprene-*block*-poly(methyl methacrylate) (PI-*b*-PMMA) copolymer brushes on gold surfaces. From these examples, we see that the traditional monomers used for anionic polymerizations can be applied to surface-initiated polymerization, however, obtaining thin films after long reaction times restricts broader application of anionic polymerization to the synthesis of polymer brushes.

Figure 1.3. Examples of polymer brushes grown by living anionic polymerization.

a)

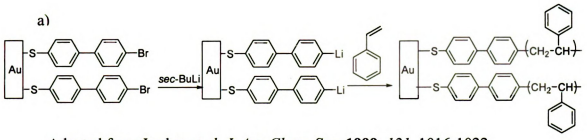

Adapted from Jordan *et al. J. Am. Chem. Soc.* **1999**, *121*, 1016-1022.

b)

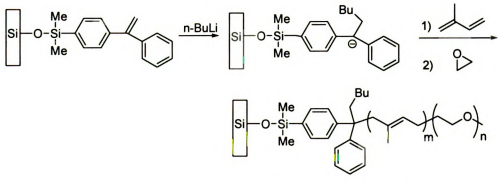

Adapted from Foster *et al. Macromolecules* **2002**, *35*, 9964-9974.

c)

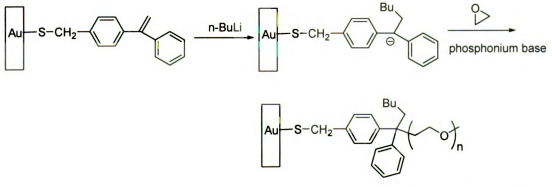

Adapted from Advincula *et al. J. Polym. Sci. A: Polym. Chem.* **2006**, *44*, 769.

Little work has been reported on the growth of polymer brushes using cationic polymerization. Ulman *et al.* reported surface-initiated cationic polymerization of 2-oxazolines from gold coated wafers[28] and gold nanoparticle surfaces.[29] Figure 1.4 shows the synthetic pathway used to obtain amphiphilic polymer brushes using this chemistry.

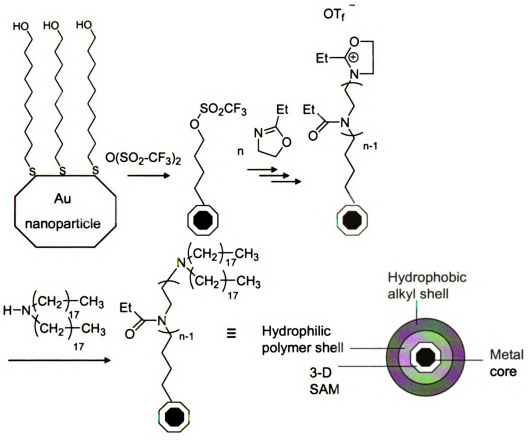

Figure 1.4. Scheme showing the surface-initiated polymerization of 2-oxazolines for the preparation of the amphiphilic nanocomposites, with 2-ethyl-2-oxazoline and *N,N*-di-*n*-octadecylamine used as monomer and terminating agent, respectively. Adapted with permission from *Macromolecules*, **2001**, *34*, 1606-1611. Copyright © 2001 American Chemical Society.

Zhao *et al.*[40] synthesized 30 nm thick PS brushes in one hour from cumyl methyl ether groups attached to SAMs on silicates. The reaction was carried out at -78 °C to suppress the chain transfer reactions characteristic of cationic polymerizations.

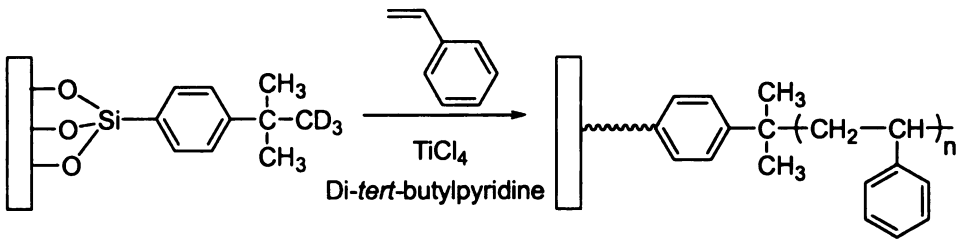

Figure 1.5. Polymer brushes grown by living cationic polymerization.

Surface-initiated ring opening metathesis polymerization (ROMP)

Surface-initiated ROMP is well suited for the polymerization of functionalized norbornenes, and as shown in Figure 1.6, has been demonstrated on Au, SiO_2 and Si surfaces using Grubbs-type catalysts (Cat-**1** and Cat-**2**) linked to surfaces by various molecules (SAM-**1**, **2**, **3**). Whitesides *et al.*[33] used a surface-immobilized Grubbs-type ROMP catalyst to grow functionalized polynorbornenes. They reported the rapid, controlled growth of 90 nm thick brushes polymer brushes in 30 min, and also formed diblock copolymer brushes by exposing the brushes to a second monomer solution. The same strategy was utilized by Moon *et al.*[34] to form brushes from polymers with poly(*p*-phenylene ethynylene) side chains for chemical sensing applications. Although very thin films (10 nm) were obtained, the brush fluorescence was brighter than comparable spin-cast films, which was attributed to reduced aggregation of polymer chains.

Figure 1.6. Surface-initiated ROMP applied to the synthesis of norbornene-based polymer brushes

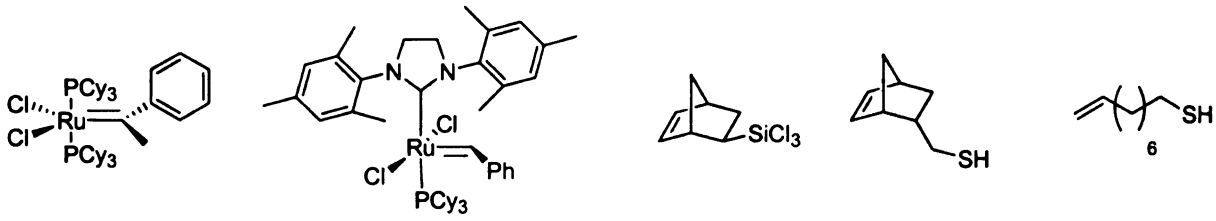

Cat-1 **Cat-2** **SAM-1** **SAM-2** **SAM-3**

a)

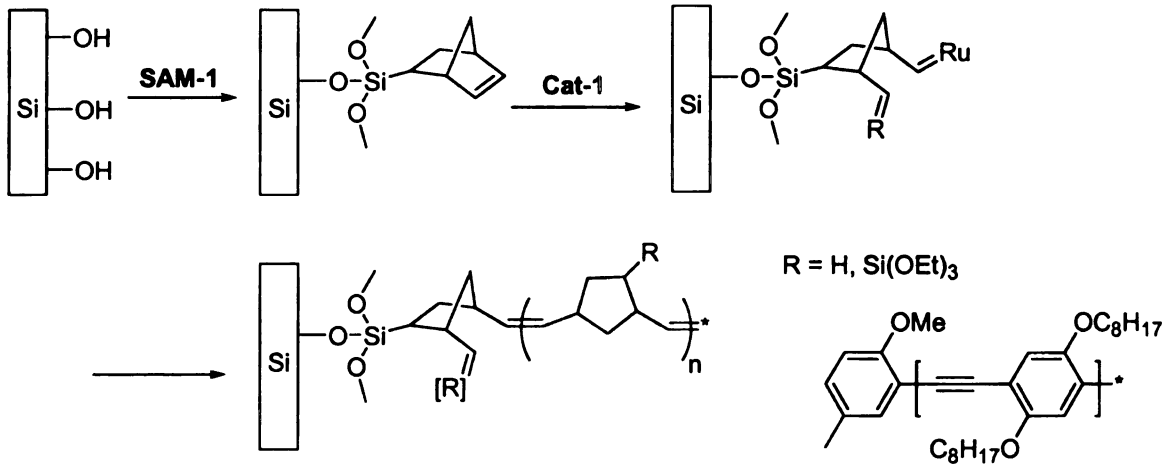

Adapted from Whitesides *et al. Macromolecules* **2000**, *33*, 2793-2795 and Moon *et al. Macromolecules* **2002**, *35*, 6086-6089.

b)

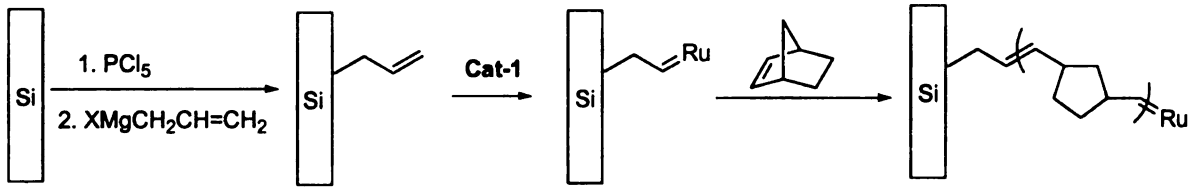

Adapted from Grubbs, R. H. *et al. Langmuir* **2001**, *17*, 1321-1323.

Grubbs *et al.*[35] directly attached initiators through a Si-C bond to a Si (111) surface, providing a link between the polymer and a Si wafer without the insulating SiO_2 layer. By varying the monomer concentrations, they obtained brush thickness ranging from 0.9 nm to 5 μm.

ROMP has been coupled with other techniques to form nanopatterned functionalized surfaces. Mirkin *et al.*[36] combined dip-pen nanolithography (DPN) and ROMP to form polymer brush arrays on the nanometer length scale. The novelty of this approach is that combinatorial polymer brush arrays can be formed by controlling the tip and substrate reaction time and different monomers can be used for polymerization.

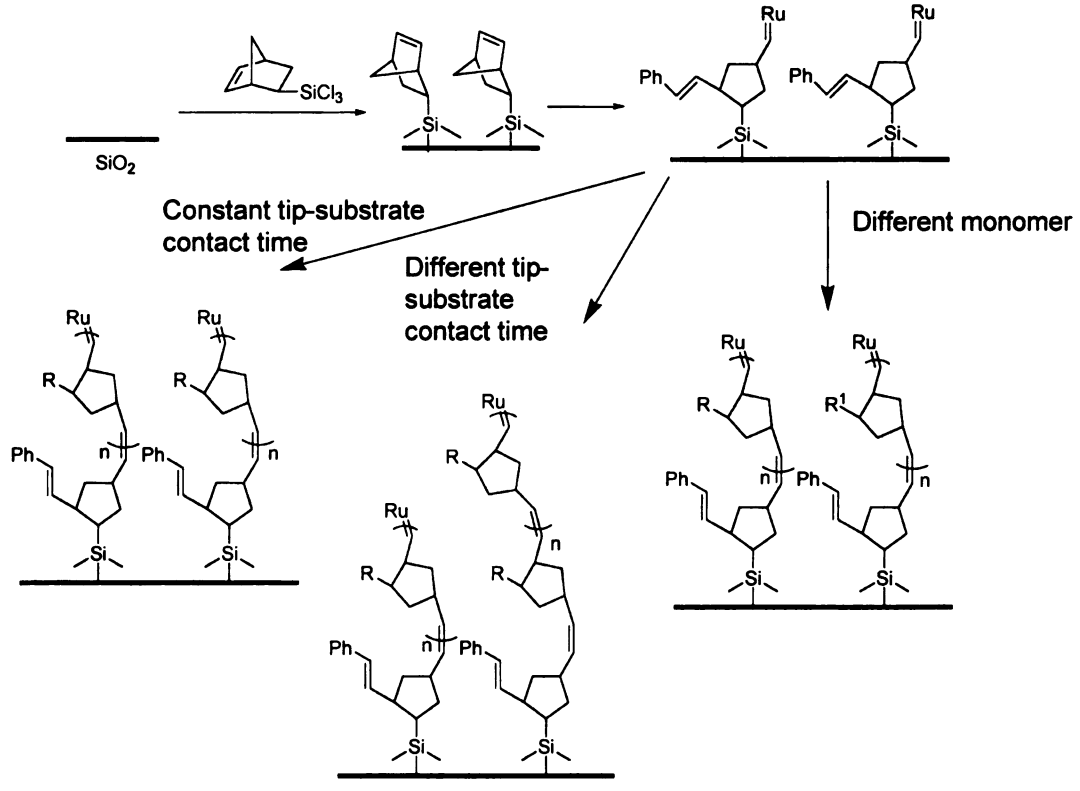

Figure 1.7. Graphic representation of ROMP initiated by DPN and a monomer coated AFM tip. Adapted with permission from *Angew. Chem., Int. Ed.* **2003**, *42*, 4785-4789. Copyright © 2003 Wiley Intersciences.

Surface-initiated ring opening polymerization (ROP)

Surface-initiated ROP has been applied to the synthesis of poly(*N*-propionylethyleneimine), PCL, PLA, and polyglutamate brushes.[3] Figure 1.8 shows examples of the polymerization of ε-caprolactone and L-lactide initiated from SAMs terminated with ethylene glycol.

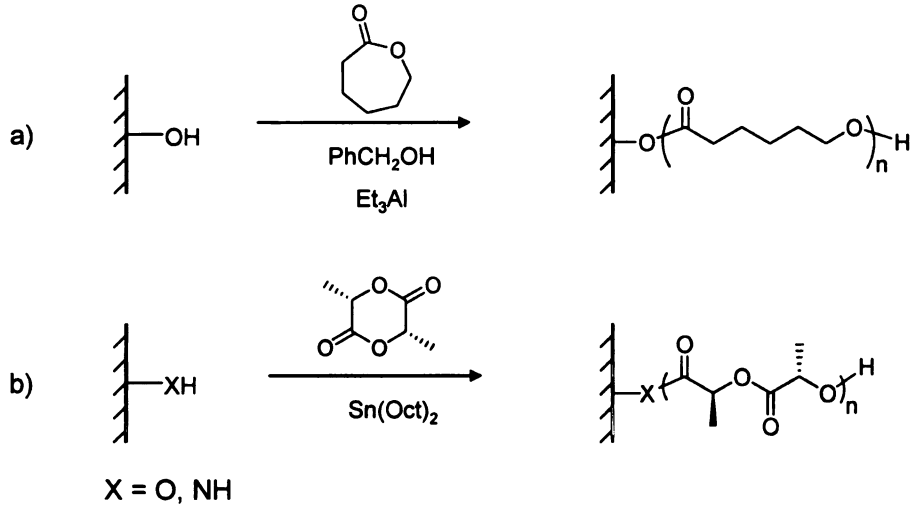

Figure 1.8. PCL and PLA brushes formed by surface-initiated ROP.

Husseman *et al.*[37] grew PCL from gold using aluminum alkoxide-catalyzed ROP. Brushes up to 70 nm thick formed in a few hours using a diethylaluminum alkoxide based catalyst; the concurrent formation of polymers in solution required exhaustive washing of the substrates to remove adsorbed polymer. SAMs terminated with oligo(ethylene glycol) (OEG) was also used to initiate polymerization of lactide,[38] however, the growth rate was slow, with a three day polymerization at 40 °C yielding a 12 nm thick film. The use of amine-terminated SAMs on SiO_2 were also investigated, and

70 nm thick PLA brushes were grown in three days at 80 °C. Kim *et al.* reported the polymerization of lactide from poly(2-hydoxyethyl methacrylate) (poly(HEMA)) brushes at 95 °C using $Sn(2\text{-ethylhexanoate})_2$ as the catalyst.[41] In this example, the terminal OH groups on the poly(HEMA) side chains initiated the ROP of lactide. Despite the use of a gold substrate, the film was stable at the polymerization temperature due to partial crosslinking of poly(HEMA) as a result of transesterification.

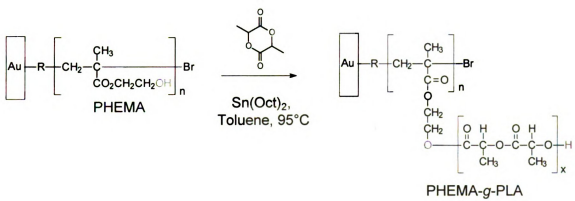

Figure 1.9. Synthesis of poly(HEMA)-*g*-(polylactide).

Joubert *et al.*[39] recently reported the first example of grafting PEO to silica nanoparticles using surface-initiated ROP of oxirane monomers. The silica particles were first treated with pre-hydrolyzed 3-glycidyloxypropyl trimethoxysilane (GPS) to form particles with grafted alcohols, which acted as a co-initiator/chain-transfer reagent in the polymerization.

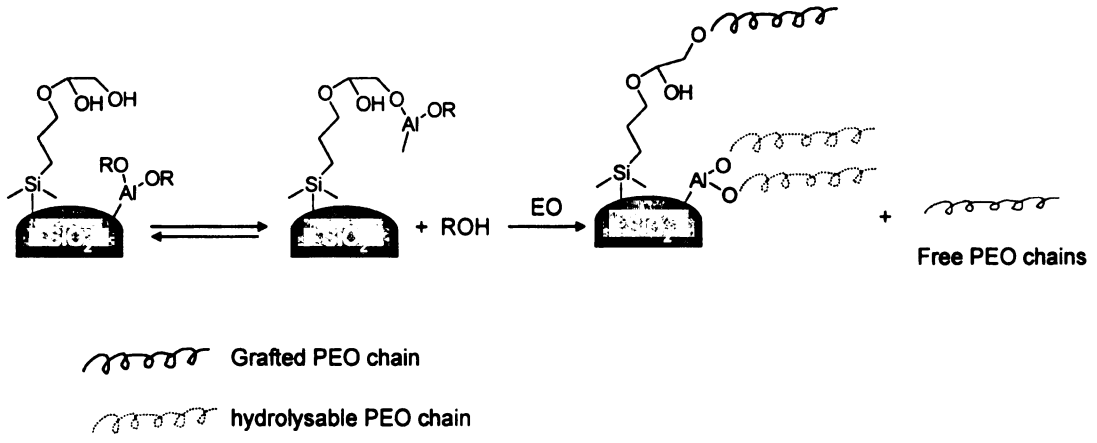

Figure 1.10. Synthetic strategy for the anionic ring-opening polymerization of ethylene oxide initiated from a silica surface modified by $Al(OiPr)_3$/GPS.

Surface-initiated controlled radical polymerization (CRP)

Over the past decade, a variety of CRP methods have been developed and blossomed. A major difference between traditional free radical polymerization and CRP is the lifetime of active radicals. In traditional radical polymerizations, active radicals are formed, add to monomers (propagate), and terminate. In CRP, the low concentration of active radicals greatly extends the lifetime of a growing polymer chain due to a dynamic equilibrium between the dormant species and active radicals. Although the details of the various types of controlled radical polymerizations are different, the general principle is still the same.[19] As shown in Scheme 1.1, the covalent bond of the dormant species is homolytically and reversibly cleaved by physical (heat or light) or chemical (metal catalysts) methods to generate a reactive radical, which adds to monomers to form polymer chains. The low concentration of growing radicals is maintained by fast

reversion to the dormant species, which greatly reduces the chances of bimolecular radical coupling and disproportionation reactions. This equilibrium exists in every propagation step resulting in uniform polymer chains.

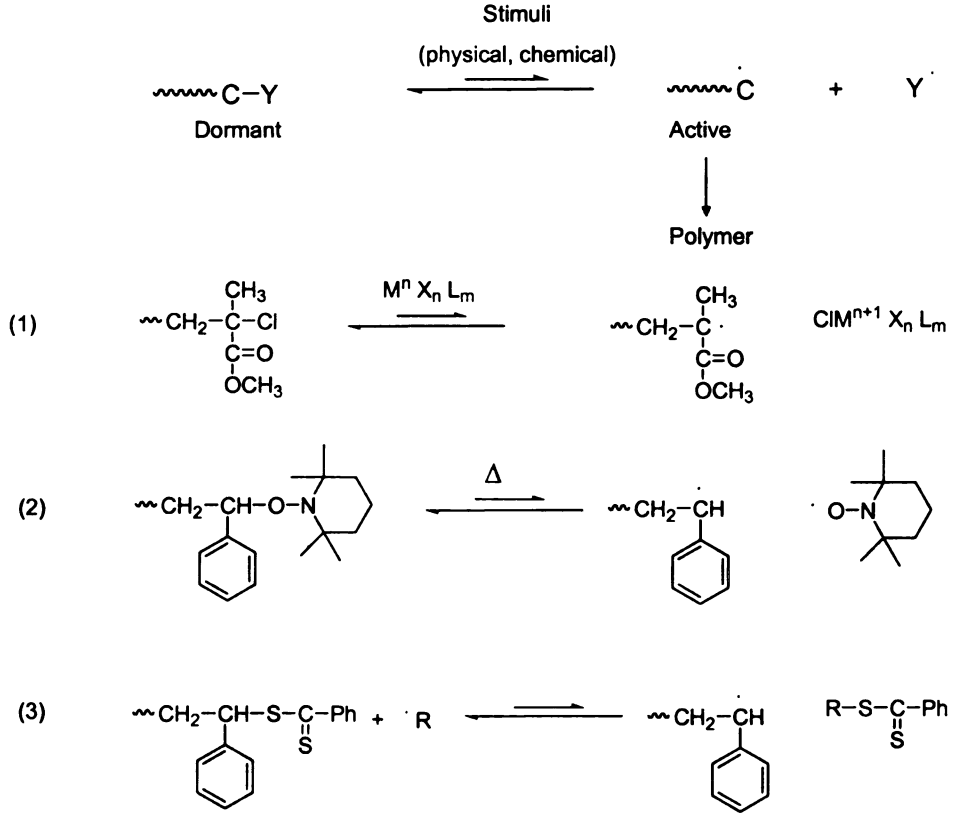

Scheme 1.1. The general mechanism of controlled radical polymerization and some typical examples.

Metal-catalyzed living radical polymerization, (ATRP)[20] (1), nitroxide mediated polymerization (NMP)[5] (2), and reverse addition fragmentation transfer (RAFT)[42] (3) are the most extensively used controlled radical polymerizations since they provide good control over the polymer architecture, are compatible with a broad range of monomers and polymerization conditions, and the chemicals used in the polymerization are readily

accessible. Each method has its own advantages as well as limitations.[43] NMP has been successfully applied only to styrene and styrene derivatives, and usually provides poor control in the polymerization of acrylates and methacrylates. High temperatures are usually required when the 2,2,6,6-tetramethyl-1-piperinyloxy (TEMPO) free radical is used for NMP, because of the strength of the C-O bond between TEMPO and the growing chain end. In addition, alkoxy amines are usually difficult to remove from the chain end, which limits its conversion to other functional groups. The advantage of NMP is that it does not use metal catalysts, which often cannot be completely removed from polymerizations. In theory, RAFT can be applied to all radical polymerizations. However, high temperatures (>140 °C) are required for RAFT of vinyl esters, and the residual thioester end groups can cause odor problems in low molecular weight species. Development of improved transferable groups for RAFT is desirable. ATRP has been applied to largest number of monomers and over a wide temperature range (-20 to 130 °C). Since the polymer end group is a halogen, it can be easily converted to other functional groups. Some tolerance to oxygen and compatibility with water makes ATRP probably the most popular CRP method. However, the biggest challenge for ATRP is to solve the challenge of removing/recycling the metal catalysts, which impedes its wide application in biotechnology and for industrial syntheses of polymers. A detailed discussion of ATRP appears in the following section.

Andruzzi *et al.*[44] reported the use of surface-initiated NMP to grow polymer brushes with pendant OEG segments from a silica surface. The monomers were styrene derivatives with pendent OEG units, and were polymerized at 125 °C for 48 h. The as-formed polymer brushes were used to study protein adsorption and cell adhesion.

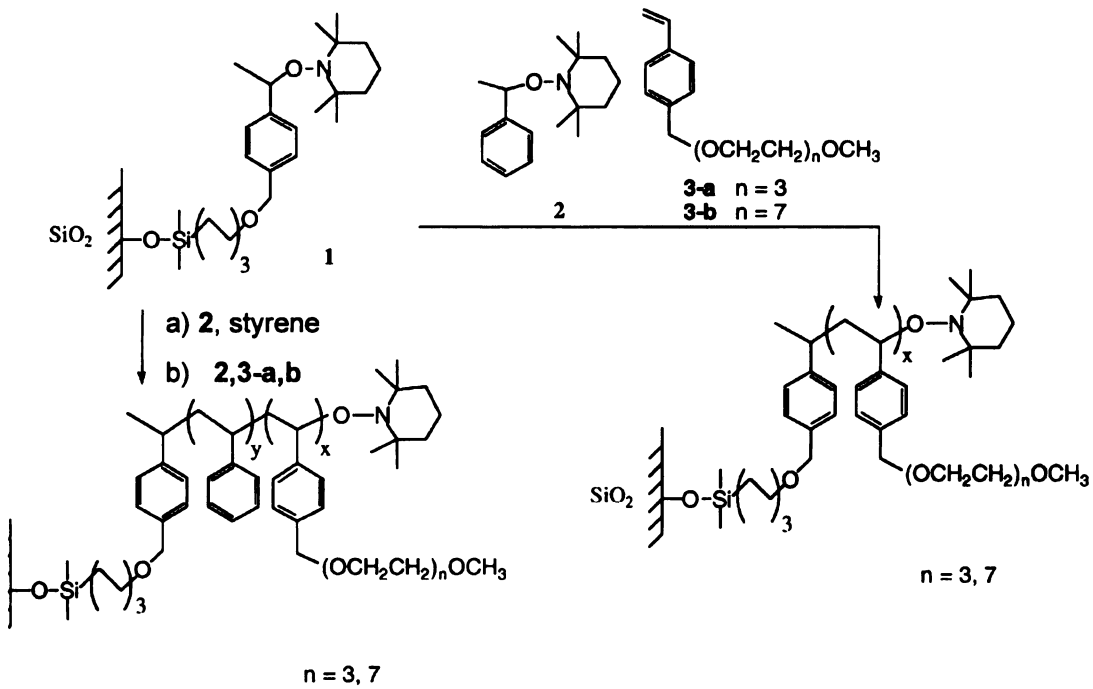

Figure 1.11. Synthesis of tethered OEG containing polymer brushes on silica surfaces.

Atom Transfer Radical Polymerization (ATRP)

The general mechanism of ATRP is shown in Scheme 1.2. The terminal halogen atom of the initiator (R-X) is extracted by a metal catalyst, such as a Cu^I complex, during initiation to form a reactive radical. This process occurs with a rate constant of k_{act} and the reverse reaction occurs with a rate constant k_{deact}. The reactive radical will add to monomers to form a polymer just as in traditional free radical polymerization, with the propagation rate k_p. The advantage of ATRP is the low concentration of reactive radicals in the polymerization system, which is maintained by the equilibrium between the reactive radical and dormant species ($K_{eq} = k_{act} / k_{deact}$). Since $k_{deact} > k_{act}$, the equilibrium favors the dormant species. Termination (k_t) also occurs in ATRP, mainly by bimolecular

coupling or disproportionation. However, if the radical concentration is sufficiently low, termination can be ignored. Therefore, a successful ATRP will yield polymers with high molecular weight and low PDI.

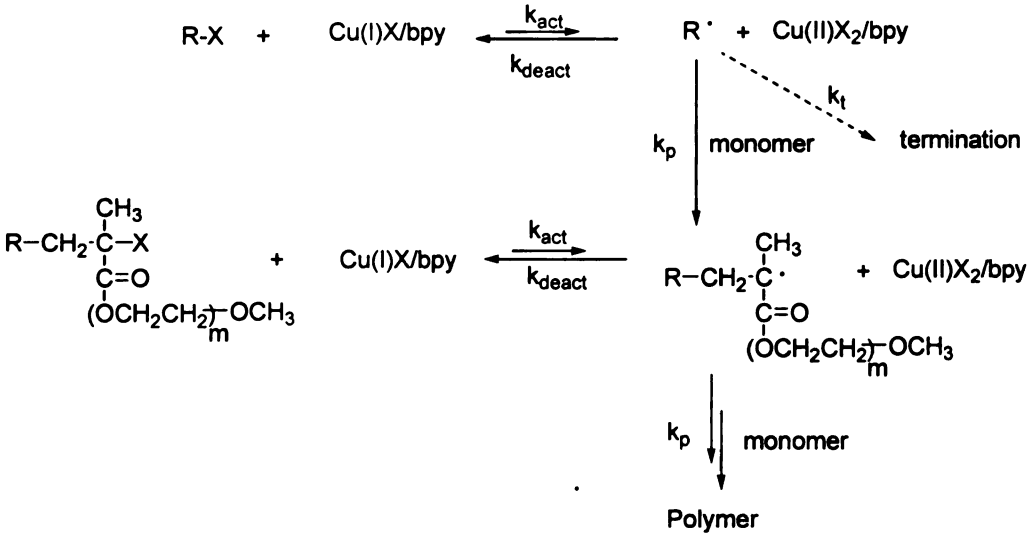

Scheme 1.2. The mechanism of ATRP of poly(ethylene glycol) methyl ether methacrylate (PEGMA).

ATRP kinetics

For copper-mediated ATRP, the polymerization rate (R_p) can be described as[45]

$$R_p = k_p K_{eq}[M][I]_0 \frac{[Cu^I]}{[XCu^{II}]} \qquad \text{Eq. 1}$$

where $K_{eq} = k_{act} / k_{deact}$. The PDI can be expressed as

$$\frac{M_W}{M_n} = 1 + \left(\frac{k_p[I]_0}{k_{deact}[XCu^{II}]}\right)\left(\frac{2}{P} - 1\right) \qquad \text{Eq. 2}$$

In Eq. 1, R_p is first order with respect to the solution concentrations of monomer [M] and the Cu^I catalyst. The initial build up of the Cu^{II} species eventually leads to control over the polymerization as the equilibrium between Cu^I and Cu^{II} is established. K_{eq} depends on the monomer structure and can be adjusted by the choice of the metal and ligands in the catalysts. A high value for K_{eq} gives a faster rate of polymerization, but if the value of K_{eq} is too high, ATRP simply becomes a conventional redox-initiated radical polymerization ($k_{deact} \sim 0$) with substantial termination. If K_{eq} is too small, the polymerization is too slow to be useful. Eq. 2 indicates that the PDI (M_w/M_n) decreases with conversion, p. For a given monomer, a decrease in the k_p/k_{deact} ratio through fast deactivation of the catalyst will result in lower PDI. In addition, a higher concentration of deactivator (Cu^{II}) will help control the polymerization (narrow molecular weight distribution), with the decrease of polymerization rate. Therefore, in some examples of Cu-catalyzed ATRP, small amounts of Cu^{II} halides are added to the system in the initial stage of polymerization to control the polymerization.

ATRP components

Monomers

ATRP has successfully been employed on styrenes, acrylates, methacrylates, acrylonitriles, (meth)acrylamide, and other monomers. Scheme 1.3 lists representative monomers successfully polymerized using ATRP. Monomer structure is one of the determining factors of k_p, since it defines the stability of the radicals formed after the addition of growing radicals. Each monomer also has its own equilibrium constant (K_{eq} = k_{act}/k_{deact}), which defines its polymerization rate in ATRP. Therefore, each monomer has unique optimum polymerization conditions. The monomers used in this study are PEGMA macromonomers, methacrylates which contain pendent ethylene oxide segments. The novelty of these macromonomers is partly due to the incorporation of the biologically relevant PEO segments, and that they also directly afford comb-shaped polymers with regular and densely attached branches. Furthermore, crosslinked polymers can be prepared by homopolymerization of divinyl monomers or copolymerization of mono and divinyl groups.[46, 47]

Scheme 1.3. Representative monomers used for ATRP

a) Styrenes

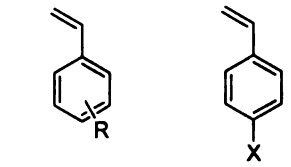

R= CH_3, ^tBu X=Br, Cl, F

b) Acrylates

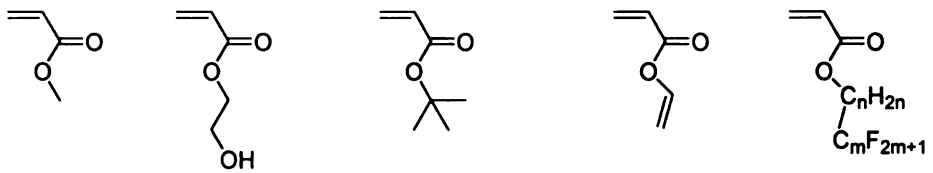

MA HEA tBA

c) Methacrylates

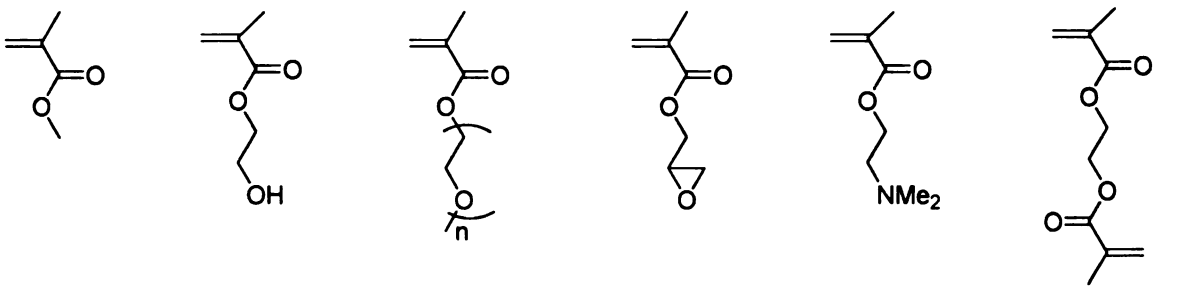

MMA HEMA PEGMA GMA DMAEMA EGDMA

Initiators

The diversity of ATRP initiators is larger than for other controlled polymerizations. Scheme 1.4. lists representative examples of initiators. A good ATRP initiator should be sufficiently reactive to ensure that all chain ends start to grow polymers at the same time, and the equilibrium in the initiation step should favor the dormant species in order to reduce the chance of side reactions. Substituent groups on initiators stabilize the radical in the order of CN > C(=O)R > C(=O)OR > Ph > Cl > Me, with α-haloesters the most common initiators used in surface-initiated ATRP. The general order in bond strength is R-Cl > R-Br > R-I, and while alkyl iodides are efficient initiatiors, bromo and chloro α-haloesters are the most often used since alkyl iodides require special precautions to avoid side reactions in ATRP.

Catalysts and ligands

(a) Cu based ATRP

A variety of transition metal complexes have been applied in ATRP, such as Mo,[48] Re,[49] Ru,[50, 51] Fe,[52-54] Rh,[55] Ni,[56 57] Pd,[58] and Cu [21, 59] metal complexes. The following discussion will emphasize copper-based ATRP since Cu mediated ATRP was used in this study. Cu complexes are versatile ATRP catalysts, with styrenes, (meth)acrylates, amides and acrylonitriles all successfully polymerized by ATRP.

Scheme 1.4. Representative examples of initiators used for ATRP

a) Halogenated alkanes and benzylic halides

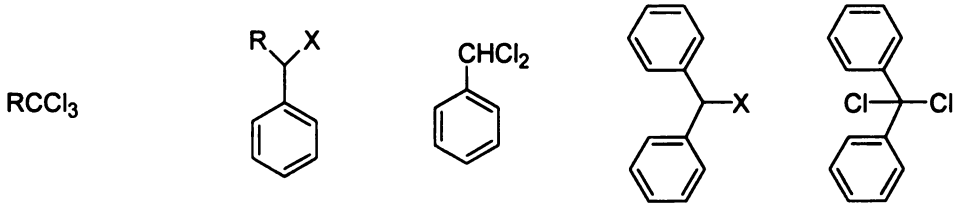

R = H, Cl, Br, Ph, CF_3, CO_2CH_3, C_nH_{2n+1}

R = H, CH_3, X = Br, Cl

X = Br, Cl

b) α- Haloesters and their derivatives

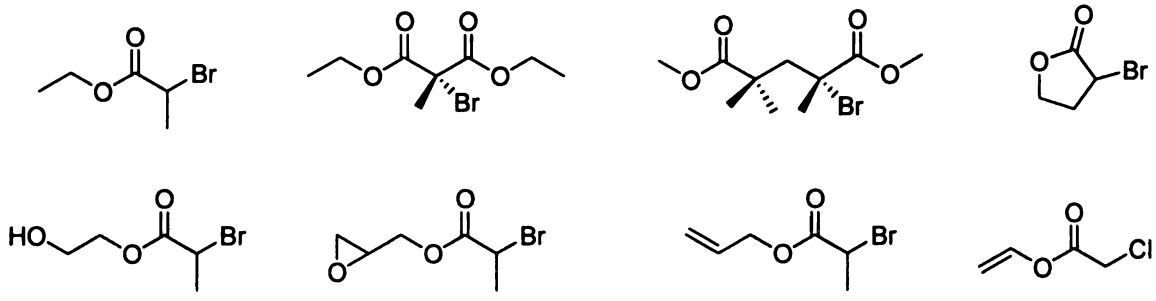

The choice of ligands used in ATRP catalysts can be used to adjust the equilibrium between the dormant and reactive radicals, and to solubilize and stabilize the metal catalyst in the reaction media at different temperatures. For copper-based ATRP, nitrogen ligands work best, with sulfur, oxygen or phosphorous ligands less effective, possibly due to the inappropriate electronic effects or unfavorable binding constants. The electronic and steric effects of ligands greatly affect the catalyst reactivity. Significant steric hindrance at the metal center or the use of ligands with strong electron-withdrawing

groups decreases catalyst reactivity. Scheme 1.5 shows examples of ligands used for copper-based ATRP. Bipyridine (bpy) has been the ligand of choice for copper-mediated ATRP of styrene and (meth)acrylic monomers. Cu/bpy complexes perform well in aqueous media, but their limited solubility in organic solvents reduces their control over the polymerization. To improve the solubility of the catalysts in organic solvents and maintain better control over the polymerization, bpy is often replaced by an alkyl-substituted analog 4,4'-di(*n*-nonyl)-2,2'-bipyridine (dnNbpy). The activity of nitrogen ligands usually increases with the number of coordinated sites ($N_4 > N_3 > N_2 >> N_1$), and decreases with the number C atoms that link nitrogen ($C_2 > C_3 > C_4$). Multidentate ligands, such as *tris*[2-(dimethylamino)ethyl]amine (Me_6TREN) and 1,1,4,7,10,10-hexamethyltriethylenetetramine (HMTETA) have been successfully used for the ATRP of styrene and methacrylates.

(b) Structures of Cu^I complexes

Cationic Cu^I complexes prefer a tetrahedral or square planar configuration with a tetradentate ligand or with two bidentate ligands. Cu^I complexes with bidentate ligands such as bpy are generally represented as $[Cu^I (bpy)_2]^+[Y]^-$. For Cu^I Br and Cu^I Cl salts, the counter ion $[Y]^-$ can also be the $[Cu^I Br_2]^-$ and $[Cu^I Cl_2]^-$ anions, respectively. In the solid state, the typical geometry of the $[Cu^I (bpy)_2]^+$ cation is a distorted tetrahedron, as shown in Figure 1.12.[60] The average Cu-N bond length ranges from 1.985 to 2.057 Å and is not greatly affected by the counter ion or substituents on the bpy ligand. The dihedral angle is in the range of 80-83° due to the restricted geometry of the bpy ligands.

Scheme 1.5. Examples of ligands often used for copper-mediated ATRP.

a) Bidentate ligands (N_2)

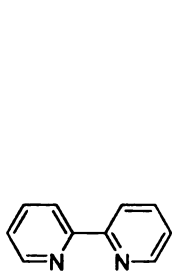

bpy

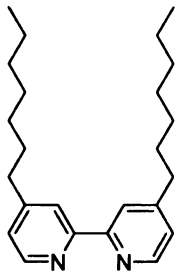

dNbpy

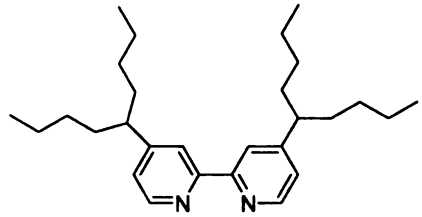

dnNbpy

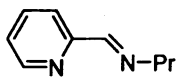

NPrPMI

b) Tridentate ligands (N_3)

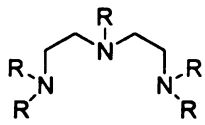

R=H, DETA

R=CH_3, PMDETA

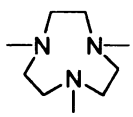

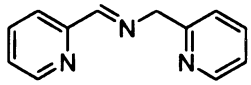

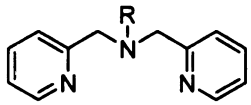

R=H, BPMA

R=$(CH_2)_7CH_3$ BPMOA

c) Tetradentate Ligands (N_4)

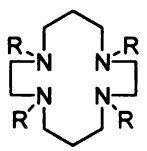

R=H, Cyclam

R=CH_3, Me_4 Cyclam

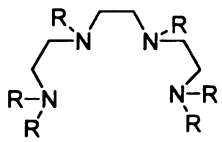

R=H, TETA

R=CH_3, HMTETA

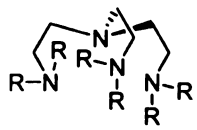

R=H, TREN

R=CH_3,Me_6TREN

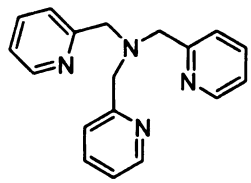

TPMA

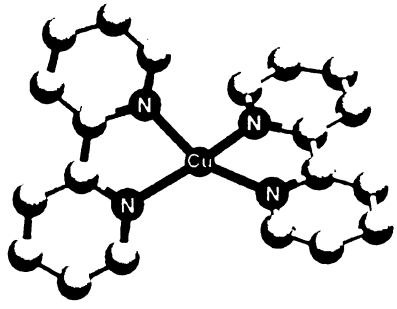

Figure 1.12. Structure of the $[Cu^{I}(bpy)_2]^{+}$ cation in $[Cu^{I}(bpy)_2]^{+}[ClO_4]^{-}$.

Bridging is observed in $Cu^{I}X$ (X = halide) (Figure 1.13). In $[Cu^{I}(bpy)Br_2]$, each Cu^{I} center has a distorted tetrahedral geometry and is coordinated to the two nitrogen atoms of a bpy ligand and two bridging bromides.

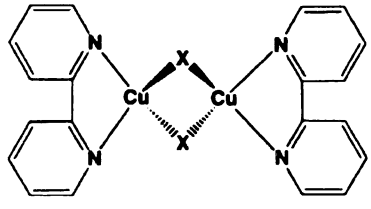

Figure 1.13. Structure of the $[Cu^{I}(bpy)X_2]$ (X=Br, Cl) dimer.

The structures of Cu^{I} /bpy complexes in solution also have been studied. In non-polar media, $Cu^{I}X$/bpy complexes were proposed to exist predominantly as the bridged complexes shown in Figure 1.13. However, in polar media, the predominant complexes are $[Cu^{I}(bpy)_2]^{+}[Y]^{-}$.

Cu/HMTETA complexes are very reactive catalysts and have been used in my research. The X-ray structure of $[Cu^{I}(HMTETA)_2]^{+}[Cu^{I}Cl_2]^{-}$ complex (Figure 1.14) indicates Cu^{I} in a distorted tetrahedral geometry.

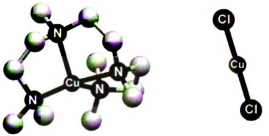

Figure 1.14. Molecular structure of $[Cu^{I}(HMTETA)]^{+}[Cu^{I}Cl_2]^{-}$.

(c) Structures of Cu^{II} complexes

It is generally accepted that the most common $Cu^{II}X_2$/bpy complexes are $[Cu^{II}(bpy)_2X]^{+}[X]^{-}$. As shown in Figure 1.15, $[Cu^{II}(bpy)_2X]^{+}$ adopts a trigonal bipyramidal geometry.

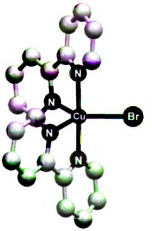

Figure 1.15. Structure of the $[Cu^{II}(bpy)_2Br]^{+}$ cation in $[Cu^{II}(bpy)_2Br]^{+}[Br]^{-}$.

$Cu(II)X_2$ complexes with tetradentate ligands such as HMTETA ($[Cu^{II}(HMTETA)X]^+[X]^-$) involve penta-coordination. As shown in Figure 1.16, the Cu center coordinates with four nitrogen atoms of the ligand and the donor halogen atom, forming a square pyramidal geometry.

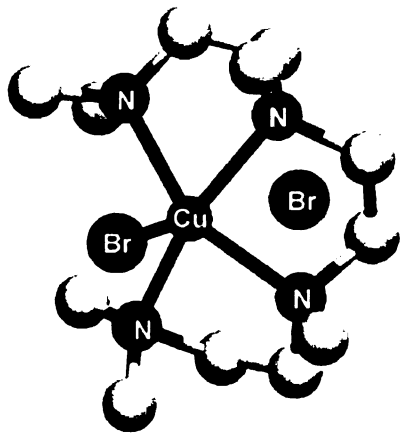

Figure 1.16. Molecular structure of $[Cu^{II}(HMTETA)Br]^+[Br]^-$.

Water as a polymerization solvent

A variety of solvents have been used for ATRP, including toluene, anisole, diphenyl ether, ethyl acetate, acetone, DMF, alcohols, and water.[20] Generally, the use of polar solvents improves the solubility of Cu^{II} complexes and favors homogeneous, well-controlled ATRP. Water has been increasingly employed for ATRP of polar, water soluble monomers having hydroxyl, oxyethylene, amino, ammonium, and carboxylate functional groups. Water also can greatly accelerate the polymerization rate. The first aqueous copper-mediated ATRP was reported by Matyjaszewski *et al.*,[61] the polymerization of 2-hydroxyethyl acrylate (HEA) in aqueous media (50:50 v:v) using a

CuBr/bpy catalyst at 90 °C. A 12 hour polymerization resulted in 87% conversion of monomer to polymer. Later, Armes *et al.*[62, 63] reported the remarkably fast ATRP of PEGMAs in water, 90% conversion in 30 min at 20 °C, while retaining control over the polymerization (PDI < 1.3). The fast polymerization rate was attributed to the formation of mononuclear Cu^{I} species in water. Huang *et al.* described the rapid growth of poly(HEMA) brushes in water using a catalyst prepared from 30 mol% CuCl, $CuBr_2$, and bpy.[64]

Water used as a co-solvent accelerates polymerizations, but there are no reports of the catalyst structure in water. However, it has been proposed that $[Cu^{I}(bpy)_2]^{+}[X]^{-}$ is the predominant complex in polar media, and is believed to be the reactive catalyst. There is also the possibility of solvent and monomer coordination to the catalyst. Haddleton[65] studied the effect of water on the polymerization of PEGMA(8-9) using a CuBr/*N*-(*n*-propyl)-2-pyridylmethanimine (NPrPMI) complex. They proposed the competitive coordination of water and ligand to the copper center, which results in an increase in polymerization rate. Later, Jonsson[66] studied the ATRP of PEGMA(7-8) in aqueous media, and calculated the propagating radical concentration from the redox properties of the alkyl halide and Cu complex. The calculated radical concentration in water is 3 orders of magnitude higher than in acetonitrile, which contributes to the fast ATRP kinetics in water.

ATRP of PEGMA

There are two general strategies for incorporating PEO segments in polymer structures via ATRP. In the *macroinitiator* approach[67-72] shown in Scheme 1.6., an ω-hydroxy group of PEO is converted into an ATRP initiator by coupling with an α-bromoacyl bromide or α-bromocarboxylic acid. This scheme provides block copolymers. The *macromonomer* approach is the direct polymerization of a PEG-containing monomer such as a PEG methacrylate. This scheme provides densely grafted comb polymers with PEG teeth. The macromonomer approach is a convenient way to form macromolecular structures with PEO segments. Haddleton *et al.*[73] investigated ATRP of PEGMA (M_n = 480 g/mol) in toluene mediated by Cu^IBr/NPrPMI. Using an on-line ^{1}H-NMR analysis, they observed a fast polymerization rate, 90% conversion in 1 hour at 90 °C. These reaction conditions are harsh and incompatible with polymerizations from gold since the Au-S bond is unstable above 60 °C. Armes *et al.* [62, 63] studied ATRP of PEGMAs with ~8 and 45 repeating units of ethylene oxide in water, and also found that polymerization rate was remarkably fast (90% conversion in 20 min at 20 °C), but still controlled (PDI < 1.3). Apparently, water greatly accelerated the polymerization rate, as discussed above. The structure of PEGMA plays an important role in accelerating polymerization since the sterically congested PEGMA inhibits radical-radical coupling, which reduces the termination rate (k_t). Decreases in k_t with increased monomer size also has been observed for alkyl-substituted methacrylate esters. For example, k_t for undecenyl methacrylate is 0.6×10^{-6} L/(mol • s), 1/40 of the rate for methyl methacrylate (25.5×10^{-6} L/mol • s).

Scheme 1.6. Synthetic approaches used to incorporate PEO segments in polymers.

(a) Macroinitiator approach

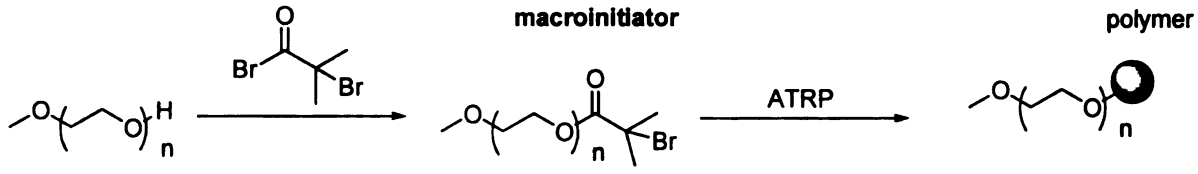

(b) Macromonomer approach

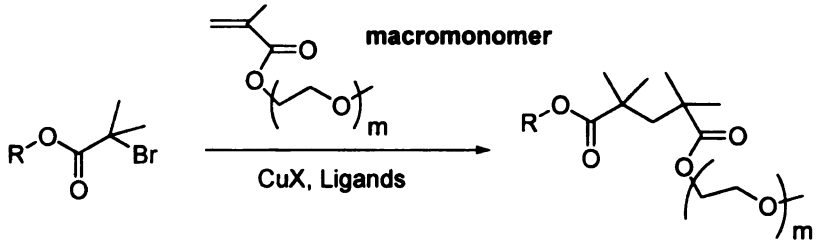

Ito *et al.*[74] reported aqueous ATRP of two styrene-functionalized PEG macromonomers (M_n = 2300 g/mol). They reported that k_p/k_t was ~0.25 in water, and proposed inter-micellar polymerization to explain the high molecular weight they obtained. However, no evidence for micellar polymerization was found in Arme's system. Later, Jonsson *et al.*[66] estimated k_p to be 3.6×10^3 M^{-1} s^{-1} for PEGMA (M_n = 480 g/mol) in water by correlating the apparent polymerization rate with the redox potential ($E_{1/2}$) of copper complex. The high overall polymerization rate was ascribed to complexation of ethylene glycol groups to copper, displacing some of the diamine ligands to form a very reactive metal catalyst.

The above examples of PEGMA polymerization provided low molecular weights, with degree of polymerizations (DPs) ~10-33. A recent paper by Matyjaszewski *et al.*[75] described aqueous AGET (activator generated by electron transfer) ATRP of PEGMA homopolymers and random copolymers with DPs >240 and PDIs <1.3.

Given the results of PEGMA polymerization in solution, we expect surface-initiated ATRP of these monomers to provide thick polymer films on surfaces. The surface-initiated ATRP of PEGMA is elaborated in Chapters II and III.

Polymer brushes formed by surface-initiated ATRP

An advantage of the ATRP system is the facile process by which substrates are converted into initiators. Functionalization of the target substrate uses commercially available α-haloesters or benzyl halides and their derivatives, rather than the multi-step syntheses required for alkoxyamines and xanthates used in other controlled polymerizations. Not surprisingly, ATRP is the most commonly used controlled polymerization technique, and has been applied to the growth of well-defined polymer brushes on gold, silicon wafers, inorganic particles/colloids, organic latexes, and a variety of other substrates.

Methods for the controlled growth of polymers from surfaces.

As described earlier, the preparation of polymer brushes requires attachment of an initiator on the surface followed by ATRP of vinyl monomers from the substrate. Figure 1.19 depicts the general scheme for polymer brush formation on flat surfaces.

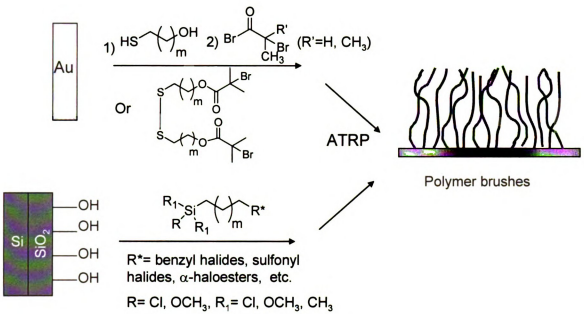

Figure 1.17. General synthetic route to polymer brushes on gold and silica substrates.

The main challenge in surface-initiated ATRP from flat surfaces is the inherent low concentration of initiators in the system, and therefore, a low concentration of the Cu^{II} radical deactivator. At low Cu^{II} concentrations, ATRP may resemble a redox process, an uncontrolled polymerization dominated by termination. The addition of deactivator in the form of Cu^{II} can compensate for the low Cu^{II} concentration, or sacrificial initiator can be added. In the case of added sacrificial initiator, termination of radicals in solution will generate a sufficient concentration of deactivator to afford control over the polymerization. The addition of "free" initiator to the system is not only beneficial for controlled synthesis of polymer brushes, but also provides a way to characterize polymer brushes. Analysis of polymers formed in solution can be used to estimate the molecular weight of tethered polymer chains, since several experiments have shown that the polymer chains cleaved from surfaces have molar masses and PDIs

similar to the polymers formed in solution. The DP of tethered polymer chains can be estimated from the concentrations of consumed monomers and sacrificial initiator, assuming all initiators were used.

$$DP = \Delta [M]/[initiator]$$

However, a significant drawback of adding sacrificial initiator is the formation of polymer in solution, which can be very difficult to remove from surfaces, especially during the synthesis of crosslinked polymer brushes. The alternative, adding a Cu^{II} deactivator, is particularly useful in controlling polymer brush growth. Using 30 mol% $CuBr_2$ as a deactivator in HEMA polymerizations, Huang *et al.* obtained 400 nm thick films compared to 200 nm films without $CuBr_2$.[64] The results are sensitive to the $CuBr_2$ concentration; the limiting film thickness using 5% $CuBr_2$ (relative to the Cu^{I} concentration) was slightly >200 nm. A related study on the polymerization kinetics of methyl acrylate (MA) defined 0.1×10^{-3} M as the Cu^{I} concentration that yields the thickest films when the Cu^{II} concentration was fixed at 30 mol%.[76] The Cu^{I} concentration was varied from 40 mM to 2.5×10^{-4} M in this study. Diluting the catalyst concentration also helps control the growth of polymer brushes.

Brush architectures generated by surface-initiated ATRP.

The versatility of surface-initiated polymerizations makes it possible to form a variety of brush architectures on flat surfaces, including block copolymer, binary polymer brushes, [77, 78] comb-like polymer brushes, hyperbranched polymers,[79, 80] and crosslinked polymer brushes,[81] as shown in Figure 1.18. Huang *et al.* described the facile synthesis of crosslinked polymer brushes on gold by surface-initiated ATRP.[81] Chapter III will

describe studies of comb-like polymer brushes with PEO segments grown on different substrates, and crosslinked polymer brushes will be described in Chapter IV.

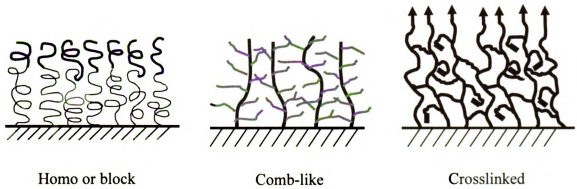

Figure 1.18. Schematic illustration of linear, comb-like and crosslinked polymer brushes.

Polymers grown by ATRP retain a halogen at the terminus of the growing polymer chain. As described earlier, these sites can be reactivated to initiate the formation of block copolymers. As shown by Zhao *et al.*[82] these sites also can be permanently deactivated. Zhao designed novel binary polymer brushes by combining ATRP and NMP. As shown in Figure 1.19, a Y-shaped SAM was formed on the surface that incorporated both ATRP and NMRP initiators. ATRP of MMA was followed by removal of the terminal halogen using Bu_3SnH. Styrene was then polymerized by NMP to form binary polymer brushes that show lateral phase separation.

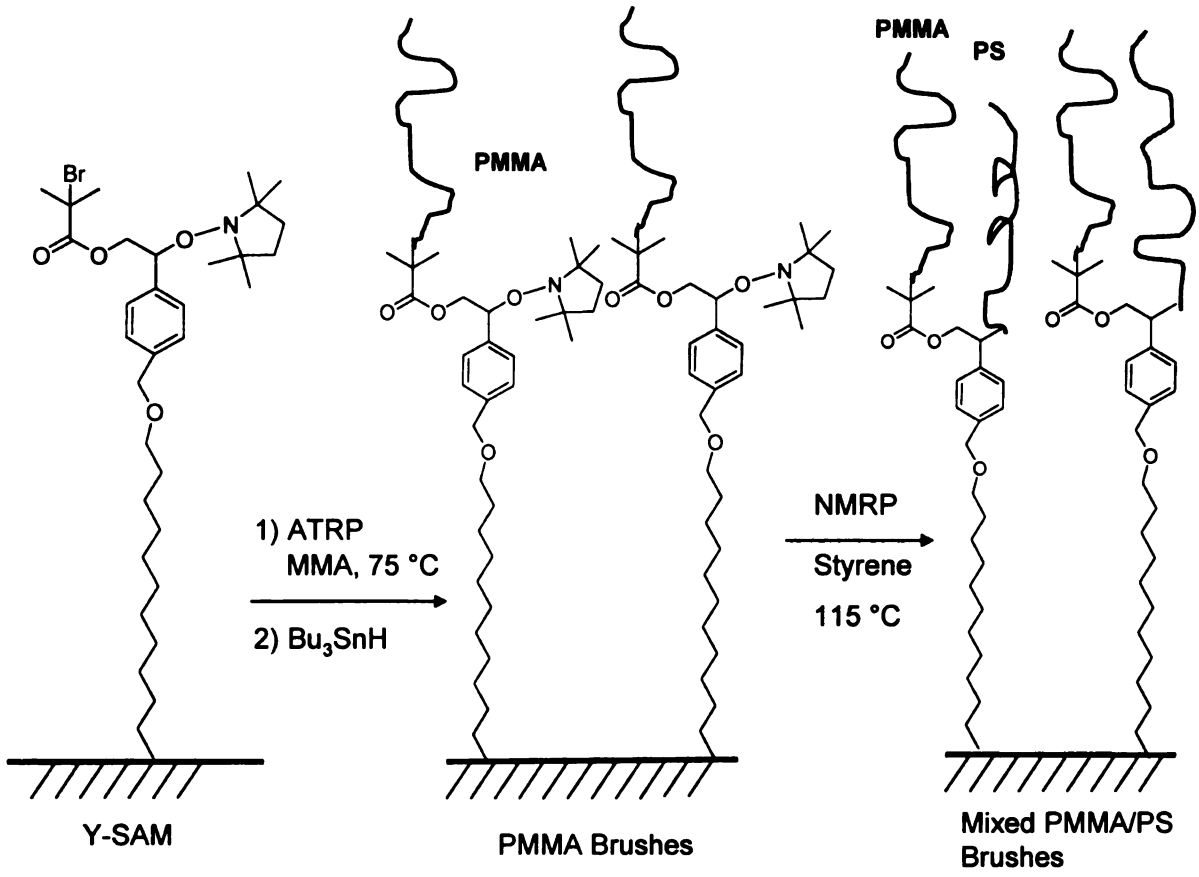

Figure 1.19. Synthesis of mixed PMMA/PS brushes from an asymmetric di-functional initiator-terminated SAM (Y-SAM) by combining ATRP and NMRP techniques. Reprinted with permission from *J. Am. Chem. Soc.* **2004**, *126*, 6124-6134. Copyright © 2004 American Chemical Society.

Controlled ATRP from surfaces of particles.

Surface-initiated ATRP is not confined to the formation of polymer brushes on planar substrates. Polymer/inorganic hybrid nanoparticles have also been prepared by surface-initiated ATRP of various monomers from colloidal initiators,[6, 80, 83-88] aiming to improve their stability in different solvents. A variety of inorganic substrates can be modified by polymer brushes; the following discussion will emphasize polymer brushes

grown on the surfaces of silica nanoparticles. Using mild conditions (water, 20 °C), Armes *et al.*[89] grafted poly(PEGMA) and poly((2-*N*-morpholino)ethyl methacrylate)) (PMEMA) brushes on the surface of 300 nm silica particles prepared by the Stober process. The PMEMA grafted silica particles showed lower critical solution temperature (LCST) behavior, and began to aggregate at 34 °C. The aggregates completely re-dispersed on cooling below the LCST.

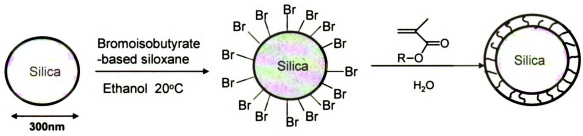

Figure 1.20. Poly(PEGMA) and PMEMA brushes grown from silica nanoparticles.

Zhao *et al.*[90] reported the first synthesis of comb-coil polymer brushes on the surface of silica nanoparticles. A poly(HEMA) brush was grown from the nanoparticle by surface-initiated ATRP. Then, concurrent polymerization of *tert*-butyl acrylate (tBA) and lactide were initiated from the terminal halogen group by AGET ATRP, and from the OH groups of the poly(HEMA) side chains by ROP, respectively.

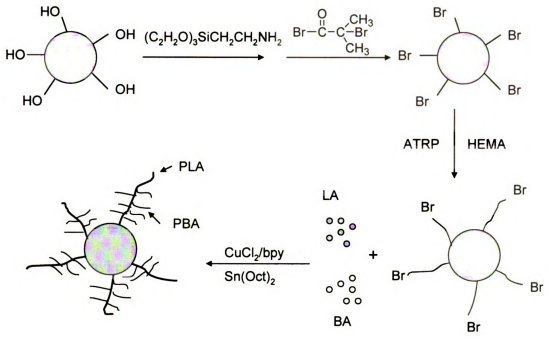

Figure 1.21. Preparation of comb-coil polymer brushes on the surface of silica nanoparticles.

Physicochemical properties of polymer brushes

Physical states of polymer brushes

The physical nature of surfaces ("hard" or "soft") largely depends on the physical states of polymer brushes (crystalline or amorphous). To date, most polymer brushes have been amorphous, including glassy polymers such as PS or rubbery polymers such as polydimethoxysilane (PDMS).

Liquid crystalline polymer (LCP) brushes have attracted substantial interest due to the application of LC materials for displays and as semi-conducting materials. Peng *et al.*[91] synthesized and studied side chain LCP brushes comprised of phenylbenzoates

tethered to a polymethacrylate with a spacer. These films, up to 200 nm thick and prepared by surface-initiated free-radical polymerization, were used as alignment layers for LC systems. Alignment layers orient LCs at surfaces and provide the large area domains needed for displays. As the brushes were heated or exposed to solvent, the LC phase underwent a reversible nematic to isotropic LC phase transition. Recently, Huck *et al.*[92] reported the synthesis of side chain LCP brushes formed by surface-initiated ATRP of active acrylate mesogens on silica and glass substrates (Figure 1.22). Glass sides with polymer brushes were oriented face to face and separated by a spacer. A nematic LC, 4'-pentyl-4-biphenyl carbonitrile, was injected into the gap between the slides and spread as a result of capillary forces. Homeotropic alignment was observed, which was ascribed to the interaction of LC side chain with the LC phase. Alignment was also observed on nanopatterned substrates, particularly in regions where polymer brushes were present on both the top and bottom substrates. This suggests potential applications for brushes in displays and optoelectronics.

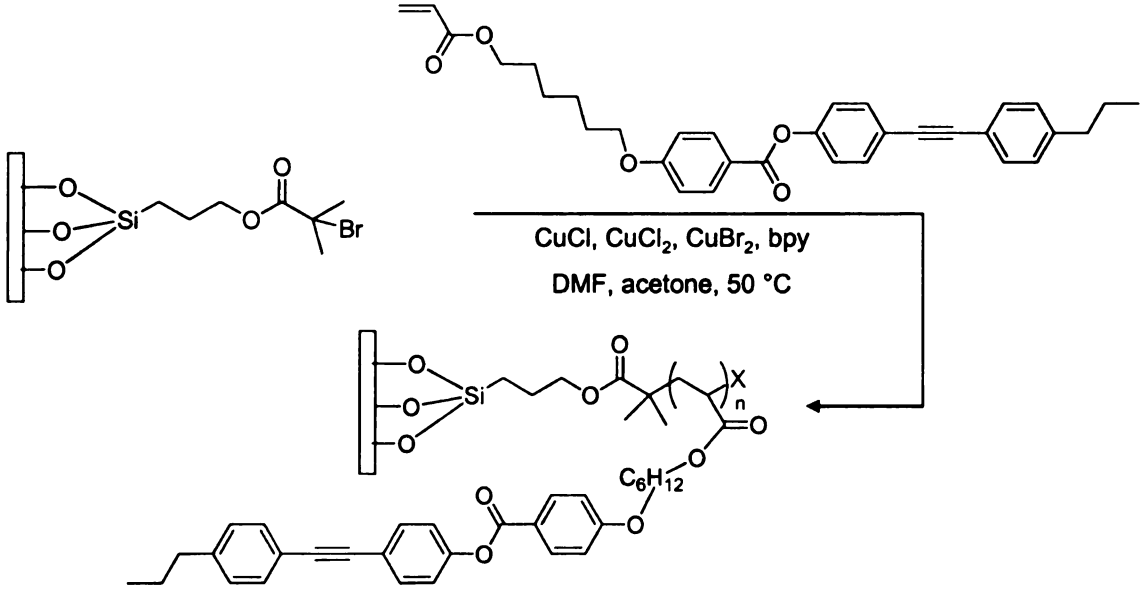

Figure 1.22. Synthesis of side chain LCP brushes by surface-initiated ATRP.

Although much progress has been made on amorphous polymer films and LCP brushes, there are few examples of studies on the crystalline state of polymer brushes. Studies of polymer brush crystallization should help explain polymer crystallization in constrained geometries. Chapter II will elaborate on the crystallization behavior of polymer brushes.

Stimuli-responsive polymer brushes

Stimuli-responsive polymer brushes are attractive for applications as "smart" or responsive surfaces. Such brushes would alter their conformations upon changes in temperature, solvents, pH, photo-illumination, or another external trigger, resulting in changes in the surface physical properties.

Solvent induced polymer brush rearrangement.

For simple A-B block copolymers, phase separation of the A and B blocks generally occurs when the heat of mixing is positive. Phase separation of A-B block copolymers also occurs on surfaces, but being tethered to the surface, the polymer chains are constrained to separate in nanometer-sized domains. Immersing block copolymer brushes such as PMMA-*b*-PS in different solvents results in solvent-induced structuring of the surface. Brittain *et al.*[93,94] studied the rearrangement of PMMA-PS block polymer brushes in CH_2Cl_2 (a good solvent for both blocks) and cyclohexane (a good solvent for PS but not for PMMA). When the polymer brushes are in CH_2Cl_2, both blocks swell and stretch away from the substrate, yielding a smooth surface. When the polymer brushes

are in a mixture of CH_2Cl_2 and cyclohexane, the PMMA blocks collapse to form aggregates and avoid interaction with cyclohexane.

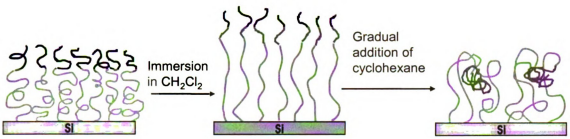

Figure 1.23. Speculative model for nanopattern formation in di-block copolymers.

A-B-A triblock copolymers showed similar phenomena. For PMMA-*b*-PS-*b*-PMMA, the film showed extended conformations when exposed to the good solvent (CH_2Cl_2), and a folded brush conformation when exposed to cyclohexane, which is a good solvent only for the middle block.[95]

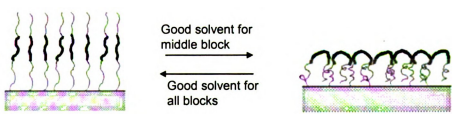

Figure 1.24. Reversible response of triblock copolymer brushes to different solvents.

Polymer brushes can show different solvent induced changes in their surface morphologies provided they have sufficient conformational freedom. Pyun *et al.*[96] synthesized an A-B-C triblock copolymer (PDMS-*b*-PS-*b*-Poly((3-(dimethoxy

methylsilyl)propyl acrylate (DMSA) using anionic ring opening polymerization and ATRP. The polymer was "*grafted to*" the silica surface resulting in polymer brushes with low grafting densities. The polymer brushes rearranged to form glassy or rubbery surfaces when immersed in different solvents (toluene and hexane) (Figure 1.25).

Various polymer brush architectures were constructed on surfaces to study their properties. For example, Li *et al.*[97] grew mixed P*t*BA/PS brushes on silica particles by the sequential ATRP of tBA and NMP of styrene from Y-shaped-initiators anchored on silica particles. The block copolymer chains tethered to these particles reorganized in response to changes in solvent, forming stable suspensions in $CHCl_3$ and MeOH, which are good solvents for PS and poly (acrylic acid) (PAA, hydrolysis product of P*t*BA), respectively.

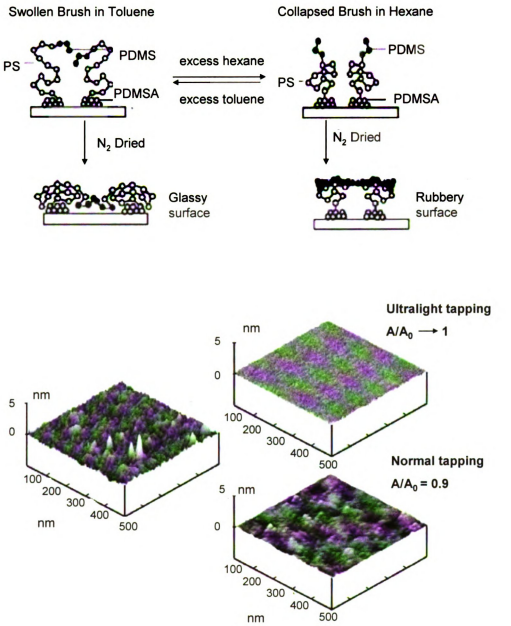

Figure 1.25. Tapping mode AFM height images of PDMS-*b*-PS-*b*-PDMSA brushes after the following treatments: (left) after immersion in toluene and drying with nitrogen, (right) after immersion in toluene, gradual addition of hexane and drying with nitrogen. Reprinted with permission from *Macromol. Chem. Phys.* **2004**, *205*, 411. Copyright © 2004 Wiley Intersciences.

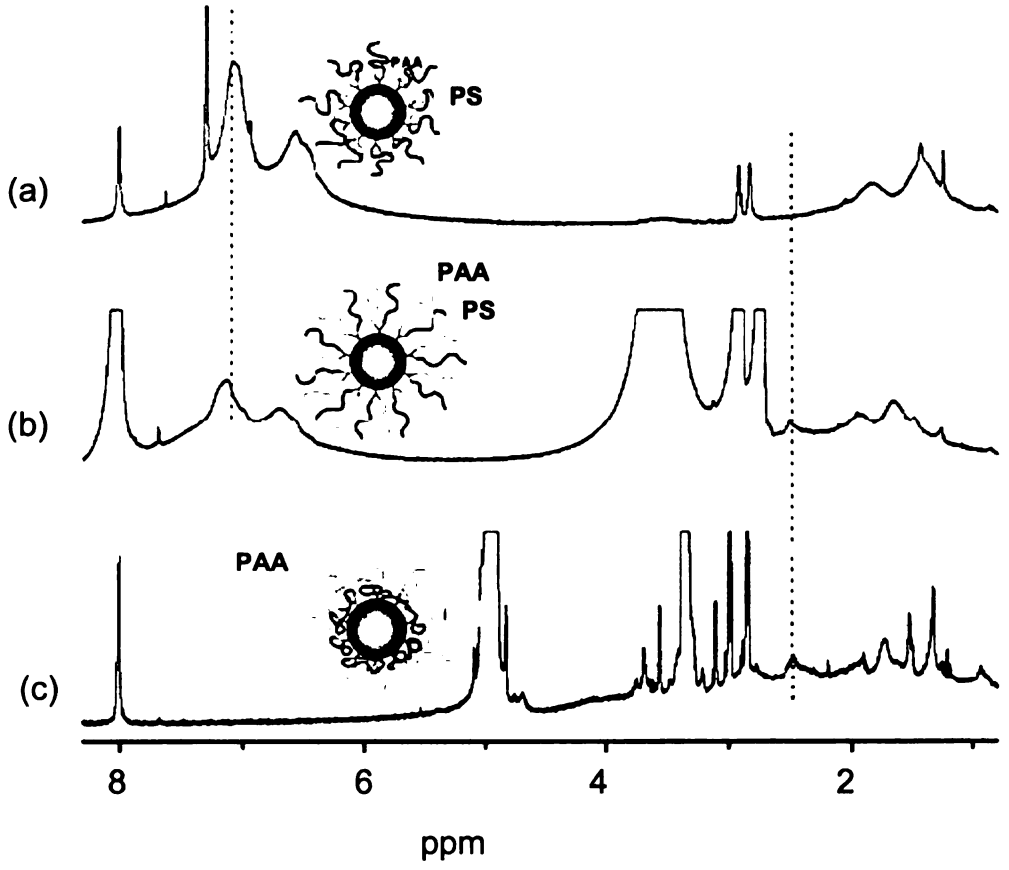

Figure 1.26. ^{1}H NMR spectra of PAA/PS particles dispersed in (a) $CDCl_3$, (b) DMF-d_7, and (c) CD_3OD. A drop of DMF-d_7 was added into the particles prior to $CDCl_3$ and CD_3OD to increase the concentration of the dispersed nanoparticles. Reprinted with permission from *J. Am. Chem. Soc.* **2005**, *127*, 6248-6256. Copyright © 2005 American Chemical Society.

Temperature-responsive polymer brushes

Poly(*N*-isopropylacrylamide) (PNIPAAM) films are widely studied as temperature responsive films since its LCST is ~32-33 °C, an easily accessible and biologically relevant temperature. Jiang *et al.* prepared PNIPAAM films on a well-controlled rough surface by surface-initiated ATRP.[98] The films switch between super-hydrophilicity (contact angle ~0 °) and super-hydrophobicity (contact angle ~150 °) within a 10° temperature range. At 25 °C (below the LCST of PNIPAAM), the polymer

adopts an extended brush architecture and the surface is hydrophilic due to H-bonding between the polymer chains and water. At 40 °C (above the LCST), the polymer structure is collapsed and the surface is hydrophobic due to H-bonding exclusively between polymer chains.

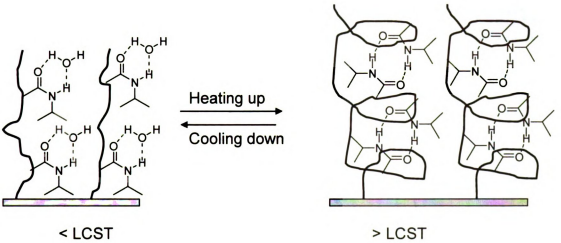

Figure 1.27. Diagram showing reversible formation of intermolecular hydrogen bonding between PNIPAAM chains and water molecules (left) and intramolecular hydrogen bonding between the C=O and N-H groups in PNIPAAM chains (right) below and above the LCST. This mechanism is proposed to explain the thermally responsive wettability of a PNIPAAM thin film.

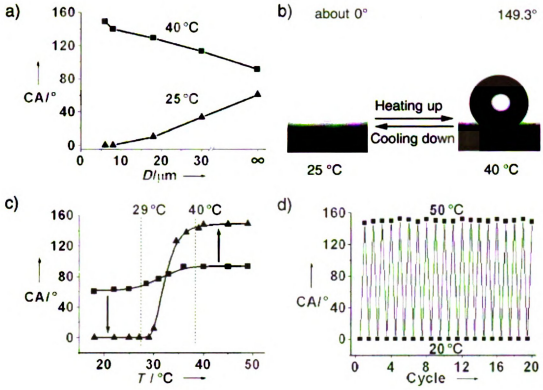

Figure 1.28. Surface-roughness-enhanced wettability of a PNIPAAM-modified surface. a) The relationships between groove spacing (D) of rough surfaces and the water contact angle at 25 °C (▲), and at 40 °C (■). b) Water drop profile for thermally responsive switching between super-hydrophilicity and super-hydrophobicity of a PNIPAAM-modified rough surface with a groove spacing of about 6 µm, at 25 °C and 40 °C. The water contact angles are ~0° and 149.3°, respectively. c) The temperature (T) dependence of water contact angles for PNIPAAM thin films on a rough substrate with groove spacing of about 6 µm (▲) and on flat substrate (■). d) Water contact angles at two different temperatures for a PNIPAAM-modified rough substrate with a groove spacing of 6 µm. Half cycles: 20 °C; and integral cycles: 50 °C. Reprinted with permission from *Angew. Chem., Int. Ed.* **2004**, *43*, 357-360. Copyright © 2004 Wiley Intersciences.

Applications of polymer brushes

Polymer brushes can be applied in many different areas. For example, LCP brushes, discussed previously, can be used as semiconducting polymers for LC displays. With the development of nanotechniques, switchable surfaces have been used for bioanalysis, microfluidic devices, and protein separations. Some representative examples of polymer brush applications are described below.

Nanotechnology—Patterning of polymer brushes

One of the most important applications of polymer brushes is that they are well-suited for the fabrication of nano- or micro-patterned arrays, which could be useful in cell growth control, biomimetic microfabrication, drug delivery and microelectronics. Polymer brushes can be patterned by traditional photolithography or chemical amplification of patterned SAMs. Photolithography was first explored by Ruhe *et al.*, [99] who exposed polymers to UV light through a mask. A good example of the complex patterning that can be carried out on polymer brushes was described by Hawker and co-workers.[100] A P*t*BA brush was formed on a silica substrate, followed by spin-casting on the surface a polystyrene film containing bis(*tert*-butylphenyl)iodonium triflate. After exposing the surface to UV irradiation through a mask, the P*t*BA brushes were converted to PAA brushes, resulting in a surface with distinct hydrophobic and hydrophilic areas. SAM patterning was obtained by micro-contact printing (μCP), which was first introduced by Whitesides *et al.*,[101] and the pattern initiator monolayer was amplified from the by surface initiated polymerization. Caster and co-workers [102] used scanning probe lithography and surface-initiated ATRP to nanopattern PNIPAAM brushes.

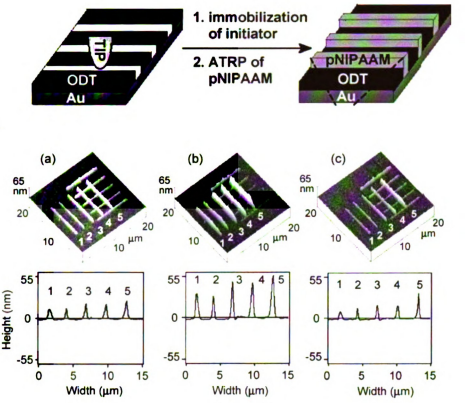

Figure 1.29. (top) Preparation of surface-confined PNIPAAM polymer brush nanopatterns by combining "nanoshaving" and surface-initiated ATRP using a surface-tethered thiol initiator. (Bottom) Contact mode AFM height images (20 μm × 20 μm) and corresponding typical height profiles of a PNIPAAM brush line nanopattern imaged at room temperature in (a) air, (b) MQ-grade water, and (c) a mixture of MeOH/water (1:1, v:v). Reprinted with permission from *Nano Lett.* **2004**, *4*, 373-376. Copyright © 2004 American Chemical Society.

Biological application in protein resistance and cell adhesion

PEO (or PEG) is very important in biological applications due to its ability to resist protein absorption and cell adhesion (non-specific adhesion resistance). PEO-containing surfaces used for current nanotechnology application are generated by self-assembly of OEG alkane thiols on gold surfaces. PEO-containing polymer brushes are attractive due to their synthetic robustness, and high surface grafting densities. As shown earlier (Figure 1.12), Andruzzi *et al.* compared the OEG tethered polystyrene brushes with OEG SAMs, and found that polymer brushes were superior in their ability to inhibit protein (less than 6%) and cell (less than 3%) adhesion when compared to surface assemblies with the same ethylene glycol length.

Biocompatible and non-biofouling PEO containing polymer brushes patterned onto gold or silica by various lithography techniques can be applied to "molecular recognition". The non-patterned regions are backfilled with a molecule that has a specific interaction with cell or other biomolecules. For example, Figure 1.31 shows a nanopatterned gold surface modified with poly(PEGMA) brushes, [103] and a cell-adhesive protein was absorbed on the surface after the features were backfilled with SAM **2**. Two different cells were patterned on the surface.

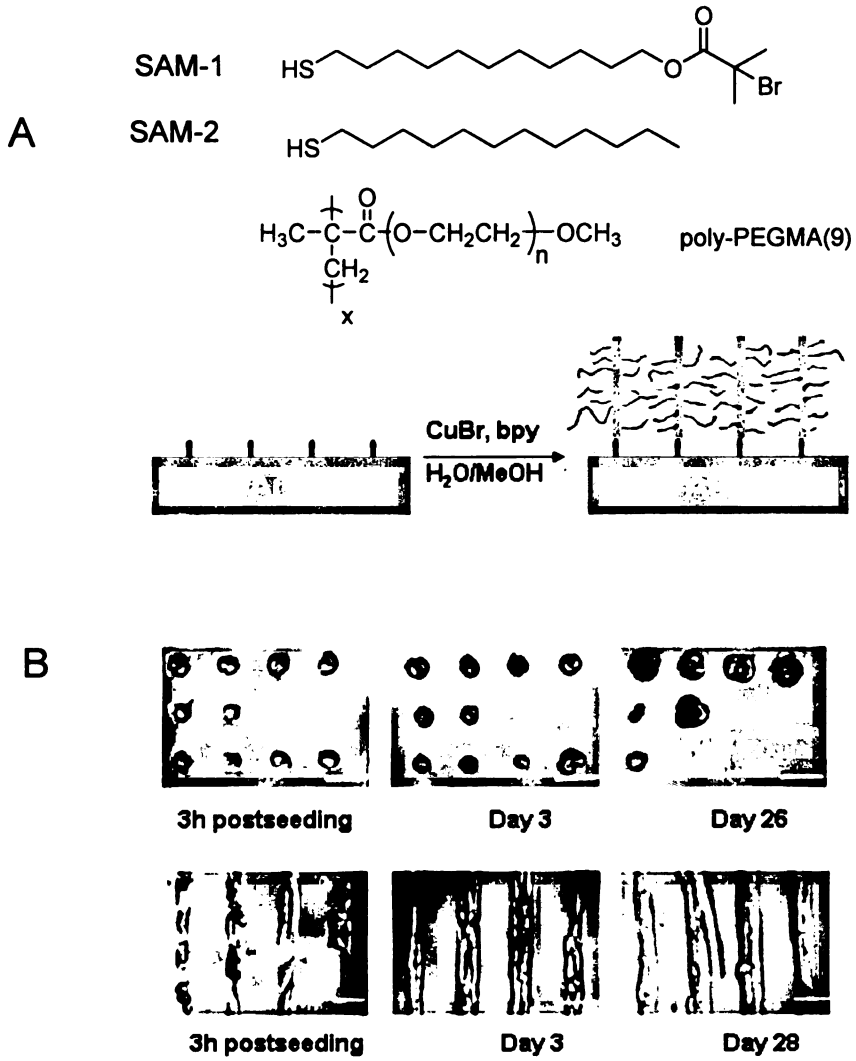

Figure 1.30. A) a PEGMA polymerized by ATRP from a micropatterned gold surface. (B) NIH 3T3 fibroblast cells cultured on patterns of adsorbed fibronectin (20 μm circles and 40 μm stripes). Reprinted with permission from *Biomacromolecules*, **2005**, *6*, 2427-2448. Copyright © 2005 American Chemical Society.

Polymer brushes grafted membranes.

Ito *et al.* reported pH sensitive,[104] photosensitive,[105] and oxidation/reduction sensitive[106] polymer brushes covalently tethered to porous membranes, which can be used to regulate liquids flowing through porous membranes.

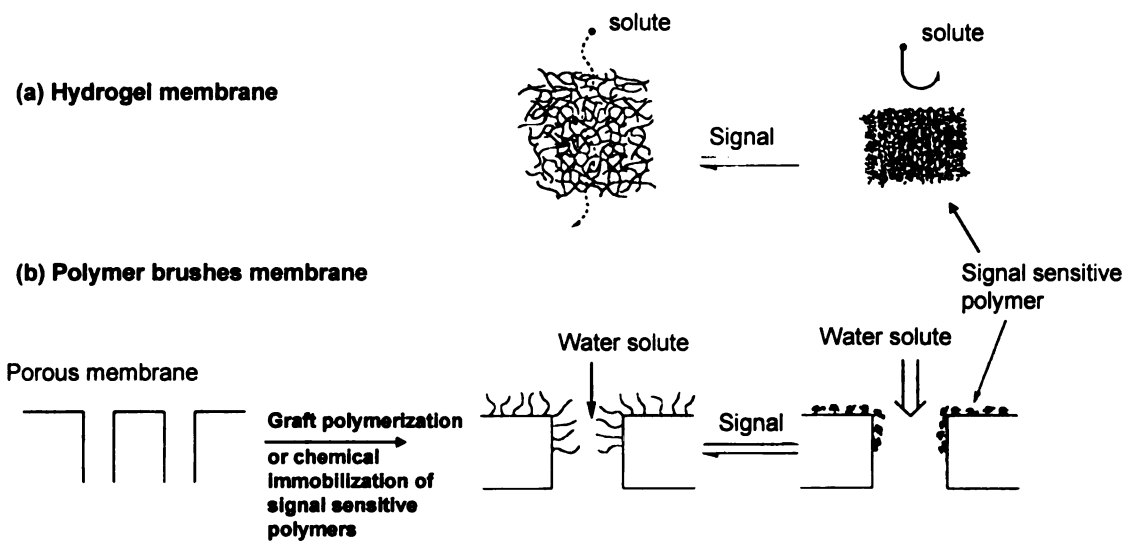

Figure 1.31. Preparation of polymer brushes grafted to porous membranes and an illustration of the mechanism for regulating water and solute permeation through a polymer brush grafted membrane and a hydrogel membrane.

Polymer brushes grafted on membranes afford selective gas transport. Balachandra *et al.*[107] grafted cross-linked poly(ethylene glycol dimethacrylate) (Poly(EGDMA)) and poly(HEMA) brushes on the surface of porous aluminum membrane supports. Gas permeation studies with poly(EGDMA) films showed a CO_2/CH_4 selectivity of 20, and a CO_2 permeability coefficient of 20 Barrer. The CO_2/CH_4 selectivity of poly(HEMA) films was only 0.9, however, fluorination of

poly(HEMA) increased the CO_2/CH_4 selectivity to 9. Described in Chapter V are the preparation of PEO-containing polymer brushes grafted from porous alumina membrane supports, and the permeability of gasses through the membranes.

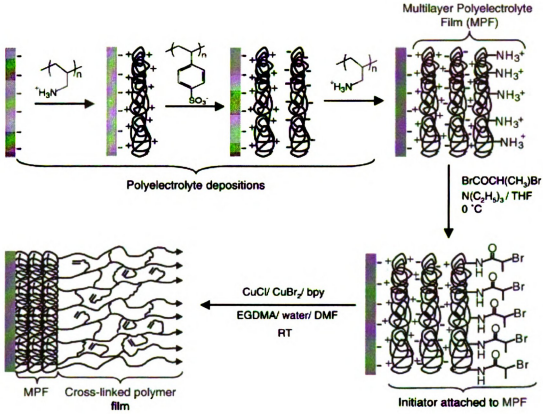

Figure 1.32. Schematic diagram showing polymerization of EGDMA from a polyelectrolyte surface modified with an initiator. Reprinted with permission from *J. Membr. Sci.* **2003**, *227*, 1-14.

References:

1. Zhao, B.; Brittain, W. J., *Prog. Polym. Sci.* **2000,** *25*, 677-710.

2. Milner, S. T., *Science* **1991,** *251*, 905-914.

3. Edmondson, S.; Osborne, V. L.; Huck, W. T. S., *Chem. Soc. Rev.* **2004,** *33*, 14-22.

4. Jennings, G. K.; Brantley, E. L., *Adv. Mater.* **2004,** *16*, 1983-1994.

5. Husseman, M.; Malmstrom, E. E.; McNamara, M.; Mate, M.; Mecerreyes, D.; Benoit, D. G.; Hedrick, J. L.; Mansky, P.; Huang, E.; Russell, T. P.; Hawker, C. J., *Macromolecules* **1999,** *32*, 1424-1431.

6. Huang, X.; Wirth, M. J., *Macromolecules* **1999,** *32*, 1694-1696.

7. Kim, J. B.; Bruening, M. L.; Baker, G. L., *J. Am. Chem. Soc.* **2000,** *122*, 7616-7617.

8. Jones, D. M.; Brown, A. A.; Huck, W. T. S., *Langmuir* **2002,** *18*, 1265-1269.

9. Pyun, J.; Kowalewski, T.; Matyjaszewski, K., *Macromol. Rapid Commun.* **2003,** *24*, 1043-1059.

10. Pyun, J.; Matyjaszewski, K., *Chem. Mater.* **2001,** *13*, 3436-3448.

11. Ionov, L.; Minko, S.; Stamm, M.; Gohy, J. F.; Jerome, R.; Scholl, A., *J. Am. Chem. Soc.* **2003,** *125*, 8302-8306.

12. Currie, E. P. K.; Norde, W.; Stuart, M. A. C., *Adv. Colloid. Interface Sci.* **2003,** *100*, 205-265.

13. Luzinov, I.; Minko, S.; Tsukruk, V. V., *Prog. Polym. Sci.* **2004,** *29*, 635-698.

14. Huck, W. T. S.; Yan, L.; Stroock, A.; Haag, R.; Whitesides, G. M., *Langmuir* **1999,** *15*, 6862-6867.

15. Zhou, F.; Jiang, L.; Liu, W. M.; Xue, Q. J., *Macromol. Rapid. Commun.* **2004,** *25*, 1979-1983.

16. Zhou, F.; Liu, W. M.; Hao, J. C.; Xu, T.; Chen, M.; Xue, Q. J., *Adv. Funct. Mater.* **2003,** *13*, 938-942.

17. Senaratne, W.; Andruzzi, L.; Ober, C. K., *Biomacromolecules* **2005,** *6*, 2427-2448.

18. Rutenberg, I. M.; Scherman, O. A.; Grubbs, R. H.; Jiang, W. R.; Garfunkel, E.; Bao, Z., *J. Am. Chem. Soc.* **2004,** *126*, 4062-4063.

19. Kamigaito, M.; Ando, T.; Sawamoto, M., **2001,** *101*, 3689-3745.

20. Matyjaszewski, K.; Xia, J. H., *Chem. Rev.* **2001,** *101*, 2921-2990.

21. Patten, T. E.; Matyjaszewski, K., *Adv. Mater.* **1998,** *10*, 901.

22. Advincula, R.; Zhou, Q. G.; Park, M.; Wang, S. G.; Mays, J.; Sakellariou, G.; Pispas, S.; Hadjichristidis, N., *Langmuir* **2002,** *18*, 8672-8684.

23. Advincula, R. C., *J. Dispersion Sci. Tech.* **2003,** *24*, 343-361.

24. Jordan, R.; Ulman, A.; Kang, J. F.; Rafailovich, M. H.; Sokolov, J., *J. Am. Chem. Soc.* **1999,** *121*, 1016-1022.

25. Zheng, L.; Xie, A. F.; Lean, J. T., *Macromolecules* **2004,** *37*, 9954-9962.

26. Quirk, R. P.; Mathers, R. T.; Cregger, T.; Foster, M. D., *Macromolecules* **2002,** *35*, 9964-9974.

27. Sakellariou, G.; Park, M.; Advincula, R.; Mays, J. W.; Hadjichristidis, N., *J. Polym. Sci. A: Polym. Chem.* **2006,** *44*, 769-782.

28. Jordan, R.; Ulman, A., *J. Am. Chem. Soc.* **1998,** *120*, 243-247.

29. Jordan, R.; West, N.; Ulman, A.; Chou, Y. M.; Nuyken, O., *Macromolecules* **2001,** *34*, 1606-1611.

30. Zhao, B.; Brittain, W. J., *J. Am. Chem. Soc.* **1999,** *121*, 3557-3558.

31. Prucker, O.; Ruhe, J., *Macromolecules* **1998,** *31*, 592-601.

32. Prucker, O.; Ruhe, J., *Macromolecules* **1998,** *31*, 602-613.

33. Kim, N. Y.; Jeon, N. L.; Choi, I. S.; Takami, S.; Harada, Y.; Finnie, K. R.; Girolami, G. S.; Nuzzo, R. G.; Whitesides, G. M.; Laibinis, P. E., *Macromolecules* **2000,** *33*, 2793-2795.

34. Moon, J. H.; Swager, T. M., *Macromolecules* **2002,** *35*, 6086-6089.

35. Juang, A.; Scherman, O. A.; Grubbs, R. H.; Lewis, N. S., *Langmuir* **2001,** *17*, 1321-1323.

36. Liu, X. G.; Guo, S. W.; Mirkin, C. A., *Angew. Chem., Int. Ed.* **2003,** *42*, 4785-4789.

37. Husemann, M.; Mecerreyes, D.; Hawker, C. J.; Hedrick, J. L.; Shah, R.; Abbott, N. L., *Angew. Chem., Int. Ed.* **1999,** *38*, 647-649.

38. Choi, I. S.; Langer, R., *Macromolecules* **2001,** *34*, 5361-5363.

39. Joubert, M.; Delaite, C.; Bourgeat-Lami, E.; Dumas, P., *Macromol. Rapid Commun.* **2005,** *26*, 602-607.

40. Zhao, B.; Brittain, W. J., *Macromolecules* **2000,** *33*, 342-348.

41. Kim, J. B.; Huang, W.; Wang, C.; Bruening, M. L.; Baker, G. L., *Bottle Brush Brushes: Ring-Opening Polymerization of Lactide from Poly(hydroxy methacrylate) Surfaces*. Wiley-VCH VerlagGmbH&Co. KGaA: Weinheim, 2004.

42. Baum, M.; Brittain, W. J., *Macromolecules* **2002,** *35*, 610-615.

43. Matyjaszewski, K., *Controlled Radical Polymerization.* Washington, DC, 1998.

44. Andruzzi, L.; Senaratne, W.; Hexemer, A.; Sheets, E. D.; Ilic, B.; Kramer, E. J.; Baird, B.; Ober, C. K., *Langmuir* **2005,** *21*, 2495-2504.

45. Matyjaszewski, K., *Macromol. Symp.* **2002,** *183*, 71-81.

46. Connal, L. A.; Gurr, P. A.; Qiao, G. G.; Solomon, D. H., *J. Mater. Chem.* **2005,** *15*, 1286-1292.

47. Wang, A. R.; Zhu, S. P., *Macromolecules* **2002,** *35*, 9926-9933.

48. Brandts, J. A. M.; van de Geijn, P.; van Faassen, E. E.; Boersma, J.; van Koten, G., *J. Organometallic Chem.* **1999,** *584*, 246-253.

49. Kotani, Y.; Kamigaito, M.; Sawamoto, M., *Macromolecules* **1999,** *32*, 2420-2424.

50. Kato, M.; Kamigaito, M.; Sawamoto, M.; Higashimura, T., *Macromolecules* **1995,** *28*, 1721-1723.

51. Bielawski, C. W.; Louie, J.; Grubbs, R. H., *J. Am. Chem. Soc.* **2000,** *122*, 12872-12873.

52. Wang, J. S.; Matyjaszewski, K., *J. Am. Chem. Soc.* **1995,** *117*, 5614-5615.

53. Matyjaszewski, K.; Wei, M. L.; Xia, J. H.; McDermott, N. E., *Macromolecules* **1997,** *30*, 8161-8164.

54. Muhlebach, A.; Gaynor, S. G.; Matyjaszewski, K., *Macromolecules* **1998,** *31*, 6046-6052.

55. Percec, V.; Barboiu, B.; Neumann, A.; Ronda, J. C.; Zhao, M. Y., *Macromolecules* **1996,** *29*, 3665-3668.

56. Uegaki, H.; Kotani, Y.; Kamigaito, M.; Sawamoto, M., *Macromolecules* **1998,** *31*, 6756-6761.

57. Moineau, G.; Minet, M.; Dubois, P.; Teyssie, P.; Senninger, T.; Jerome, R., *Macromolecules* **1999,** *32*, 27-35.

58. Lecomte, P.; Drapier, I.; Dubois, P.; Teyssie, P.; Jerome, R., *Macromolecules* **1997,** *30*, 7631-7633.

59. Patten, T. E.; Matyjaszewski, K., *Acc. Chem. Res.* **1999,** *32*, 895-903.

60. Pintauer, T.; Matyjaszewski, K., *Coordin. Chem. Rev.* **2005,** *249*, 1155-1184.

61. Coca, S.; Jasieczek, C. B.; Beers, K. L.; Matyjaszewski, K., *J. Polym. Sci. Polym. Chem.* **1998,** *36*, 1417-1424.

62. Wang, X. S.; Lascelles, S. F.; Jackson, R. A.; Armes, S. P., *Chem. Commun.* **1999**, 1817-1818.

63. Wang, X. S.; Armes, S. P., *Macromolecules* **2000,** *33*, 6640-6647.

64. Huang, W. X.; Kim, J. B.; Bruening, M. L.; Baker, G. L., *Macromolecules* **2002,** *35*, 1175-1179.

65. Perrier, S.; Haddleton, D. M., *Macromol. Symp.* **2002,** 261-272.

66. Coullerez, G.; Carlmark, A.; Malmstrom, E.; Jonsson, M., *J. Phys. Chem. A* **2004,** *108*, 7129-7131.

67. Lee, S. B.; Russell, A. J.; Matyjaszewski, K., *Biomacromolecules* **2003,** *4*, 1386-1393.

68. Ali, M. M.; Stover, H. D. H., *Macromolecules* **2004,** *37*, 5219-5227.

69. Liu, S. Y.; Weaver, J. V. M.; Tang, Y. Q.; Billingham, N. C.; Armes, S. P.; Tribe, K., *Macromolecules* **2002,** *35*, 6121-6131.

70. Cai, Y. L.; Armes, S. P., *Macromolecules* **2004,** *37*, 7116-7122.

71. Fujii, S.; Cai, Y. L.; Weaver, J. V. M.; Armes, S. P., *J, Am. Chem. Soc.* **2005,** *127*, 7304-7305.

72. Dufresne, M. H.; Gauthier, M. A.; Leroux, J. C., *Bioconjugate Chem.*

2005, *16*, 1027-1033.

73. Haddleton, D. M.; Perrier, S.; Bon, S. A. F., *Macromolecules* **2000,** *33*, 8246-8251.

74. Nomura, E.; Ito, K.; Kajiwara, A.; Kamachi, M., *Macromolecules* **1997,** *30*, 2811-2817.

75. Oh, J. K.; Min, K.; Matyjaszewski, K., **2006,** *39*, 3161-3167.

76. Kim, J. B.; Huang, W. X.; Miller, M. D.; Baker, G. L.; Bruening, M. L., *J. Polym. Sci. A: Polym. Chem.* **2003,** *41*, 386-394.

77. Lemieux, M.; Usov, D.; Minko, S.; Stamm, M.; Shulha, H.; Tsukruk, V. V., *Macromolecules* **2003,** *36*, 7244-7255.

78. Minko, S.; Patil, S.; Datsyuk, V.; Simon, F.; Eichhorn, K. J.; Motornov, M.; Usov, D.; Tokarev, I.; Stamm, M., *Langmuir* **2002,** *18*, 289-296.

79. Mori, H.; Boker, A.; Krausch, G.; Muller, A. H. E., *Macromolecules* **2001,** *34*, 6871-6882.

80. Mori, H.; Seng, D. C.; Zhang, M. F.; Muller, A. H. E., *Langmuir* **2002,** *18*, 3682-3693.

81. Huang, W. X.; Baker, G. L.; Bruening, M. L., *Angew. Chem., Int. Ed.* **2001,** *40*, 1510.

82. Zhao, B.; Haasch, R. T.; MacLaren, S., *J. Am. Chem. Soc.* **2004,** *126*, 6124-6134.

83. Pyun, J.; Jia, S. J.; Kowalewski, T.; Patterson, G. D.; Matyjaszewski, K., *Macromolecules* **2003,** *36*, 5094-5104.

84. von Werne, T.; Patten, T. E., *J. Am. Chem. Soc.* **2001,** *123*, 7497-7505.

85. Bontempo, D.; Tirelli, N.; Masci, G.; Crescenzi, V.; Hubbell, J. A., *Macromol. Rapid Commun.* **2002,** *23*, 418-422.

86. von Werne, T.; Patten, T. E., *J. Am. Chem. Soc.* **1999,** *121*, 7409-7410.

87. Mandal, T. K.; Fleming, M. S.; Walt, D. R., *Chem. Mater.* **2000,** *12*, 3481-3487.

88. Xiao, D. Q.; Wirth, M. J., *Macromolecules* **2002,** *35*, 2919-2925.

89. Perruchot, C.; Khan, M. A.; Kamitsi, A.; Armes, S. P.; von Werne, T.; Patten, T. E., *Langmuir* **2001,** *17*, 4479-4481.

90. Zhao, H. Y.; Kang, X. L.; Liu, L., *Macromolecules* **2005,** *38*, 10619-10622.

91. Peng, B.; Johannsmann, D.; Ruhe, J., *Macromolecules* **1999,** *32*, 6759-6766.

92. Hamelinck, P. J.; Huck, W. T. S., *J. Mater. Chem.* **2005,** *15*, 381-385.

93. Zhao, B.; Brittain, W. J.; Zhou, W. S.; Cheng, S. Z. D., *J. Am. Chem. Soc.* **2000,** *122*, 2407-2408.

94. Zhao, B.; Brittain, W. J., *Macromolecules* **2000,** *33*, 8813-8820.

95. Boyes, S. G.; Brittain, W. J.; Weng, X.; Cheng, S. Z. D., *Macromolecules* **2002,** *35*, 4960-4967.

96. Pyun, J.; Jia, S. J.; Kowalewski, T.; Matyjaszewski, K., *Macromol. Chem. Phys.* **2004,** *205*, 411-417.

97. Li, D. J.; Sheng, X.; Zhao, B., *J. Am. Chem. Soc.* **2005,** *127*, 6248-6256.

98. Sun, T. L.; Wang, G. J.; Feng, L.; Liu, B. Q.; Ma, Y. M.; Jiang, L.; Zhu, D. B., *Angew. Chem., Int. Ed.* **2004,** *43*, 357-360.

99. Prucker, O.; Schimmel, M.; Tovar, G.; Knoll, W.; Ruhe, J., *Adv. Mater.* **1998,** *10*, 1073.

100. Husemann, M.; Morrison, M.; Benoit, D.; Frommer, K. J.; Mate, C. M.; Hinsberg, W. D.; Hedrick, J. L.; Hawker, C. J., *J. Am. Chem. Soc.* **2000,** *122*, 1844-1845.

101. Xia, Y. N.; Whitesides, G. M., *Angew. Chem., Int. Ed.* **1998,** *37*, 551-575.

102. Kaholek, M.; Lee, W. K.; LaMattina, B.; Caster, K. C.; Zauscher, S., *Nano Lett.* **2004,** *4*, 373-376.

103. Ma, H. W.; Hyun, J. H.; Stiller, P.; Chilkoti, A., *Adv. Mater.* **2004,** *16*, 338-+.

104. Ito, Y.; Park, Y. S.; Imanishi, Y., *J. Am. Chem. Soc.* **1997,** *119*, 2739-2740.

105. Ito, Y.; Ochiai, Y.; Park, Y. S.; Imanishi, Y., *J. Am. Chem. Soc.* **1997,** *119*, 1619-1623.

106. Ito, Y.; Nishi, S.; Park, Y. S.; Imanishi, Y., *Macromolecules* **1997,** *30*, 5856-5859.

107. Balachandra, A. M.; Baker, G. L.; Bruening, M. L., *J. Membr. Sci.* **2003,** *227*, 1-14.

Chapter II

Crystallization of Polymer Brushes

This chapter describes the crystallization of comb-like polymer brushes formed by surface-initiated atom transfer radical polymerization (ATRP) of PEG-methacrylates (PEGMA) from gold surfaces in aqueous media. Optical microscopy and atomic force microscopy (AFM) show that the ethylene oxide side chains of poly(PEGMA) crystallize to form two-dimensional spherulites. The crystal growth rates are film-thickness dependent. AFM and reflectance FT-IR measurements on < 100 nm films are consistent with formation of crystalline lamellae predominantly oriented parallel to the surface, but thicker films are mainly comprised of perpendicularly-oriented lamellae. The crystallization of polymer brushes occurs by heterogeneous nucleation and one-dimensional growth.

Introduction

Thin and ultra-thin films are attractive for tailoring surface properties because of their wide range of physicochemical properties. Studies on polymer films, primarily physically absorbed films deposited on substrates by spin-coating, show that the interactions between the substrate and polymer layers usually lead to physical properties that are different than those of the bulk polymer. For example, the glass transition temperature (T_g) may be enhanced or depressed depending on the film thickness and interfacial interactions,[1] and restriction of chain mobility greatly affects the crystallization process. Polymer morphology, [2-9] degree of crystallinity,[10, 11] preferred

polymer chain orientation, [2, 7, 12] and crystal growth rates [3,10, 11, 13-18] may vary with the film thickness.

Although physical adsorption of films on substrates is a convenient and versatile method for surface modification, the stability of physisorbed coatings is limited in the presence of good solvents. For this reason, films covalently bonded to substrates, such as polymer brushes, are being rapidly adopted for the study of thin films. Some properties of polymer brushes are unique to their architecture and have not been explored in detail. For example, the effect that the polymer brush architecture may have on crystallization is unclear since the extended chains of densely grafted brushes may pre-organize and favor crystallization, while chain entanglements and the restricted mobility of the polymer chains in these brushes may retard the crystallization process. Luzinov *et al.* [19, 20] studied the surface morphology of PEG brushes formed by reacting the end groups of activated PEGs of different molecular masses with a surface primed with poly(glycidyl methacrylate). After PEG grafting, the surface was either partially or totally covered by finger-like crystalline domains, depending on the molecular mass of the constituent PEGs. Since the thicknesses of the films were similar, the variations in crystalline morphology must be related to the grafting density and the molecular masses of the PEGs.

To further understand the effects of brush architecture on crystallization, this work examines the crystallization of comb-like polymer brushes obtained from ATRP of poly(ethylene glycol) methyl ether methacrylate (PEGMA) from initiators immobilized on Au surfaces. In the case of PEGMA macromonomers, polymerization from surfaces yields methacrylate comb polymer brushes with hydrophilic poly(ethylene oxide) (PEO) side chains as shown in Figure 2.1. The side chains of poly(PEGMA) and other comb

polymers crystallize when they are sufficiently long, irrespective of the tacticity of the polymer backbone.[21-23]

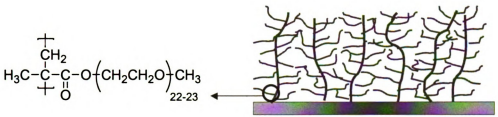

Figure 2.1. Architecture of comb-like poly(PEGMA) brushes grown from a surface.

The melting temperature (T_m) of the PEO segment in comb polymers depends on the length of side chains and ranges from below room temperature to ~65 °C, the T_m of PEO. This range is compatible with thermally unstable substrates such as self-assembled monolayers on Au, enabling detailed IR analysis of the structure and orientation of the crystalline PEO side chains. In addition to their relevance for understanding crystallization of thin films, poly(PEGMA) brushes have important potential applications as gas separation membranes and materials for limiting non-specific protein adsorption on surfaces. Studies of chain crystallization in poly(PEGMA) brushes complement extensive research on crystallization of bulk PEO,[24, 25] PEO films on surfaces,[2, 3, 14, 15] PEO segments in block copolymers,[26, 27] as well as films of PMMA/PEO blends.[7, 28, 29]

Crystalline PEO comb-polymers are usually arranged in a "sandwich" structure, with layers of amorphous backbones alternating with lamellae of crystalline side chains. For example, Inomata *et al.* suggested a crystalline lamellae packing for PEO side chains of poly(MMA-*stat*-PEGMA), with amorphous backbone connecting lamellae.[23]

Neugebauer *et al.* proposed a model of alternating disordered and crystalline domains for polymethacrylates with PEG and alkyl side chains. [21]

Although the chain conformations in adsorbed films and brushes are different, polymer crystallization studies of physisorbed films provide a useful starting point for understanding the crystallization of brushes. As film thickness decreases to nm dimensions in the physisorbed polymer films, the spherulitic morphology observed in bulk polymers evolves into sheaf-like aggregates,[6,7, 30] or finger-like patterns for monolayer films.[9, 31, 32] AFM makes it possible to observe individual lamellae in spherulites. For most ultra-thin polymer films studied to date, crystalline lamellae preferentially orient parallel to the substrate, with the polymer chain axis oriented normal to the surface. The orientation of crystalline lamellae may change with the film thickness, and lamellae oriented parallel to the surface may give way to perpendicular lamellae as the film thickness increases. For example, Schönherr *et al.*[2] studied PEO films and reported crystalline lamellae oriented parallel to the substrate when the films were < 300 nm thick, and perpendicular lamellae for film thickness > 1 μm. This trend in lamellae orientation was also found in crystalline low density polyethylene (LDPE) films[7] and poly(di-*n*-hexylsilane) films.[12] The accepted explanation for these thickness effects is that perpendicular orientation minimizes the energy for the primary nucleation step, and therefore, the same orientation is favored for secondary nucleation and crystal growth, resulting in the favored perpendicular lamellae orientation. In ultra-thin films, lamellae lying flat on the surface reduce the surface energy more effectively and are favored over perpendicular lamellae.

Frank *et al.*[11] reported that the crystallization rate and crystallinity of poly(di-*n*-hexylsilane) films decreased significantly when the film thickness was < 50 nm. Since then, several research groups confirmed a reduction in crystal growth rates as film thickness decreased, but conflicting results remain regarding the correlation between film thickness and crystal growth rate. Taguchi *et al.*[16] studied the growth rate of isotactic polystyrene films and claimed that the film growth rate (G) can be related to film thickness (d) using a simple equation: $G(d) = G(\infty)\ (1- a/d)$, where $G(\infty)$ refers to the growth rate of bulk polymer, and the constant a is ~ 6 nm. In contrast to the above results, Schönherr *et al.*[2] studied isothermal crystallization of PEO films on silicon substrates, and concluded from an Avrami analysis of FT-IR data that the crystallite growth rate and film thickness have an exponential relationship, i.e, $G(d) = G(\infty)\ exp\ (1- constant/d)$. Dalnoki-Veress *et al.*[14, 18] studied isothermal crystallization of PEO films ranging from 13 nm to 2 μm, and reported a non-monotonic decrease in crystal growth rate for film thickness > 40 nm, which they related to morphology changes.

This chapter describes the synthesis and characterization of crystalline polymer brushes with an emphasis on the effect of film thickness on morphology, chain orientation in crystallites and the crystallization rate. The crystallization kinetics for brushes is interpreted in the context of the Avrami-Evans theory.

Experimental Section

Materials. Poly(ethylene glycol) methyl ether methacrylate (PEGMA, M_n=1,100 g/mol), Cu(I)Br (99.999%), Cu(II)Br_2 (Aldrich, 99.999%), and 11-mercapto-undecanol [$HS(CH_2)_{11}OH$] were used as received. 2,2'-Bipyridine (bpy) was recrystallized from hot hexane and sublimed under vacuum at 60 °C. The disulfide initiator ($((CH_3)_2CBrCOO(CH_2)_{11}S)_2$) was synthesized using a slightly modified version of a literature procedure.[33] Deionized water (Milli-Q, 18 MΩcm) was used as the polymerization solvent.

Synthesis of initiator [Br-C(CH$_3$)$_2$-COO(CH$_2$)$_{11}$S)$_2$] [33] CH_2Cl_2 (150 mL), 10% aqueous potassium bicarbonate (20 mL) and 11-mercaptoundecanol (4.0 g) were added to a 250 mL Schlenk flask. Bromine (0.51 mL) was slowly syringed into the well-stirred mixture, and the initial orange-red color of bromine quickly disappeared. After continued stirring for 2 h, the organic and water layers were separated, and the water layer was extracted with 50 mL of CH_2Cl_2. The combined organic layers were dried over $MgSO_4$, filtered, and evaporated to dryness to yield 2.95 g (75%) of $HO(CH_2)_{11}S$-$S(CH_2)_{11}OH$ (**1**) as a white powder. ^{1}H-NMR (300 MHz, $CDCl_3$): δ 1.23 (br, 32H, CH_2), 1.52 (m, 4H, CH_2), 1.62 (m, 4H, CH_2), 2.62 (t, 4H, SCH_2), 3.61(t, 4H, OCH_2). Under a blanket of Ar, 2-bromoisobutyryl bromide (1.46 mL) was added drop-wise to a 0 °C solution of disulfide [**1**] (2.0 g, 5 mmol) and triethyl amine (3.4 mL, 0.07 mol) in 120 mL CH_2Cl_2. After stirring at 0 °C for 1 h, and at 25 °C for 2 h, the solution was filtered to remove triethylamine hydrobromide and then extracted with 2N sodium carbonate solution saturated with aqueous ammonium chloride (2 × 50 mL). The dichloromethane was removed by rotary evaporation and the crude product was purified by column

chromatography using 10:1 hexane/ethyl acetate as the eluent. Removal of the solvent provided 1.5 g of the initiator (43%) as a pale yellow viscous liquid. ^{1}H-NMR (300 MHz, $CDCl_3$): δ 1.31 (br, 28H), 1.7 (br, 8H), 1.9 (s, 12H), 2.7(t, 4H, J = 7.3), 4.18 (t, 4H, J = 6.6). ^{13}C-NMR: δ 172 (C=O), 66.4 (OCH_2), 56.2 (C), 39.4 (SCH_2), 31.0(CH_3), 29.7(CH_2), 29.5(CH_2), 29.4(CH_2), 28.7(CH_2), 28.6(CH_2), 26.0(CH_2). Anal. Calcd. for $C_{30}H_{56}Br_2O_4S_2$: C, 51.13; H, 8.01. Found C, 51.27; H, 7.69.

Scheme 2.1. Synthetic procedure for preparation of initiator **2**

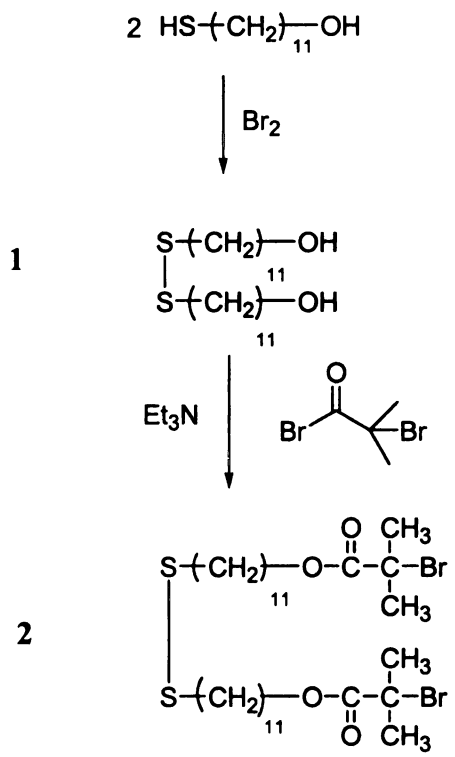

Preparation of immobilized initiators on Au surfaces. Gold-coated wafers (200 nm of gold sputter-coated on 20 nm of Cr on Si (100) wafers) were UV/O_3-cleaned for 15 min before use. After washing with water and ethanol, the slides were immersed in a 1

mM solution of disulfide initiator **2** in ethanol for 24 h to form the self-assembled monolayer. The films were washed with ethanol, sonicated in ethanol for 1 min, again washed with ethanol, and then dried under a stream of N_2. The substrates were characterized by ellipsometry and by reflectance FT-IR.

Surface-initiated polymerization of PEGMA. PEGMA (35 g, 0.032 mol) and 20 mL of Milli Q water were added to a Schlenk flask and stirred until the PEGMA completely dissolved. The flask was connected to a vacuum line and the solution was degassed by three freeze-pump-thaw cycles, and finally backfilled with Ar. Under a blanket of Ar, CuBr (0.024 g), $CuBr_2$ (0.011 g), and bpy (0.077 g) were added to the solution, and the mixture was stirred for at least 1 h to form a homogeneous dark brown solution. The solution of monomer and catalyst ([CuBr] = 1 mM, [$CuBr_2$] = 0.3 mM, and [bpy] = 3 mM) was transferred into a N_2-filled glovebag and added to a series of vials, each containing one initiator-anchored slide. Slides were removed from vials at predetermined times, and the polymer films grown from the gold surfaces were rinsed sequentially with water, THF, and anhydrous ethanol. The films were then dried under a stream of N_2,

Solution ATRP of PEGMA. PEGMA (20 g, 0.018 mol) and 15 mL of water were added to a Schlenk flask. The flask was connected to a vacuum line and degassed via three freeze-pump-thaw cycles. CuBr (0.065 g, 0.45 mmol), $CuBr_2$ (0.034 g, 0.15 mmol) and bpy (0.14 g, 0.9 mmol) were added to the mixture under Ar, and the solution was stirred until a homogeneous dark brown solution was formed. Degassed ethyl 2-bromoisobutyrate (0.18 g, 0.9 mmol) was syringed into the reaction mixture to initiate the polymerization. The solution became increasingly viscous and after 2 h, the

polymerization was quenched by exposing the solution to air. After dilution with water or THF, the resulting blue solution was filtered through a short silica column to remove the copper catalyst. Removal of the solvent yielded 5 g of poly(PEGMA) as a white solid. ^{1}H-NMR indicated > 99 % conversion of PEGMA (see Figure 2.15). M_n = 60,000 g/mol.

Characterization methods. Reflectance FT-IR was performed using a Nicolet Magna-IR 560 spectrometer with a PIKE grazing angle of 80 °C. Reflectance FT-IR experiments used *p*-polarized light. Since only transition moment components perpendicular to the surface provide absorption peaks in the spectra, the molecular conformation of samples were inferred from IR absorption spectra using the previously reported PEG assignments. Film thicknesses were measured by a rotating analyzer ellipsometer (M-44; J.A. Woollam) at an incident angle of 75°. The data were analyzed using WVASE32 software, and the thickness and refractive index determinations were performed on at least three spots on each substrate. The refractive index was fitted with the film thickness, and the measured refractive index was around 1.5. AFM images were measured using the close-contact mode of a nano-R^{TM} instrument, and both height and phase images were recorded simultaneously. The silicon tip was used with a spring constant of 36 N/m, with tip curvature of 10-20 nm, and a resonance frequency of 286-339 KHz. The scan rate was set to 0.85 Hz and the set-point was adjusted to optimize image quality.

Crystallization studies. The morphology of crystalline polymer brushes were imaged using Nikon Optiphot2-POL polarizing optical microscope equipped with a Mettler FP 82 hot-stage and a CCD camera. Samples for isothermal crystallization experiments were heated at 50 °C for 8 h in a vacuum oven to erase the thermal history of

the film. The films were immediately transferred to the hot stage, and held at 23 ± 2 °C under a flow of N_2. In non-isothermal crystallization experiments, the samples were loaded into the hot stage and heated to 45 °C (above the melting temperature), and then cooled at 2 °C /min to ambient temperature, and further cooled at 1 °C /min to ~5 °C by purging the hot-stage with the boil off from liquid N_2. For other experiments, the slides were cooled to ambient temperature in a desiccator under reduced pressure or under N_2.

Polymer solutions for spin-coating were prepared as 1-10 wt % solutions in solvent CH_2Cl_2 and filtered through 0.02 μm PTFE filters. All films were deposited at 3000 rpm, with the film thickness controlled by varying the concentration of the polymer solution. After spin-coating, the films were dried under vacuum and annealed at 30 °C. The films were characterized by external reflectance FT-IR and by ellipsometry.

Results and discussion

Preparation of polymer brushes. Scheme 2.1 shows the synthetic route used to grow poly(PEGMA) from gold. Methacrylates containing 4-5, 8-9, and 22-23 ethylene oxide repeat units were polymerized, but only poly(PEGMA) with 22-23 PEO units crystallized at room temperature. Research on bulk poly(PEGMA) shows that the atactic backbone of poly(PEGMA) and a portion of side chains adjacent to the backbone constitute an amorphous phase, and the ethylene oxide chain must exceed a minimum chain length, typically 9-10 ethylene oxide units to crystallize. In the remainder of this chapter, PEGMA refers to the methacrylate with 22-23 PEO units, unless otherwise specified. Polymerization studies of other PEG methacrylates appear in Chapter III.

Immobilization of the initiator was confirmed by the appearance of a carbonyl peak in the reflectance FT-IR spectrum (Figure 2.2a) as well as formation of a 17 ± 2 Å-thick film, as measured by ellipsometry. The PEGMA macromonomer was polymerized from the surface using aqueous solution containing the $CuBr/CuBr_2$/bpy ATRP catalyst. During the first 8 h of the polymerization, the film thickness increased linearly with polymerization time, consistent with a controlled polymerization (see Figure 2.3), but at longer times, the film growth rate decreased, which may reflect reaction of active chain ends with adventitious oxygen in the glovebag.

IR spectra of the films (Figure 2.2b) show characteristic bands for poly(PEGMA): C-H stretching (2950-2800 cm^{-1}), C=O stretching (1740 cm^{-1}), CH_2 bending (1460 cm^{-1}), CH_2 wagging (1350 cm^{-1}), overlapping CH_2 twisting (~1300-1240 cm^{-1}), and a broad C-O-C stretching band (1150 cm^{-1}). The width and position of the IR peaks are consistent with an amorphous polymer brush film. As described below, the evolution of the IR bands indicates that these films crystallize at room temperature.

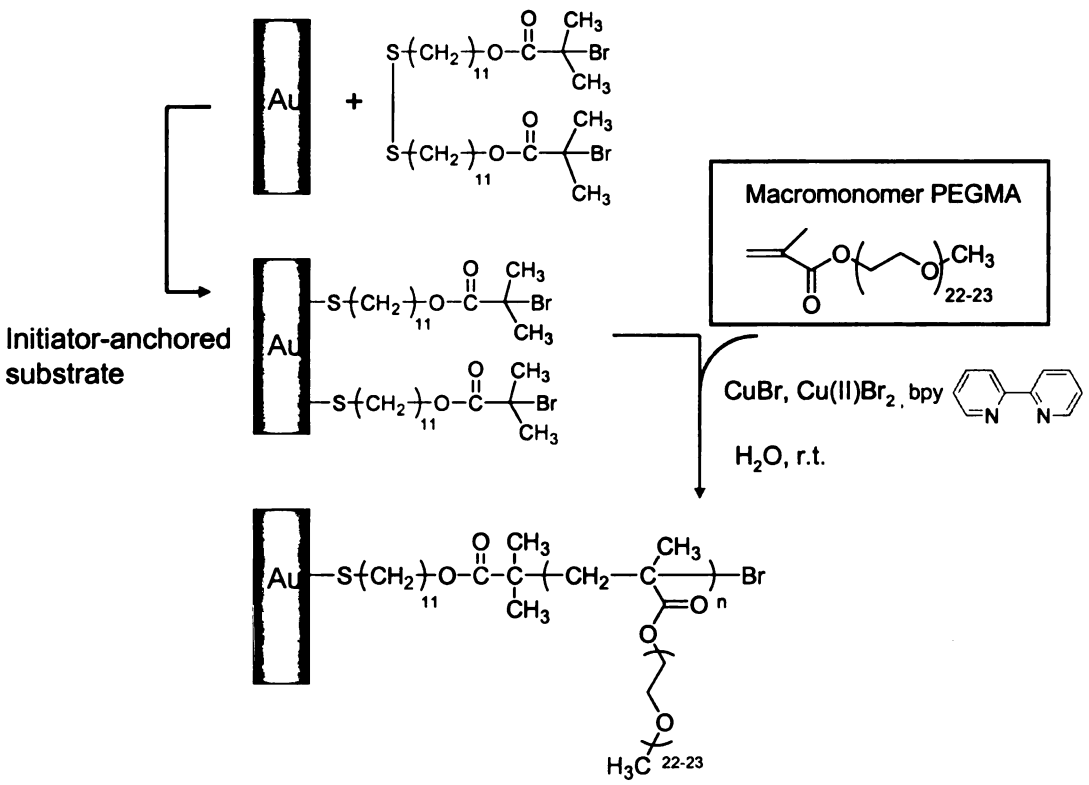

Scheme 2.2. Growth of poly(PEGMA) films from gold.

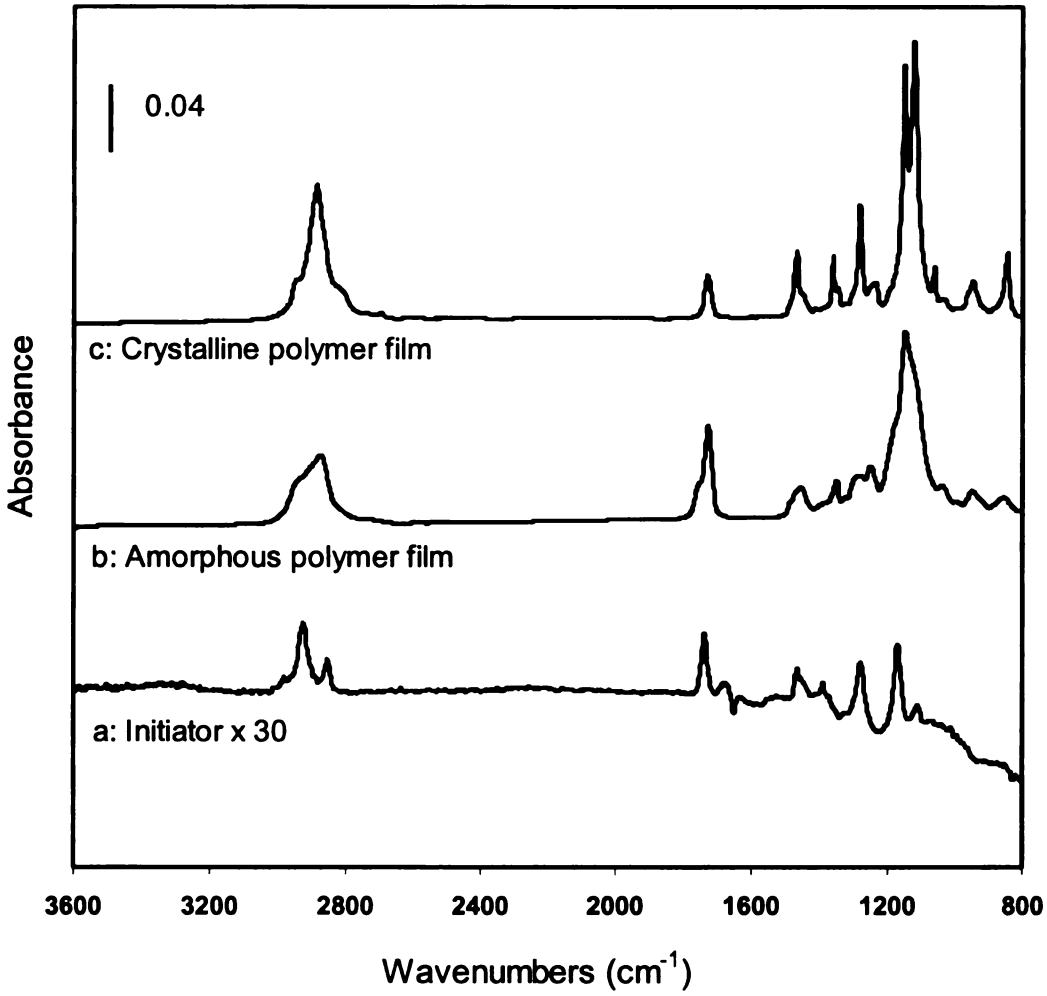

Figure 2.2. Reflectance FTIR spectra of (a) an initiator monolayer, and (b) an amorphous 114 nm thick poly(PEGMA) film. Spectrum b was taken immediately after its synthesis. Trace (c) shows a poly(PEGMA) film of the same film thickness after crystallization at room temperature.

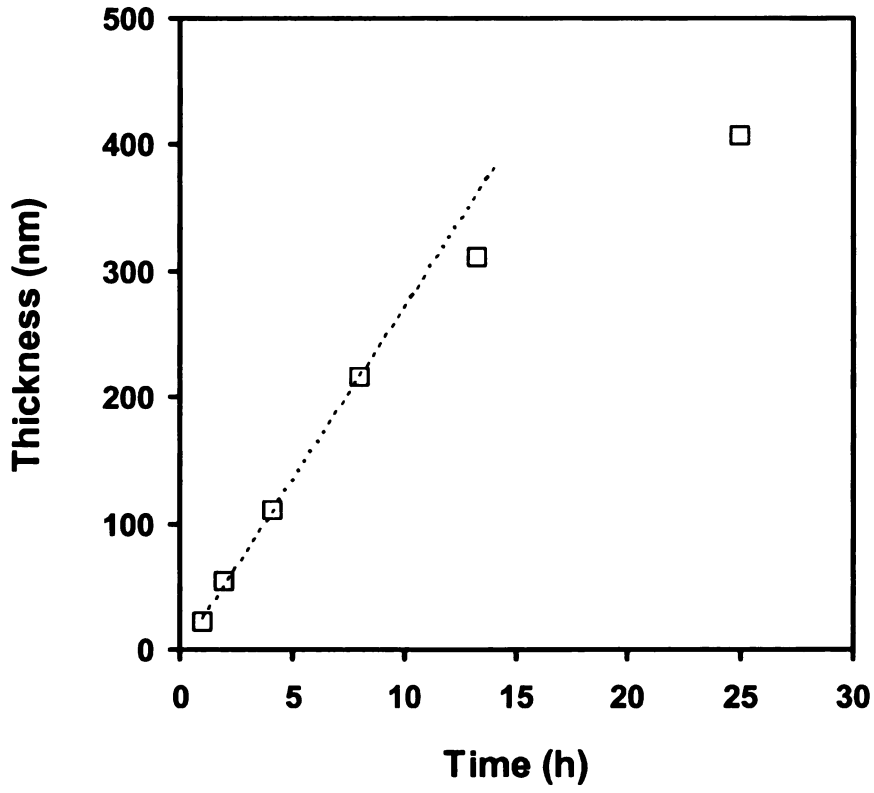

Figure 2.3. Evolution of the ellipsometric film thickness with time for the ATRP of PEGMA at room temperature from initiators anchored to gold surfaces. Conditions: [CuBr] = 1 mM, [$CuBr_2$] = 0.3 mM, [bpy] = 3 mM, and [M]:[H_2O] = 2:1 (v/v).

Morphology of crystalline polymer brushes. The optical microscopy experiments described here provide a qualitative picture of the crystallization behavior as a function of temperature and film thickness. While stored at room temperature, the films crystallized and the mirror-like finish of as-prepared films developed surface features that were visible to the naked eye. When observed between crossed polarizers, the as-prepared polymer films initially appeared dark (amorphous), but eventually the Maltese cross patterns characteristic of spherulites filled the field of view. The images shown in Figure 2.4 are from samples annealed at 45 °C and then cooled to the desired temperature. Since the T_m of poly(PEGMA) films are ~35-40 °C, the super-cooling ($\Delta T = T_c - T_m$) at ~5 °C supports a sufficiently high crystallization rate to enable crystallites to be observed in a short period of time.

Panels a and b in Figure 2.4 show the evolution in polymer morphology for a 240 nm-thick film. At 10 °C, large and well-defined "spherulites" cover most of the field of view. The domains have similar radii, consistent with nucleation of each domain at comparable times. At 5 °C, the crystalline domains grow to cover the entire surface, as shown in panel b. These disc-like domains are large, ~100 nm in diameter but only 240 nm thick, resulting in an aspect ratio comparable to digital video discs (DVDs). Given their symmetry and disc-like geometry, the domains may be viewed as a 2-dimensional slice through the center of a spherulite. Crystallization under isothermal conditions at room temperature under N_2 also produced films with spherulitic morphologies.

Panels b, c and d show the effects of film thickness on crystallization. All three samples were imaged at 5 °C under comparable conditions. While the 240 nm film was fully crystallized, some areas of the 148 and 76 nm films remained amorphous. The 76

nm film appeared as sheaf-like aggregates, which may be typical of the early stages of spherulite development. These observations show that the crystallization behavior poly(PEGMA) films is similar to thin PEO films, and that both the crystalline morphology and crystallization rate depend on the poly(PEGMA) film thickness.

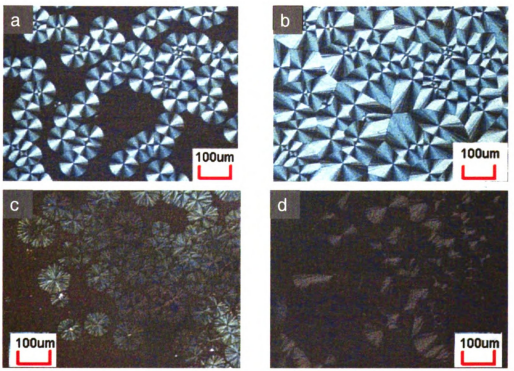

Figure 2.4. Optical micrographs of poly(PEGMA) brushes grown from gold surfaces and viewed through crossed polarizers: (a) and (b) show the crystallization of a 240 nm at 10 °C and at 5 °C, respectively; (c) and (d) show the crystallization of 148 nm and 76 nm, films, respectively at 5 °C. Images in this dissertation are presented in color.

AFM measurements provided a more detailed view of the crystalline polymer brush morphology. Figure 2.5 shows flat and 3-D height images obtained for a 108 nm film. Panel a shows a clearly resolved boundary (*1*) between two spherulitic domains and well-defined perpendicular lamellae (*2*) that emanate from the center of the "spherulite". Panel b shows the apparent overlap of two spherulitic domains, possibly at the site of a film defect, resulting in twisted branches and a more irregular boundary between the two domains.

The evolution of film morphology with thickness was examined using 20-300 nm films that were crystallized under identical conditions (isothermal crystallization). Figure 2.6 shows AFM images for 122 and 310 nm films. The image of the 310 nm film shows thick, closely packed perpendicular lamellae. The observed branching of lamellae in the 122 nm film is the expected consequence of the radial growth of "spherulites".

The morphologies of films < 100 nm are more complicated and are thickness-dependent. Panel a of Figure 2.7 Compared to thicker films, the lamellar morphology seen in the height image is less resolved, but more clearly shown in the phase image. The morphology of the 70 nm film is similar to that of the 92 nm film. A switch from perpendicularly oriented lamellae to lamellae presumably lying parallel to the surface came from the image of a 55 nm film, which clearly shows a worm-like film morphology that resembles aggregates of lamellae parallel to the surface (Figure 2.8). As the film thickness decreased to 35 nm, however, the AFM image of the film appeared homogeneous and nearly featureless, suggesting either an amorphous film, or a morphology dominated by parallel lamellae.

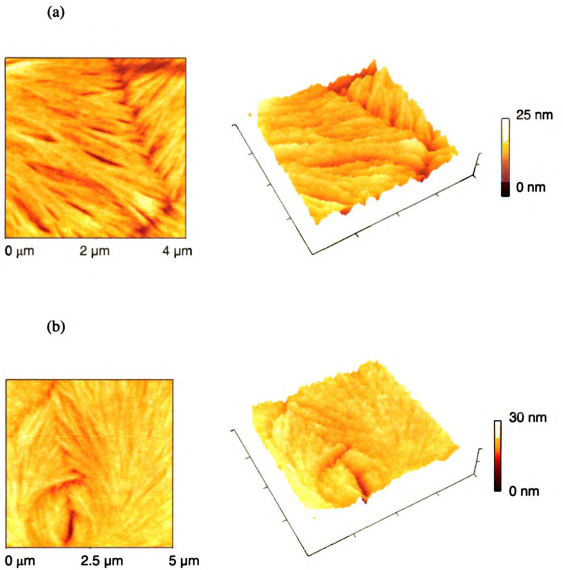

Figure 2.5. AFM images of a 108 nm crystalline polymer brush film. At left are the height images and at right are the corresponding 3-D views. In panel a, the scan distance is 4 × 4 μm, with a z distance of 25 nm. In panel b, the scan distance is 5 × 5 μm, and the z distance is 30 nm. Images in this dissertation are presented in color.

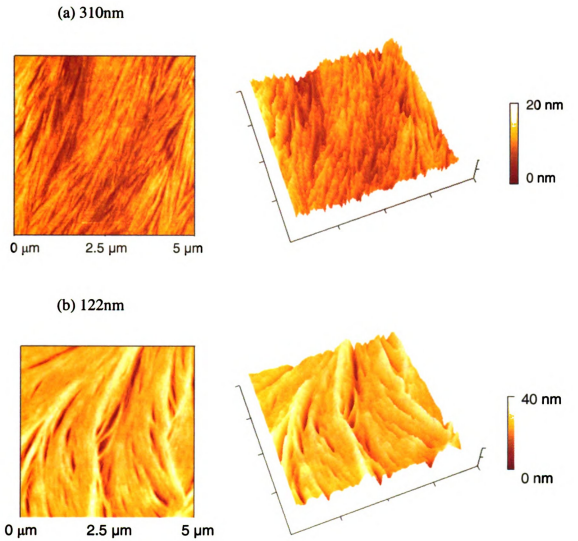

Figure 2.6. AFM images of crystalline polymer brushes. (a) shows data for a 310 nm thick film and (b) shows data for a the 122 nm film. Both image are 5 × 5 μm, and the heights of the 310 and 122 nm films are 20 and 40 nm, respectively. Images in this dissertation are presented in color.

Figure 2.7

(a) 92 nm

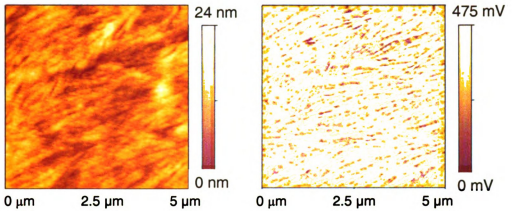

(b) 70 nm

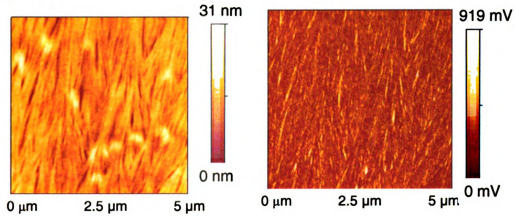

(c) 35 nm

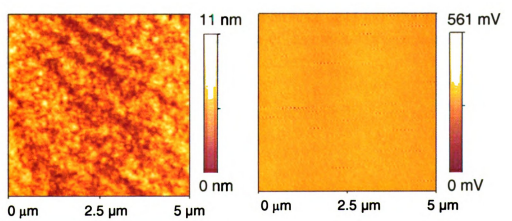

Figure 2.7. (Left) AFM height images (5 × 5 μm) of crystalline polymer brushes with thickness of: (a) 92 nm, z distance is 24 nm; (b) 70 nm, z distance is 31 nm; (c) 35 nm, z distance is 10 nm. (Right) Phase images of crystalline polymer brushes with thickness of: (a) 92 nm, z distance is 475 mV; (b) 70nm, z distance is 919 mV; (c) 35 nm, z distance is 561 mV. Images in this dissertation are presented in color.

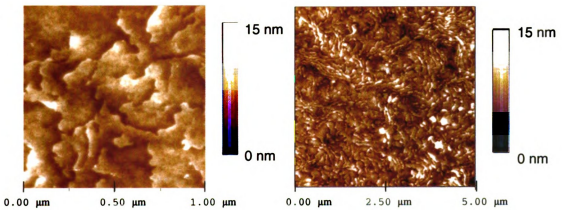

Figure 2.8. AFM height images of a crystalline film with thickness of 55 nm. Scan distance of the left image is 5 × 5 μm with a z distance of 15 nm. The scan distance in the right image is 1 × 1 μm with a z distance of 15 nm. Images in this dissertation are presented in color.

Spectroscopic characterization

Reflectance FT-IR measurements can provide spectroscopic confirmation of crystallization and information on the orientation of the poly(PEGMA) side chains relative to the surface. As seen in Figure 2.2c, crystallization causes several poly(PEGMA) IR bands to sharpen. Notable changes consistent with crystallization include the C-O-C band at 1150 cm^{-1} splitting into strong peaks at 1120 and 1148 cm^{-1}, and the CH_2 wagging peak at ~1350 cm^{-1} evolving into a sharp peak at 1360 cm^{-1} with a small shoulder at 1345 cm^{-1}. Both indicate a high degree of crystallinity for the PEO chain.

PEO usually crystallizes as a 7_2 helix, which contains seven CH_2CH_2O repeat units and two turns of the helix in the 19.3 Å between equivalent sites along the helix. The PEO chain in the helix is a succession of nearly trans (CCOC), trans (COCC), and gauche (OCCO) conformations along the chain.[24, 25] This structure, shown in Figure 2.9, has been confirmed by X-ray measurement as well as extensive spectroscopic studies. PEO adopts a planar zig-zag conformation under tension,[34] but when the stress is removed, the zig-zag conformation disappears rapidly.

The symmetry of the IR bands for the helical PEO have been assigned to two species, one with transition moment parallel to the helical axis, and the other with transition moment perpendicular to the helical axis (See Table 2.1).

Top view

Side view

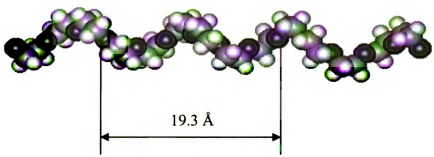

Figure 2.9. Crystalline structure of PEO with top view and side view.

Polymer brushes with different film thicknesses were characterized by reflectance FT-IR spectroscopy (Figure 2.10). All films were annealed at 50 °C to erase their thermal history, and then held at room temperature until crystallization was complete. Trace a is the IR spectrum of a 13 nm-thick film, and the width and position of the peaks indicate that this film was amorphous. All films of comparable thickness (< 20 nm) proved to be amorphous, possibly because the restricted conformations of ultrathin films prevent efficient packing of the PEO side chains into crystalline lamellae. Another possibility is that films < 20 nm thick have melting points at or below room temperature. However, the the latter seems unlikely, since a 300 nm film melts at 38 ± 1 °C, and the melting point only decreases to 34 ± 1 °C for a 80 nm film.

Table 2.1. Absorption band assignments for crystalline PEO

Band assignment [a,b]	**Transition moments** [c]	**Wavenumber (cm^{-1})** [a]	**Wavenumber (cm^{-1}) (this study)**
$\delta(CH_2)$	⊥	1473,1466	1467
$\delta((CH_2)$	∥	1461,1453	*d*
w (CH_2)	⊥	1358	1360
w (CH_2)	∥	1342	1344
t (CH_2)	⊥	1278	1280
t (CH_2)	∥	1240	1242
υ(CO)	⊥	1147	1148
υ(CO)	⊥	1116	1120
υ(CO)	∥	1103	*e*
υ(CO)+r(CH_2)+υ(CC)	⊥	1060	1062
r (CH_2)+ υ (CH_2)	∥	958	964
r (CH_2) + υ(CC)	⊥	947	947
r(CH_2)+υ(CO)	⊥	844	843

[a] Ref *24,29* [b] δ = scissor; w = wag; t = twist; υ = stretch; r = rock. [c] ⊥ and ∥ represent polarization direction perpendicular and parallel to the helical axis of PEO, [d] overlapped. [e] not observed.

The IR spectrum of a 35 nm thick film (spectrum b) shows only four peaks between 1400 and 900 cm^{-1} (1344, 1242, 1120, 964 cm^{-1}). The CH_2 wagging (1360, 1344 cm^{-1}), CH_2 rocking (964, 947 cm^{-1}) and combination bands (843 cm^{-1}) are sensitive to the conformation order.[24] Absorption peaks at 1344, 1242, and 964 cm^{-1} in trace b correspond to vibrations with transition moments parallel to the PEO helical axis. Moreover, since the reflectance FT-IR measurements used *p*-polarized light with the active transition moment normal to the surface, the helical axis of ethylene oxide units was oriented perpendicular to the substrate.

The FT-IR spectra evolved as the film thickness increased. Spectrum c shows a small band at 1148 cm^{-1}, which appears as a shoulder of the 1120 cm^{-1} band. Splitting of this C-O-C absorption confirms crystallization of the ethylene oxide segments. In addition to the 1344 and 1242 cm^{-1} bands seen in thinner films, there are new absorptions at 1360 and 1280 cm^{-1}. These bands are more obvious in trace d. The 1360, 1280, 1148, 947 and 843 cm^{-1} bands correspond to vibrations with transition moments perpendicular to the helical axis. Thus, there are two populations of helical PEO in 92 nm thick film, one with its axis perpendicular to the surface and the other parallel to the surface. In thicker films (traces e and f), the 1360, 1280, 947 and 843 cm^{-1} bands dominate indicating an increasing proportion of PEO segments oriented parallel to the surface.

The FT-IR data confirm the previous interpretations of the AFM images. The morphology of films >100 nm thick appears to be dominated by perpendicularly oriented lamellae, since polarized FT-IR measurements identify the dominant helix orientation in these films as parallel to the surface, and hence consistent with lamellae oriented normal to the surface.

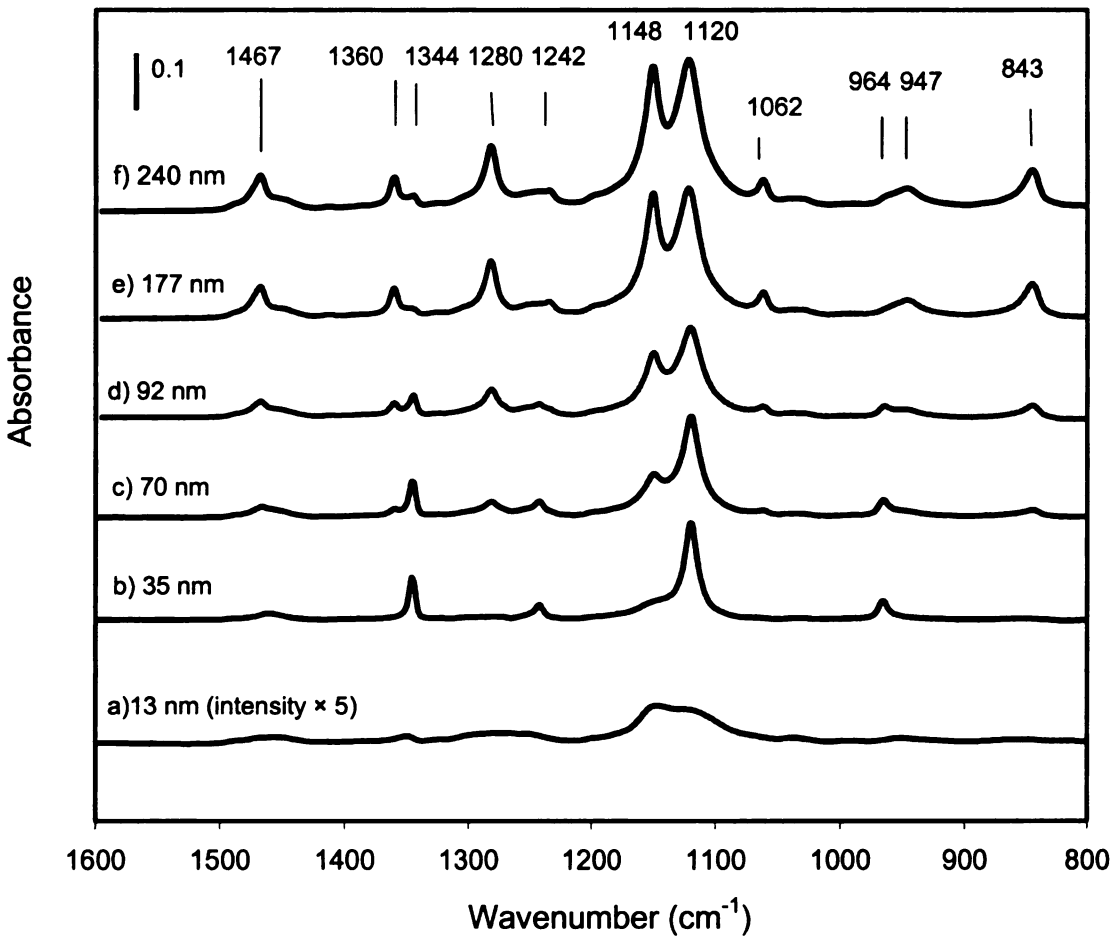

Figure 2.10. Reflectance FTIR spectra of poly(PEGMA) brushes of various thicknesses; a) 13 nm; b) 35 nm; c) 70 nm; d) 92 nm; e) 177 nm; f) 240 nm. The brushes were initially annealed at 50 °C and then allowed to crystallize at room temperature in N_2.

The morphologies of films <100 nm thick are more complicated, with AFM showing a progressive loss of perpendicular lamellae as films become thinner. For very thin films such as the 35 nm thick film shown in Figure 2.7, the AFM image was featureless, but FT-IR detected relatively sharp bands at 1342 and 1242, 1120, and 964 cm^{-1} indicating some order, and by inference, crystallinity. In contrast, the 55 nm film of Figure 2.8 shows signs of structure in the AFM image, different than seen in thicker films, suggesting lamellae oriented parallel to the surface. The FT-IR spectra of thin films are consistent with such a conclusion.

IR measurements indicate that the PEO chains in the 92 and 70 nm-thick films are orientated both parallel and perpendicular to the surface. AFM only showed irregular perpendicular lamellae, possibly due to the overgrowth of perpendicular lamellae on the top of parallel lamellae. In addition, AFM usually detects the top layer morphology of the film, while vibrational bands shown in the IR spectra reflect mean orientations of polymer chains.

The two orientations for crystalline lamellae in films are shown in Figure 2.11. Crystallization of thin polymer brushes in lamellae parallel to the surface would reduce the polymer and surface interaction, which is favorable. Rafailovich *et al.*[7] claimed that for the crystallization of thick LDPE films, the energy of the primary nucleation step is minimal when the chains are oriented parallel to the surface. However, as described in later sections of this chapter, crystallization of poly(PEGMA) occurs by heterogeneous nucleation. Formation of perpendicular lamellae also may be driven by comb-like structure of poly(PEGMA), which favors effective side chain interactions when the side chains are oriented parallel to the surface. Bulk comb polymer samples typically

crystallize in layers with the crystalline side chains oriented roughly perpendicular to the backbone. Densely packed comb polymer brushes favor an extended polymer backbone when the surface density is high enough, with the polymer backbones roughly oriented perpendicular to the surface and the side chains parallel to the surface. Crystal growth follows the same orientation, leading to the perpendicular lamellae. A similar side chain orientation was described recently by Gabriel *et al.*[35]

In addition to identifying chain orientation, IR spectroscopy suggests that films must be >20 nm to exhibit detectable crystallinity. Several groups studied spin-coated PEO films and reported different results regarding the critical film thickness for crystallization. Schönherr *et al.*[2] did not detect crystallinity in films < 15 nm. However, Reiter *et al.* [9, 32] reported crystallization in monolayer-thick films (~ 5 nm). The poly(PEGMA) case is structurally different from spin-coated PEO. First, the backbones of comb-like structures usually interfere with crystallization side chain segments adjacent to the polymer backbone, which should lead to a higher critical thickness for crystallization than linear PEO films. (We note that the melting point of the poly(PEGMA) brushes are significantly lower than linear PEO, which suggests a lower thermodynamic stability). In addition, polymer brushes with high graft densities may be viewed as pre-organized for crystallization, but more restricted in terms of available chain conformations. More detailed studies of the crystallization rates will illuminate the importance of these issues.

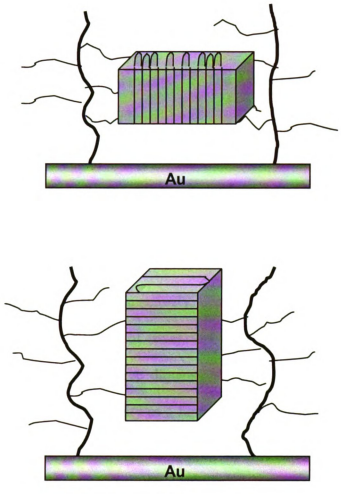

Figure 2.11. Lamellae orientations in the films of poly(PEGMA): (a) Chain axis of PEO side chains is oriented perpendicular to the substrate, lamellae parallel to the surface; (b) Chain axis of PEO side chains is parallel to the substrate, perpendicular lamellae.

Crystallization kinetics of polymer brushes.

The classical method used to interpret the growth of polymer spherulites is the application of the Avrami-Evans theory.[36-39] The Avrami equation is

$$v_c/v = 1 - \exp(-Kt^n) \qquad \text{Eq.1.}$$

where v_c/v is the volume percent crystallinity, t is the crystallization time, K is a crystallization rate constant, and n is the Avrami exponent, a parameter that reflects the dimensionality of crystal growth. For athermal nucleation (homogeneous), all nucleation events occur at $t = 0$, and n can have values of 1, 2, and 3, corresponding to one, two, and three dimensional growth, respectively. For thermal nucleation (heterogeneous), nucleation occurs as a function of time), and n can have values of 2, 3, and 4, which correspond to one, two and three dimensional growth.[40, 41] The Avrami exponent is obtained by measuring crystallinity as a function of time and analyzing the experimental data using equation 2, a logarithmic version of equation 2.1.

$$\log [- \ln (1 - v_c/v)] = n \log t + \log K \qquad \text{Eq. 2.}$$

where n and K are extracted from the slope of a plot of $\log [- \ln (1 - v_c/v)]$ *vs.* $\log t$ and the intercept, respectively.

The crystallization of thin polymer brush films is conveniently monitored by optical microscopy, which allows real-time imaging of the growth of individual spherhulites. The volume percent crystallinity in thin films can be approximated as:

$$v_c/v \sim A_c/A \sim f_c \pi r^2 / \pi R^2$$

where A_c and A are the crystalline area and the total area observed, respectively. For the case of a single spherulite, the radius r is tracked over time and related to R, the radius of the fully grown spherulite with a degree of crystallinity f_c.

The crystallization rates for a series of poly(PEGMA) thin films of various thickness were measured using polarized optical microscopy. Prior to crystallization, the films were annealed at 50 °C for 12 h to erase their thermal history. The films were immediately inserted into a hot stage purged with N_2, quenched to 23 ± 2 °C, and the evolution of the film morphology was captured by a video camera. Figure 2.12 shows the growth of spherulites in a 240 nm thick poly(PEGMA) film. The use of the term "spherulite" is technically correct only at the initial stages of crystallization, when the radius of the spherulite is less than the film thickness. This stage lasts only a few seconds and the radii of the spherulites quickly exceed the film thickness. With radii > 50 μm, these disk-like objects correspond to a slice through the center of a "spherulite", a cylindrical crystallite.

The "spherulite" growth rates were measured for films of different thicknesses and plotted as a function of time (Figure 2.13a). For each sample, a constant growth rate ($G = dR/dt$) of 0.02 to 0.07 μm/s was observed, which increased with film thickness. The average spherulite growth rate is plotted in Figure 2.13b. The growth rate increases with film thickness (regime I), but then appears to level off for films >300 nm (regime II). The increase in crystal growth rate is likely due to an increase in the average chain mobility of longer chains, enabling side chains interact with each other and incorporate into the lamellar structure more easily. At film thickness > 300 nm, the effect of the surface-anchoring on chain mobility has a minor influence on crystal growth, resulting in growth rates independent of film thickness.

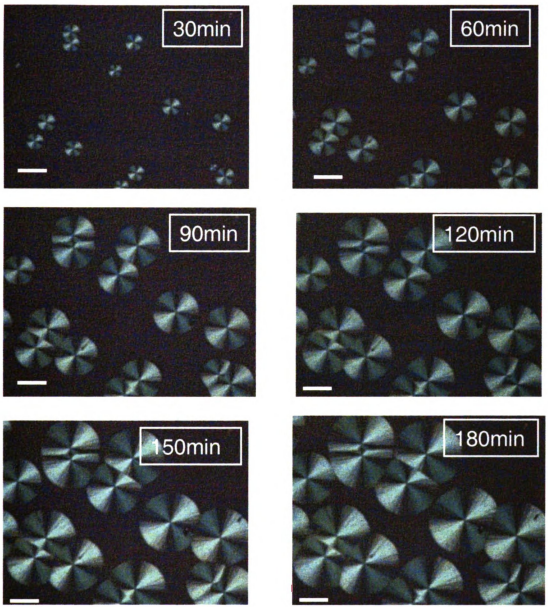

Figure 2.12. Optical micrographs showing the growth of spherulites in a 240 nm thick film at 23 ± 2 °C. The samples are viewed using crossed polarizers. The scale bar represents 100 μm. Images in this dissertation are presented in color.

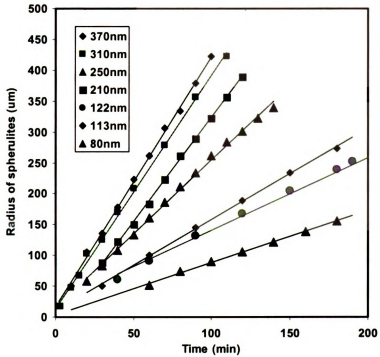

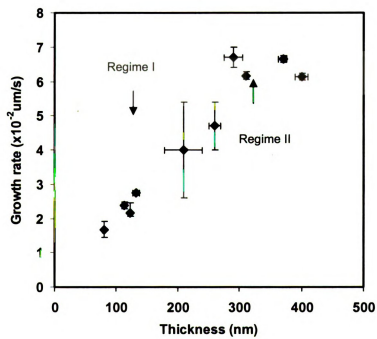

Figure 2.13 a) The evolution of spherulite radii with time for the crystallization of poly(PEGMA) brush films of various thickness at room temperature. **b)** Spherulite growth rates measured as a function of the poly(PEGMA) film thickness.

The linear fit of the Avrami equation to the experimental data is shown in Figure 2.14. For all data sets, the Avrami exponent extracted from the slopes was ~2, which is consistent with either homogeneous nucleation (athermal) and two-dimensional growth or heterogeneous nucleation (thermal), and one-dimensional growth (see Table 2.2.). For homogeneous nucleation, the distribution of nuclei in the film should be random, and therefore, the nucleation pattern in a given film should be different each time it is crystallized. For heterogeneous nucleation, secondary nucleation may occur at defect sites, and assuming the sites are not lost, the nucleation pattern should be conserved in a subsequent crystallization.

Table 2.2. Avrami exponent ***n*** determined from 2-D spherulite growth monitored by *in situ* polarized optical microscopy.

Film thickness (nm)	**Growth rate ($\times 10^{-2}$ μm/s)**	**Avrami Exponent *n***
76	1.7 ± 0.3	2.1
113	2.4 ± 0.2	2.1
210	4 ± 1.4	2.2
260	4.7 ± 0.7	2.4
290	6.7 ± 0.3	—
310	6.2 ± 0.2	2.2
370	6.6 ± 0.2	2

To identify the nucleation mode, we heated crystalline films above their melting temperature to erase their thermal history and let the samples cool to room temperature and crystallize. After crystallization was complete, we repeated the experiment three times, and followed the crystallization process using polarized optical microscopy. By comparing the images for each melt/crystallization cycle, we found that the distribution of nucleation sites were the same for each cycle, indicating heterogeneous nucleation and 1-D crystallization (radial growth).

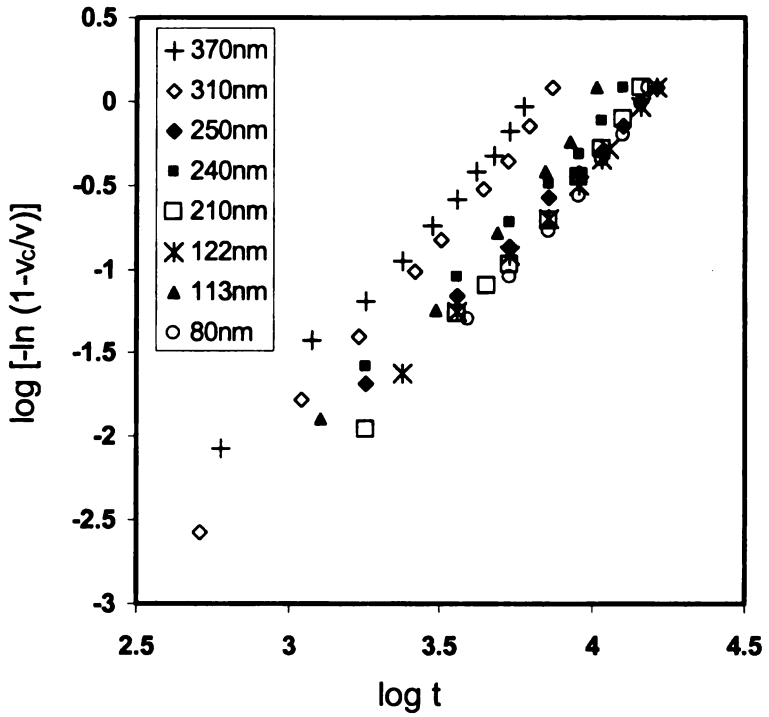

Figure 2.14. Linear fit of the Avrami equation to the experimental data for crystalline polymer brushes with different film thickness.

Frank *et al.* used Avrami analysis to interpret the dimensionality of crystal growth in poly(di-*n*-hexylsilane)[11] and PEO films.[2] For the poly(di-*n*-hexylsilane) film, polymer chains are oriented parallel to the surface, and high T_c and low film thickness favor one dimensional growth. For PEO films, the polymer chains were oriented perpendicular to the surface, and the crystal growth was 3-dimensional. The dimensionality of crystal growth is related to the polymer and interface interactions.

Several studies have reported the crystallization rates of PEO thin films.[2, 3, 14, 18] The results are dependent on the crystallization conditions (T_c, supercooling), the substrate, and the molecular weight of PEO. However, linear PEO is a poor model for the crystallization of polymer brushes because of the different architectures of linear and comb polymers as well as the processes involved in main-chain and side-chain crystallization. Therefore, we studied the crystallization behavior of spin-coated poly(PEGMA) thin films for comparison.

Poly(PEGMA) was prepared by ATRP of the PEGMA macromonomer in water using a CuBr/$CuBr_2$/bpy catalyst. After a 2 h polymerization at room temperature, the polymerization was exposed to air to terminate the reaction. Purification provided poly(PEGMA) as a white solid, with M_n = 60,000g/mol ^{1}H-NMR and IR spectra (see below) confirmed the chemical structure. Thin films were spin-coated onto gold coated silicon wafer substrate using CH_2Cl_2 as the solvent. After drying under vacuum and annealing at 30 °C, the samples were allowed to crystallize at room temperature.

Optical microscopy of the spin-coated film showed a spherulitic morphology with extinction of banded rings, which is possibly due to the twisting and dislocation of lamellae. Like the poly(PEGMA) brush, the orientation of the crystalline lamellae in

spin-coated films also depended on the film thickness. For a 60 nm thick film, the preferred lamellae orientation is parallel to the surface with the PEO side-chains oriented perpendicular to the surface. FT-IR data from the thick film (290 nm) is consistent with the PEO side-chains parallel to the surface, suggesting an perpendicular lamellae orientation.

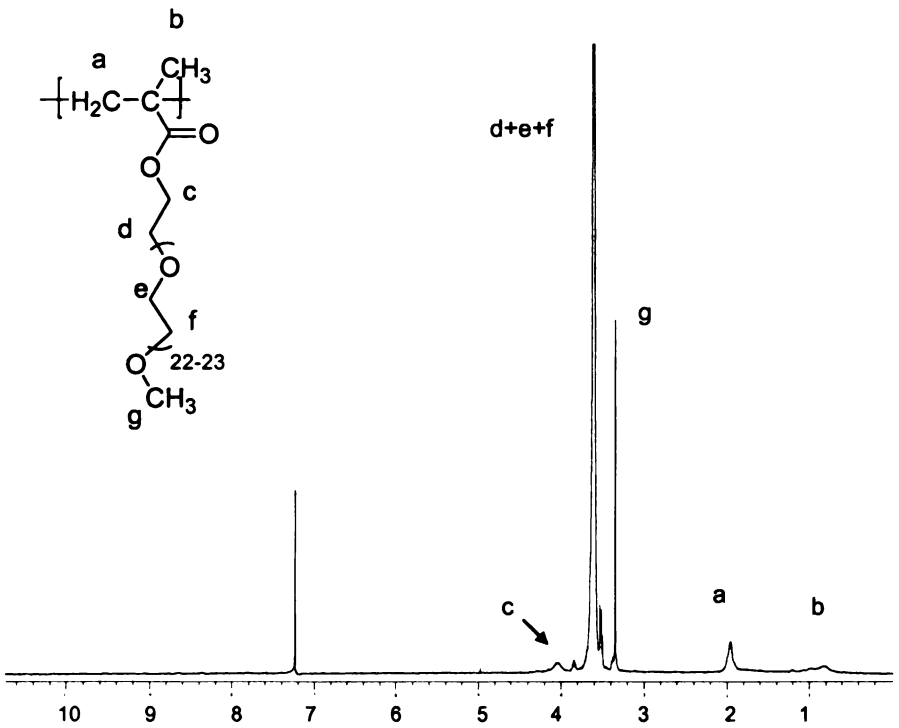

Figure 2.15. ^{1}H-NMR spectrum of poly(PEGMA).

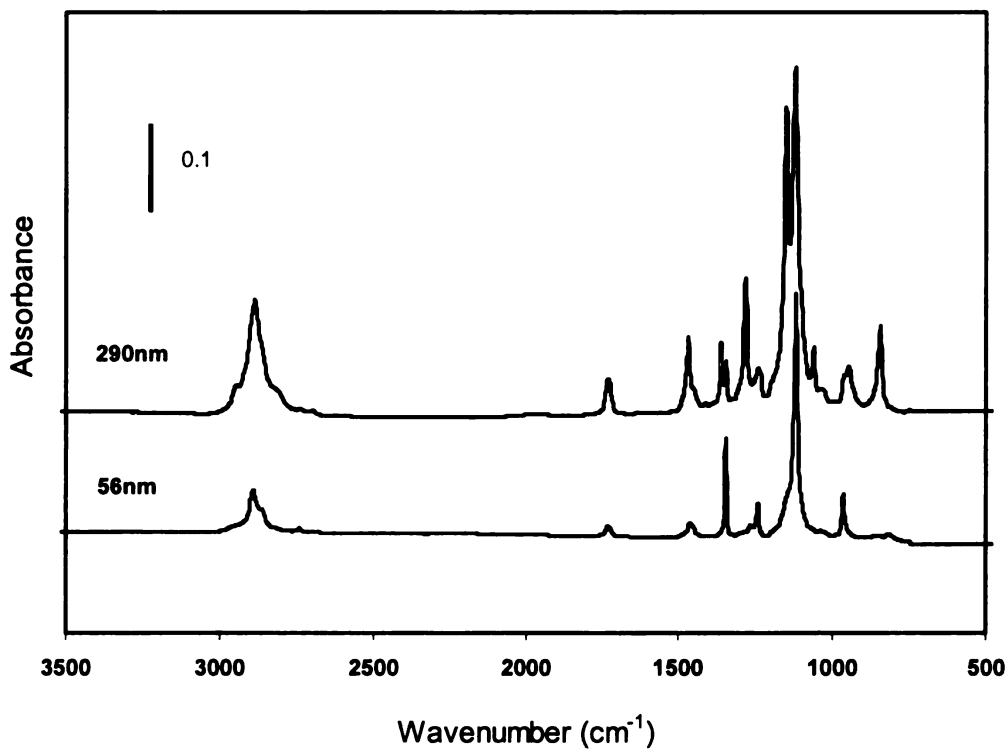

Figure 2.16. Reflectance FT-IR spectra of 56 and 290 nm thick poly(PEGMA) films that were spin-coated on the gold-coated silicon wafer.

The "spherulite" growth rate measured for a spin-coated 300 nm thick poly(PEGMA) film is shown in Figure 2.17. The spin-coated film crystallized twice as fast (0.12 μm/s) as a polymer brush (0.06 μm/s) of comparable thickness. The slower crystalline growth rate for polymer brushes indicates that the decreased mobility imposed by the brush architecture trumps any benefits of chain alignment. Alignment effects may prove to be important only when the density of polymer chains on the surface approaches full coverage.

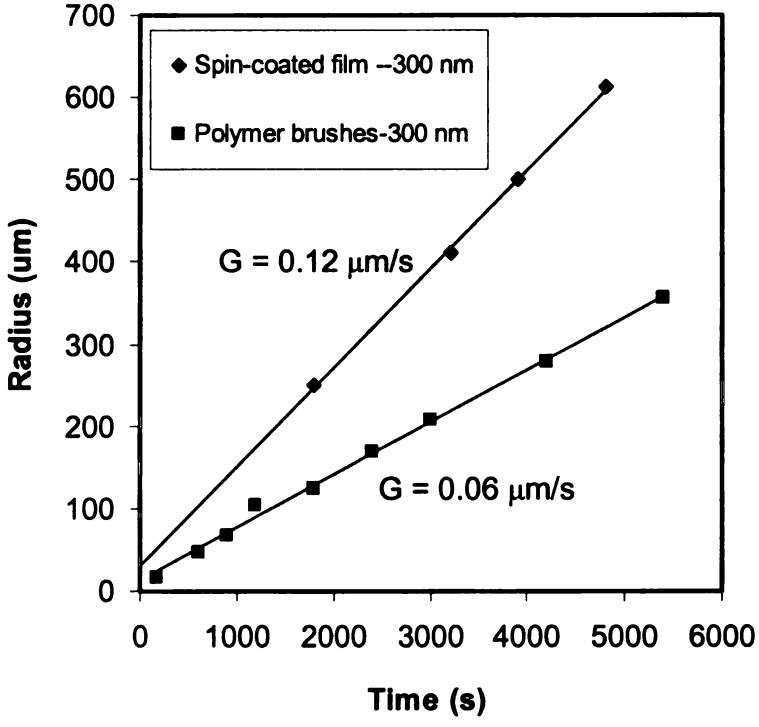

Figure 2.17. Crystal growth rates measured for spin-coated poly(PEGMA) and poly(PEGMA) brushes of comparable film thickness (~300 nm).

Conclusions.

Surface-initiated ATRP of PEGMA macromonomer from gold substrates lead to the nanometer-thck films of comb-like polymer brushes. Polymers with side chains of 22-23 ethylene oxide units align and crystallize. The film morphology, orientation of crystalline lamellae, and crystal growth rates all depend on the film thickness. Polarized optical microscopy and AFM show that the polymer brush films crystallized into spherulitic domains. In addition, both AFM and reflectance FT-IR spectroscopy are consistent with crystalline lamellae preferentially oriented perpendicular to the surface when the film thickness exceeds 100 nm. For thinner films, the favored orientation shifted to crystalline lamellae parallel to the surface, with the PEO side-chains oriented perpendicular to the surface. Crystal growth rates decreased with film thickness, and an Avrami analysis of the data indicated heterogeneous nucleation and one-dimensional crystal growth. Polymer brushes crystallized slower than physically absorbed films, likely due to mobility restrictions imposed by the brush architecture.

References:

1. Prucker, O.; Christian, S.; Bock, H.; Ruhe, J.; Frank, C. W.; Knoll, W., Glass transition in ultrathin polymer films. In *Organic Thin Films*, 1998; Vol. 695, pp 233-249.

2. Schonherr, H.; Frank, C. W., *Macromolecules* **2003,** *36*, 1188-1198.

3. Schonherr, H.; Frank, C. W., *Macromolecules* **2003,** *36*, 1199-1208.

4. Pearce, R.; Vancso, G. J., *Macromolecules* **1997,** *30*, 5843-5848.

5. Pearce, R.; Vancso, G. J., *Polymer* **1998,** *39*, 1237-1242.

6. Mellbring, O.; Oiseth, S. K.; Krozer, A.; Lausmaa, J.; Hjertberg, T., *Macromolecules,* **2001,** *34*, 7496-7503.

7. Wang, Y.; Ge, S.; Rafailovich, M.; Sokolov, J.; Zou, Y.; Ade, H.; Luning, J.; Lustiger, A.; Maron, G., *Macromolecules* **2004,** *37*, 3319-3327.

8. Sakai, Y.; Imai, M.; Kaji, K.; Tsuji, M., *Macromolecules* **1996,** *29*, 8830-8834.

9. Reiter, G.; Sommer, J. U., *J. Chem. Phys.* **2000,** *112*, 4376-4383.

10. Despotopoulou, M. M.; Frank, C. W.; Miller, R. D.; Rabolt, J. F., *Macromolecules* **1995,** *28*, 6687-6688.

11. Despotopoulou, M. M.; Frank, C. W.; Miller, R. D.; Rabolt, J. F., *Macromolecules* **1996,** *29*, 5797-5804.

12. Hu, Z. J.; Huang, H. Y.; Zhang, F. J.; Du, B. Y.; He, T. B., *Langmuir* **2004,** *20*, 3271-3277.

13. Mareau, V. H.; Prud'homme, R. E., *Macromolecules* **2005,** *38*, 398-408.

14. Dalnoki-Veress, K.; Forrest, J. A.; Massa, M. V.; Pratt, A.; Williams, A., *J. Polym. Sci. B: Polym. Phys.* **2001,** *39*, 2615-2621.

15. Schultz, J. M.; Miles, M. J., *J. Polym. Sci. B; Polym. Phys.* **1998,** *36*, 2311-2325.

16. Taguchi, K.; Miyaji, H.; Izumi, K.; Hoshino, A.; Miyamoto, Y.; Kokawa, R., *Polymer* **2001,** *42*, 7443-7447.

17. Marentette, J. M.; Brown, G. R., *Polymer* **1998,** *39*, 1405-1414.

18. Massa, M. V.; Dalnoki-Veress, K.; Forrest, J. A., *Eur. Phys. J. E* **2003,** *11*, 191-198.

19. Zdyrko, B.; Klep, V.; Luzinov, I., *Langmuir* **2003,** *19*, 10179-10187.

20. Zdyrko, B.; Varshney, S. K.; Luzinov, I., *Langmuir* **2004,** *20*, 6727-6735.

21. Neugebauer, D.; Theis, M.; Pakula, T.; Wegner, G.; Matyjaszewski, K., *Macronolecules* **2006,** *39*, 584-593.

22. Xu, J. T.; Ji, J., *Polymer* **2003,** *44*, 6379-6385.

23. Inomata, K.; Nakanishi, E.; Sakane, Y.; Koike, M.; Nose, T., *J. Polym. Sci. B: Polym. Phys.* **2005,** *43*, 79-86.

24. Yoshihara, T.; Murahashi, S.; Tadokoro, H., *J. Chem. Phys.* **1964,** *41*, 2902.

25. Miyazawa, T.; Ideguchi, Y.; Fukushima, K., *J. Chem. Phys.* **1962,** *37*, 2764-&.

26. Sun, X.; Zhang, H.; Zhang, L.; Wang, X.; Zhou, Q.-F., *Polym. J.* **2005,** *37*, 102-108.

27. Richardson, P. H.; Richards, R. W.; Blundell, D. J.; MacDonald, W. A.; Mills, P., *Polymer* **1995,** *36*, 3059-69.

28. Wang, M. T.; Braun, H. G.; Meyer, E., *Polymer* **2003,** *44*, 5015-5021.

29. Hoffmann, C. L.; Rabolt, J. F., *Macromolecules* **1996,** *29*, 2543-2547.

30. Bartczak, Z.; Argon, A. S.; Cohen, R. E.; Kowalewski, T., *Polymer* **1999,** *40*, 2367-2380.

31. Reiter, G.; Castelein, G.; Hoerner, P.; Riess, G.; Sommer, J. U.; Floudas, G., *Eur. Phys. J. E.* **2000,** *2*, 319-334.

32. Reiter, G.; Sommer, J. U., *Phys. Rev. Lett.* **1998,** *80*, 3771-3774.

33. Shah, R. R.; Merreceyes, D.; Husemann, M.; Rees, I.; Abbott, N. L.; Hawker, C. J.; Hedrick, J. L., *Macromolecules* **2000,** *33*, 597-605.

34. Takahash.Y; Sumita, I.; Tadokoro, H., *J. Polym. Sci. B; Polym. Phys.* **1973,** *11*, 2113-2122.

35. Gabriel, S.; Dubruel, P.; Schacht, E.; Jonas, A. M.; Gilbert, B.; Jerome, R.; Jerome, C., *Angew. Chem. Int. Ed.* **2005,** *44*, 5505-5509.

36. Avrami, M., *J. Chem. Phys.* **1939,** *7*, 1103.

37. Avrami, M., *J. Chem. Phys.* **1940,** *8*, 212.

38. Avrami, M., *J. Chem. Phys.* **1941,** *9*, 177.

39. Evans, U. R., *Trans. Faraday. Soc.* **1945,** *41*, 365.

40. Gedde, U., *Polymer Physics, 1st Edition*. Kluwer Academic Publishers: Dordrecht, 1995.

41. Wunderlich, B., *Macromolecular Physics*. Academic Press: New York, 1973, 1976; Vol. 1, 2.

Chapter III

Synthesis of Comb-like Polymer Brushes on Planar and Nanoparticulate Surfaces

This chapter describes the synthesis and characterization of comb-like polymer brushes on planar and non-planar surfaces using surface-initiated ATRP. Comb-like polymer brushes were formed on gold and silica surfaces by polymerization of PEGMA macromonomers in aqueous media. Polymerization of macromonomers is challenging because their high molecular weight results in low monomer concentrations. Studies of the kinetics of surface-initiated ATRP on planar substrates were used to identify optimum conditions for the growth of PEGMA films. In the second part of this chapter, these polymerizations were used to grow comb-like polymer brushes on the surface of silica nanoparticles.

Introduction

Poly(ethylene glycol) (PEG) coated surfaces are important in biological and medical applications due to PEG's ability to resist non-specific protein adsorption and cell adhesion.[1] A variety of chemical methods have been developed to deposit strongly adhering PEG coatings on surfaces including self-assembly of PEG-containing thiols on gold,[2] coupling reactive groups on PEG with silicon substrates,[3, 4] or the use of priming layers such as poly(glycidyl methacrylate) (PGMA). However, these "*grafting to*" methods usually result in a low PEG grafting density and thin films. Alternatively, PEG brushes can be grafted from initiators anchored on surfaces through the polymerization of

monomers that incorporate PEG segments. The advantage of using comb-like polymer brushes is that dense arrays of PEG side chains are formed in a one-step polymerization. A preference for well-defined brush structures implies their synthesis by a controlled polymerization technique such as ATRP. Zhu *et al.* [5] used ATRP to grow poly(PEGMA(4-5)) (the numbers refer to the average number of oxyethylene repeat units in the poly(ethylene glycol) methyl ether chain) from silica by ATRP and obtained films < 30 nm thick. Recently, Ma *et al.* [6] used ATRP to synthesize poly(PEGMA(8-9)) from a gold coated surface, however, the limiting film thickness was only 100 nm after a 16 h polymerization. Obviously, faster polymerizations of such monomers are needed to provide ready access to materials designed to exploit PEG-functionalized surfaces.

In the previous chapter, we described the polymerization of PEGMA from gold and studied the crystallization behavior of polymer brushes. In this chapter, we describe optimization of the polymerization conditions for the synthesis of polymer brushes from PEG-substituted methacrylates (Scheme 3.1), with an emphasis on generating thick films on surfaces using short polymerization times.

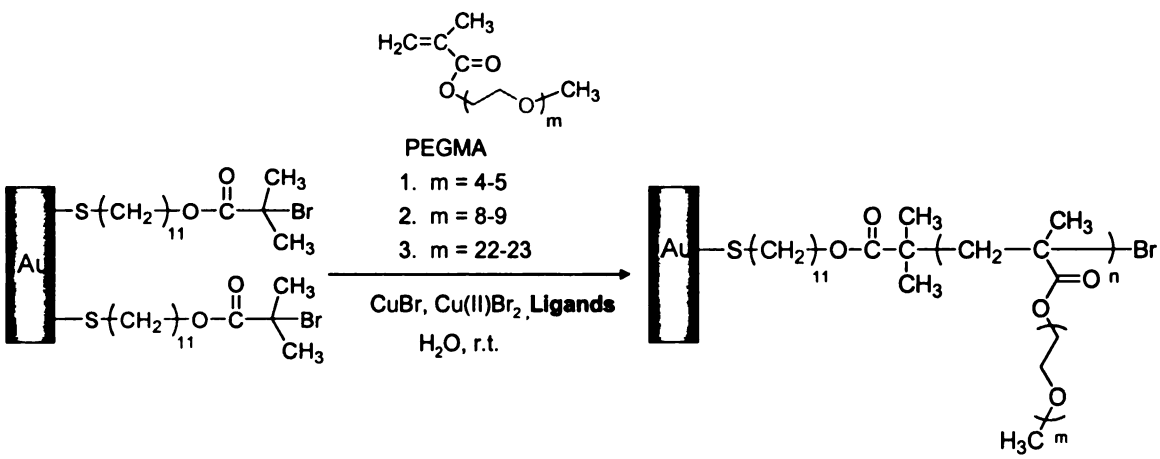

Scheme 3.1. Surface-initiated ATRP of PEGMA from gold surfaces.

Experimental

Materials. Unless otherwise noted, all chemicals were obtained from Aldrich. PEGMA(4-5), (M_n = 300 g/mol) and PEGMA(8-9), (M_n = 875 g/mol) were eluted through a basic alumina column to remove inhibitor. PEGMA(22-23) (M_n = 1,100 g/mol), $Cu^{I}Br$ (99.999%), $Cu^{I}Cl$ (99.999%), $Cu^{II}Br_2$ (99.999%), 1,1,4,7,10,10-hexamethyltriethyl enetetramine (HMTETA), tetramethyl-1,4,8,11-tetraazacyclotetradecane (Me_4Cyclam), 4,4'-di(*n*-nonyl)-2,2'-bipyridine (dnNbpy) 10-undecen-1-ol, 2-bromoisobutyryl bromide, pyridine, chlorodimethylsilane (97%) and H_2PtCl_6 were all used as received. Milli-Q water (18 MΩ) and *N,N*-dimethylformamide (DMF) (HPLC grade, inhibitor free) were used as polymerization solvents. Fumed silica (FS) (Aerosil A200), with a primary particle size approximately 12 nm and an average surface area of 200 m^2/g was kindly supplied by Degussa.

Characterization methods. Film thicknesses were measured by a rotating analyzer spectroscopy ellipsometer (M-44; J.A. Woollam) at a 75° angle of incidence. The refractive index and film thickness were calculated simultaneously from the values of Δ and Φ. Thermal gravimetric analyses (TGA) of fumed silicas were obtained in dry air using a Perkin Elmer TGA 7 instrument at a heating rate of 10 °C/min. Each sample was held at 110 °C for 30 min to remove adsorbed water prior to initiating the run. Differential scanning calorimetry (DSC) analyses of polymers were obtained using a Perkin Elmer DSC 7. Samples were run in sealed aluminum pans under an N_2 atmosphere. The coolant for the system was liquid nitrogen. Each sample was heated from room temperature to 120 °C at a rate of 10 °C/min, held at 120 °C for 30 min, cooled

to -90 °C at a rate of -50 °C /min, and then heated to 120 °C at a rate of 10 °C/min. The melting point was taken as the maximum of the melting endotherm.

Polymerization using the CuBr/CuBr$_2$/HMTETA catalyst complex. A catalyst solution was prepared in an oxygen-free drybox by adding CuBr (0.057 g, 20 mmol), $CuBr_2$ (0.045 g, 6 mmol) and HMTETA (0.13 g, 60 mmol) to 20 mL of DMF, and then transferred to a N_2-filled glove bag. A second Schlenk flask was loaded with PEGMA(4-5) (30 g, 0.09 mol) and H_2O (15 mL). The flask was connected to a vacuum line and the solution was degassed using three freeze-pump-thaw cycles, back-filled with N_2, and then transferred to the N_2-filled glove bag. Catalyst solution (5 mL) was added to the second flask, and the resulting blue-green solution was stirred until homogeneous. The final catalyst concentrations were [CuBr] = 2 mM, [$CuBr_2$] = 1 mM and [HMTETA] = 6 mM. The solution was added to a series of vials, each containing one initiator-anchored slide. Slides were removed from vials at predetermined times, ranging from 5 min to 1 h. (Polymerizations longer than 1 h generally became viscous with some gel formation.) The polymer films were rinsed sequentially with water, DMF, and anhydrous ethanol, and finally dried under a stream of N_2.

Polymerization using CuBr/Me$_4$Cyclam/CuBr$_2$(dnNbpy)$_2$ as the catalyst. In a drybox, $CuBr_2$ and dnNbpy (1:2 mol:mol) were mixed and the resulting green complex was stored for future use. A catalyst solution was prepared in an oxygen-free drybox by adding CuBr (0.057 g, 20 mmol), $CuBr_2(dnNbpy)_2$ (0.21 g, 10 mmol) and Me_4Cyclam (0.1 g, 20 mmol) to 10 mL of DMF. The solution was stirred until homogeneous (~ 20 min). A second Schlenk flask was loaded with PEGMA(4-5) (18 g, 0.05 mol) and H_2O (9 mL). The flask was connected to a vacuum line and the solution was degassed using three

freeze-pump-thaw cycles, and finally back-filled with N_2. In a N_2-filled glovebag, a portion of the catalyst solution (3 mL) was added into the flask. The final concentrations were [CuBr] = 2 mM, [$CuBr_2$ $(dnNbpy)_2$] = 1 mM, and [Me_4Cyclam] = 2 mM. The catalyst monomer solution solutions were combined, causing the formation of a brown solution and deposition of a precipitate. The solution was immediately transferred into the vials, each containing an initiator-anchored gold slide. The polymer films were taken out from the solution at predetermined times, ranging from 5 min to 1 h, rinsed sequentially with water, DMF, and anhydrous ethanol, and finally dried under a stream of N_2.

Synthesis of undecen-1-yl, 2-bromo-2-methyl propionate (1).[7] A 500 mL round bottom flask was loaded with 10-undecene-1-ol (42.78 g, 0.25 mol), anhydrous THF (250 mL), and 25 mL of pyridine. The flask was cooled to 0 °C, and 2-bromoisobutyryl bromide (24.8 mL) was added drop-wise to the flask. After stirring the reaction mixture at room temperature for 12 h, the solution was filtered to remove pyridinium hydrobromide, and THF was removed under reduced pressure. Hexane (100 mL) was added to the mixture, and the solution was washed with 2N HCl and water (2×). The organic phase was collected and dried over $MgSO_4$, filtered, and the solvent was removed by rotary evaporation. Purification by column chromatography on silica using 10/1 (v/v) hexane/ethyl acetate as the eluent provided **1** (R_f = 0.6) as a transparent liquid in 82.4% yield. ^{1}H-NMR: δ 1.2-1.45 (br, 12H), 1.64 (m, 2H), 1.94 (s, 6H), 2.05 (m, 2H), 4.17 (t, 2H), 4.95 (d, 2H), 5.8 (m,1H) ppm. ^{13}C-NMR: δ 171.6 (C=O), 139.1 (CH), 114.1 (CH_2), 66.2 (OCH_2), 56.01 (C), 32.97 (SCH_2), 30.81 (CH_3), 29.4 (CH_2), 29.3 (CH_2), 29.24 (CH_2) 29.18 (CH_2), 28.4 (CH_2), 25.8 (CH_2).

Synthesis of (11-(2-bromo-2-methyl)propionyloxy)undecyldimethylchlorosilane (2). H_2PtCl_6 (5 mg) and undecen-1-yl, 2-bromo-2-methyl propionate **(1)** (3.00 g, 9.43 mmol) were added to a dry flask. Chlorodimethylsilane (10.43 mL, 94.3 mmol) was syringed into the mixture and the reaction mixture was stirred at room temperature under N_2. The reaction was monitored by ^{1}H-NMR, and after the reaction was complete, the yellowish solution was diluted with anhydrous toluene, and quickly passed through a column of activated carbon and silica. Removal of the solvent provided (11-(2-bromo-2-methyl)propionyloxy)undecyldimethylchlorosilane (**2**) as a colorless liquid in 60% yield. ^{1}H-NMR: δ 0.4 (s, 6H), 0.9 (t, 2H) 1.22-1.42 (br, 16H), 1.8 (m, 2H), 1.93 (s, 6H), 4.16 (t, 2H). ^{13}C-NMR: δ 171.7 (C=O), 66.2 (OCH_2), 56.01 (C), 32.97 (SCH_2), 30.81 (CH_3), 29.4 (CH_2), 29.3 (CH_2), 29.24 (CH_2), 29.18 (CH_2), 28.4 (CH_2), 25.8 (CH_2), 22.1 (CH_2), 19.0 (CH_2), 1.69 (CH_3).

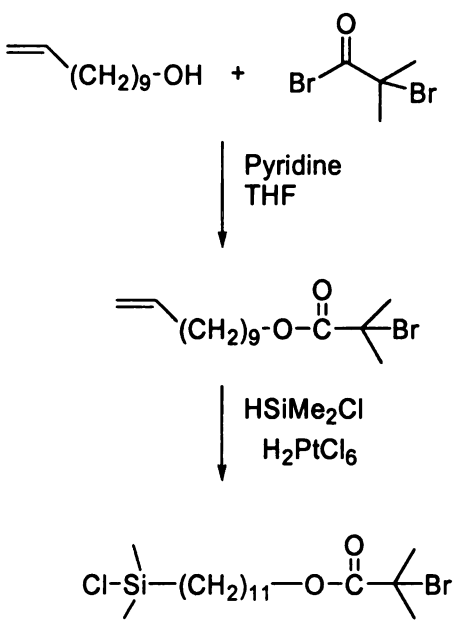

Scheme 3.2. Synthetic route to (11-(2-bromo-2-methyl)propionyloxy) undecyldimethylchlorosilane.

Surface-initiated ATRP of PRGMA from Si wafers. Silicon (100) wafers were cleaned in a toluene ultrasound bath for 5 min. The wafers were then rinsed with toluene, acetone and anhydrous ethanol, and dried with a stream of N_2. The samples were oxidized in a UV/ozone chamber for 15 min. The thickness of the SiO_2 layer measured by ellipsometry was 16-22 Å. The growth of initiators was done in a drybox or glove bag purged with N_2. To attach the initiator to the surface, the silica wafers were immersed in an initiator/toluene solution for 24 h. The film was washed with a large amount of toluene and ethanol, and dried under a stream of N_2. The increase in film thickness measured by ellipsometry, 16 ± 2Å, confirmed the presence of the initiator.

A typical polymerization procedure is described. A Schlenk flask was loaded with PEGMA(4-5) (42 g) and MilliQ water (21 mL). The solution was degassed by three freeze-pump-thaw cycles, and finally filled with argon. Cu(I)Br (0.018 g), Cu(II)Br_2 (0.008 g), and bpy (0.06 g) were added to the solution under argon. The mixture was stirred until a homogeneous dark brown solution formed (at least 1 h). The final catalyst concentrations were [CuBr] = 2 mM, [$CuBr_2$] = 0.6 mM, and [bpy] = 6 mM. The solution was transferred into a glove bag and added to a series of vials, each containing one initiator-anchored gold slide. Slides were removed from vials at predetermined times. Polymer films grown from silica wafers were rinsed with a large amount of water, followed by sonication in toluene, washed with ethanol, and finally dried under a stream of N_2.

Grafting of polymer brushes on the surface of fumed silica. Fumed silica was placed under vacuum at 120 °C for 12 h to remove adsorbed moisture. Fumed silica (0.5 g) was added to a Schlenk flask and the flask was placed under vacuum and back-filled

with N_2. Initiator (5 μL) and anhydrous toluene (10 mL) was syringed into the flask under N_2, and the reaction mixture was stirred for 24 h. After the reaction was complete, the mixture was filtered through a 40 μm pore-size filter under reduced pressure. The fumed silica was exhaustively washed with toluene under Soxhlet conditions, and dried under vacuum to yield ~2 g of white particles. TGA analysis and IR spectra (Figure 3.11.) confirm attachment of the initiator (C=O peak at 1725 cm^{-1}).

For the polymerization of PEGMA from the silica particles, fumed silica (with initiator attached) was added to a Schlenk flask, evacuated, and back-filled with argon. Degassed solvent (H_2O or H_2O/MeOH) and the monomer mixture was added and the solution was stirred to ensure complete dispersion of the silica in the solution. The catalyst solution (CuBr/$CuBr_2$/bpy complex) was added to the monomer solution to start the polymerization. After 2 h, polymerization was terminated by exposure of solution to the air. Water was added to the mixture, causing the solution to turn blue. The solution was sonicated for 2 min, and then the solids were collected by centrifugation. After decanting the solvent, an aqueous solution of saturated ethylenediaminetetraacetic acid (EDTA) was added to the mixture followed by sonication and centrifugation. After repeating this procedure three times, the solution was colorless. The solvent was decanted, and the remaining solvent was removed under vacuum. The poly(PEGMA)-modified silica was isolated as a white powder. The same procedure applied to PEGMA(8-9) yielded a white, slightly sticky solid.

Control experiments. A200 fumed silica was added to a Schlenk flask, and then evacuated and backfilled with Ar to establish an inert atmosphere. A degassed mixture of monomer and solvent (H_2O or H_2O/MeOH) was added to the silica and stirred to disperse

the silica. Then a mixture of $CuBr/CuBr_2$/bpy dissolved in an aqueous solution of monomer (see Table 3.1) was added to the solution and stirring was continued for 2 h. The work-up was started by adding water to the mixture, causing the solution to turn blue. After sonication for 2 min, the solids were isolated by centrifugation. The solvent was decanted and saturated aqueous EDTA was added to the mixture followed by sonication and centrifugation. The resulting colorless solution was decanted and the residual solvent was removed under vacuum. The powdery white solid was subjected to TGA analysis. The procedure for the other control experiment was similar, except the silica used had an attached initiator layer, and no $CuBr_2$ was added to the catalyst mixture.

Results and Discussion

Surface-initiated ATRP of PEGMA on Au. In surface-initiated ATRP, the absolute amount of initiator on the surface is small, and thus the concentration of $Cu^{II}Br$ due to the reaction of catalyst with initiator is negligible. Once radicals are generated on the surface, they cannot easily be converted to their dormant state, which leads to termination through bimolecular radical coupling and disproportionation. Thus, the addition of $Cu^{II}Br$ at the beginning of the reaction is necessary for controlled polymerizations from surfaces. Mixed halide systems ($CuBr_2/CuCl$) were reported to effectively slow the polymerization rate and reduce termination by maintaining a lower concentration of growing radicals.[8] Therefore, our initial experiments on the surface-initiated ATRP of PEGMA used a $CuCl/CuBr_2$/bpy catalyst system. The mixed halide system provided good control over polymerization as expected, but the polymerization rate, ~2 nm/h and 80 nm after 48 h, was too slow (Figure 3.1). The likely reasons for the low polymerization rate were a low K_{eq} ($k_{act} << k_{deact}$), the intrinsic low concentration of polymerizable groups in the

macromonomer, and possible rate reductions due to reduced access of the macromonomer to the growing chains on the surface. Switching from CuCl to CuBr, a more reactive catalyst, provided faster growth rates at the same catalyst concentration (Figure 3.1), however, the limiting film thickness was < 100 nm and curvature in the film thickness-time relationship indicates significant termination. Similar results were obtained for the polymerization of PEGMA(8-9) catalyzed by CuBr and CuCl. Again, we found that mixed halide system provided good polymerization control, but thin films. As shown in Figure 3.2, the difference between the two catalyst systems is dramatic.

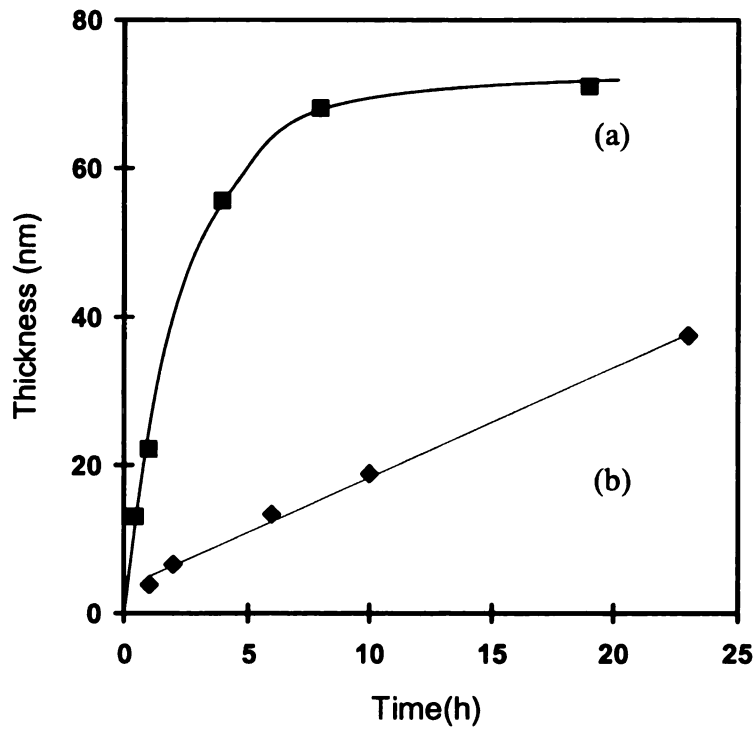

Figure 3.1. Evolution of the ellipsometric film thickness with time for the growth of poly(PEGMA(22-23)) from Au. Conditions: [M]:[H_2O] = 3:2 (v/v). (a) [CuBr] =10 mM, [$CuBr_2$] = 5 mM, [bpy]= 30 mM. (b) [CuCl] = 10 mM, [$CuBr_2$] = 5 mM, [bpy] = 30 mM. The curves are guides to the eye.

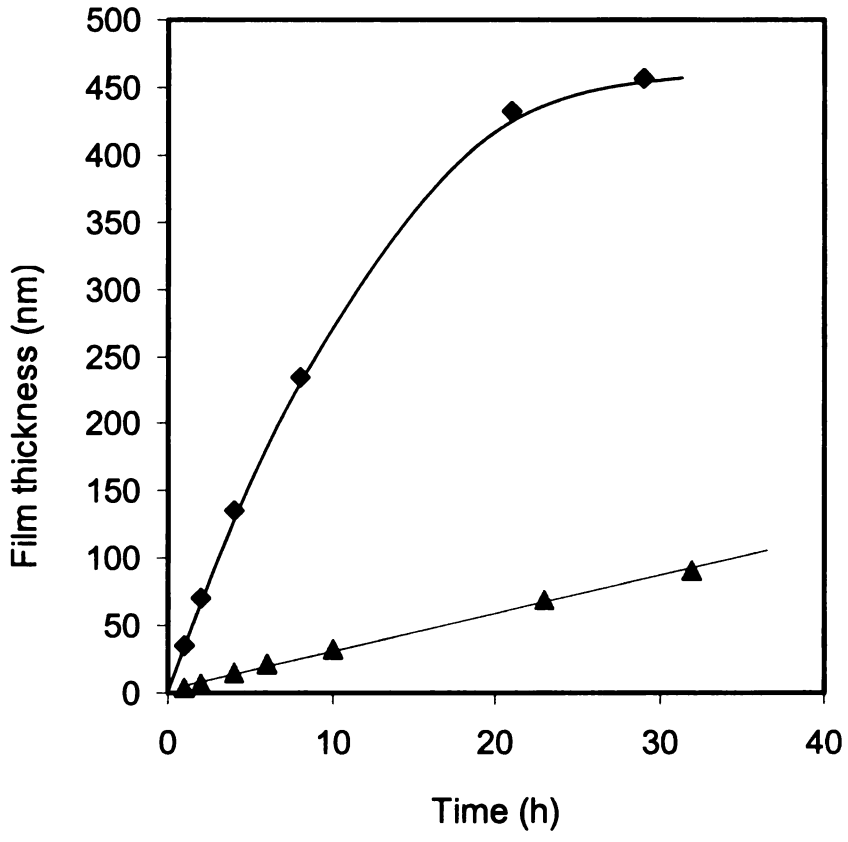

Figure 3.2. Evolution of the ellipsometric film thickness with time for the growth of poly(PEGMA(8-9)) from Au. Conditions: (a) [CuBr] = 28.5 mM, [$CuBr_2$] = 9.6 mM, [bpy] = 85.5 mM; (b) [CuCl] = 28.5 mM, [$CuBr_2$] = 9.6 mM, [bpy] = 85.5 mM. The curves are guides to the eye.

Previous results from Kim *et al.* showed that high catalyst concentrations led to a spatially dense concentration of surface-bound radicals that easily combine. Thus, the radical concentration is not constant and polymer film growth fails to follow first order kinetics in monomer. Reducing the catalyst concentration can increase the film growth rate and provide improved control over the polymerization. Figure 3.3 shows the effects of catalyst concentration on the film growth rate and film thickness in the ATRP of PEGMA(22-23). The early stages of the polymerizations are similar, but the highest growth rate and highest limiting film thickness (400 nm) correspond to the lowest catalyst concentration. Near-linear growth occurred during the initial 8 h of polymerization, and deviation from linear growth at later stages suggests some termination. Polymerizations using high catalyst concentrations were plagued by significant termination and ceased after 5 h, yielding a maximum film thickness of ~50 nm.

Applying the same approach used for the polymerization of PEGMA(8-9) gave qualitatively similar results (Figure 3.4). Two catalyst concentrations were tested, [CuBr] = 28.5 mM, and [CuBr] = 3 mM. Again the higher catalyst concentration provided the thinner film. Interestingly, the film grown with [CuBr] = 3 mM is roughly comparable to data set b in Figure 3.3, but the film derived from the lower molecular weight monomer was significantly thicker. Increasing the monomer concentration leads to thicker films (Figure 3.5.) as expected. Compared to the case of small monomers, a higher monomer concentration may help overcome the slow diffusion of the macromonomers to the reactive surface sites.

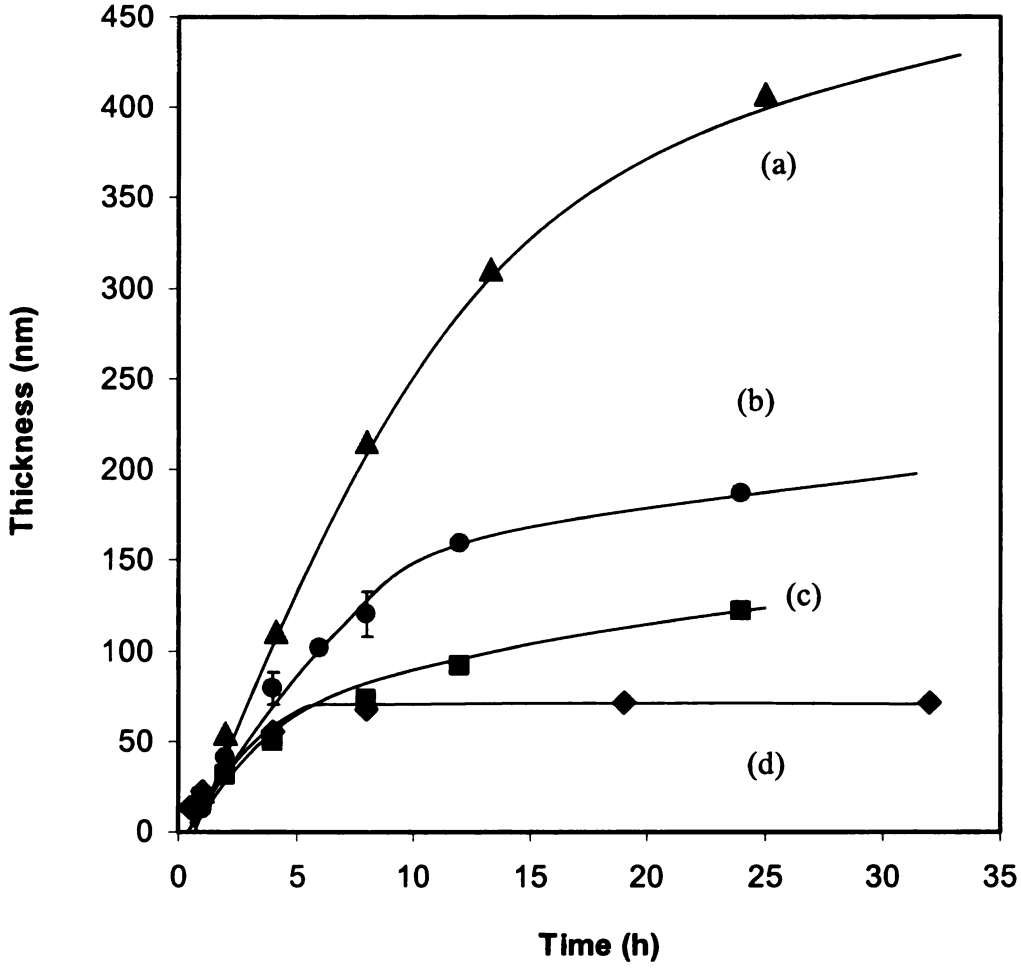

Figure 3.3. Evolution of the ellipsometric film thickness with time for the growth of poly(PEGMA(22-23)) films from Au. [M]:[H_2O] = 3:2 (v/v). (a) [CuBr] = 0.7 mM, [$CuBr_2$] = 0.21 mM, [bpy] = 2.1 mM; (b) [CuBr] = 2 mM, [$CuBr_2$] = 0.6 mM, [bpy] = 6 mM; (c) [CuBr] = 5 mM, [$CuBr_2$] = 1.5 mM, [bpy] = 15 mM; (d) [CuBr] = 10 mM, [$CuBr_2$] = 3 mM, [bpy] = 30 mM.

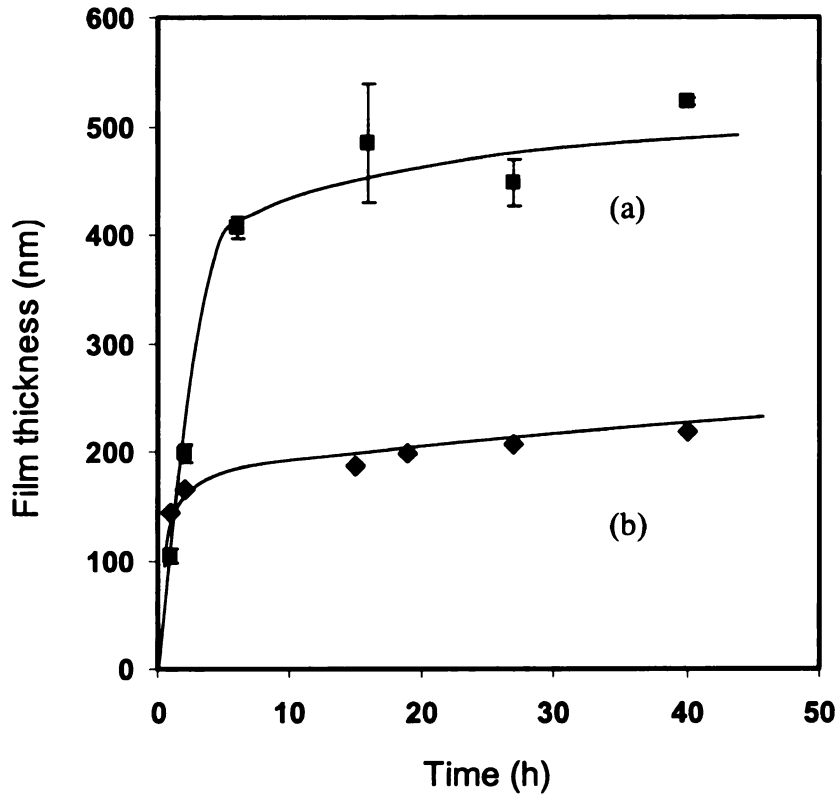

Figure 3.4. Evolution of the ellipsometric film thickness as a function of time for the polymerization of poly(PEGMA(8-9)). [M]:[[H_2O] = 1:1. (a) [CuBr] = 28.5 mM, [$CuBr_2$] = 9.6 mM, [bpy] = 85.5 mM. (b) [CuBr] = 3 mM, [$CuBr_2$] = 1 mM, [bpy] = 9 mM. The curves are guides to the eye.

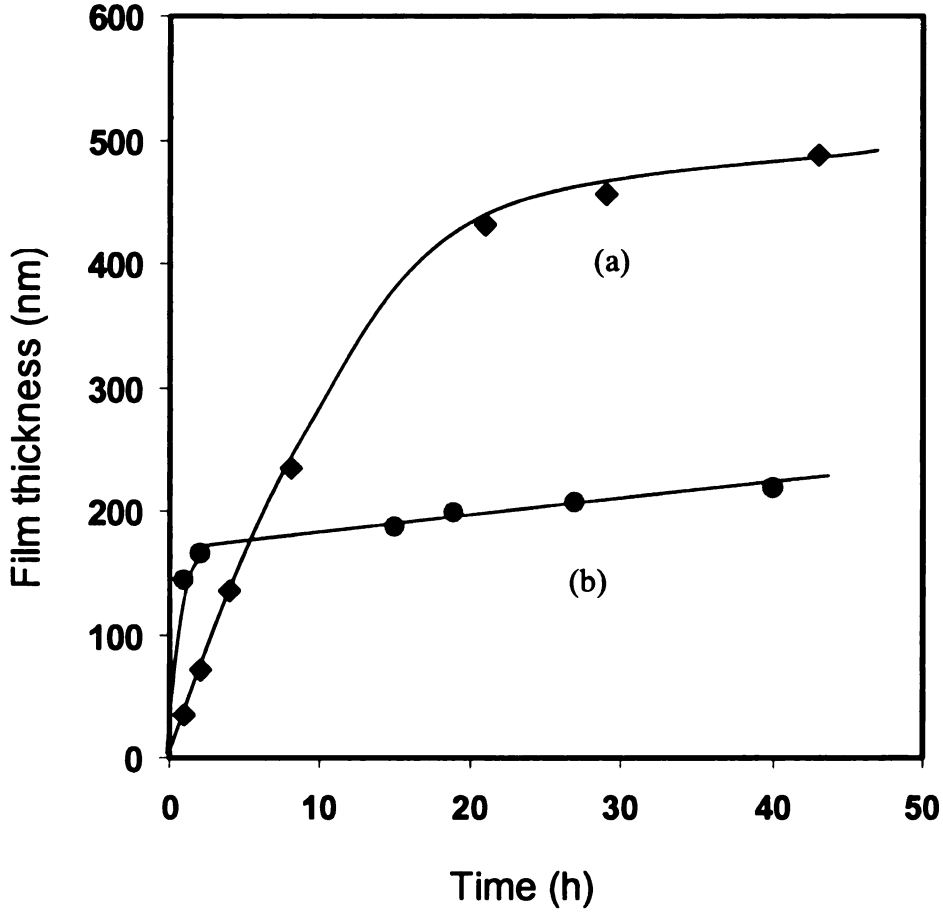

Figure 3.5. Evolution of the ellipsometric film thickness with time for the polymerization of PEGMA(8-9) at different monomer concentrations. Conditions: [CuBr] = 28.5 mM, [$CuBr_2$] = 9.6 mM, [bpy] = 85.5 mM. (a) [M]:[H_2O] = 2:1 and (b) [M]:[H_2O]=1:1. The curves are guides to the eye.

Rapid growth of comb-like polymer brushes on the surface. As described earlier, our motivation for optimizing the growth conditions for poly(PEGMA) brushes is the potential utility of thick brushes as membranes, electrolytes and in other applications. Because of the large surface area required in gas separations, processes that take hours to deposit films are not economically viable. There are alternatives to surface initiated ATRP, such as plasma polymerization or UV-induced graft polymerization, for generating polymer films on membranes. However, plasma polymerization is incompatible with non-volatile monomers, both methods can lead to polymer degradation, and neither affords significant control. As shown earlier, controlled growth of 100 nm films via ATRP can takes several hours, but practical syntheses require controlled growth with rates >100 nm/h. Our goal is the synthesis of polymer membranes in minutes using surface-initiated polymerization. Dense films are preferable since they may enhance membrane selectivity.

Our earlier results suggest that a more rapid polymerization system requires a low concentration of a highly active catalyst in a concentrated monomer solution. Copper based ATRP catalysts with tetradentate ligands such as HMTETA are more reactive than catalysts with bpy and other bidentate ligands.[9] Recently, Bao *et al.* reported the ultrafast ATRP of *tert*-butyl acrylate (20 nm/min) from Au and silica surfaces using a $CuBr/Me_4Cyclam/CuBr_2/(dnNbpy)_2$ catalyst in DMF/anisole. The same catalyst system might also be useful for the polymerization of PEGMA. Since the $CuBr/Me_4Cyclam/CuBr_2/(dnNbpy)_2$ catalyst is sparingly soluble in water, we used DMF as a co-solvent. Despite the formation of a precipitate when a DMF solution of the catalyst was added to the monomer/water mixture, the PEGMA polymerization rate was

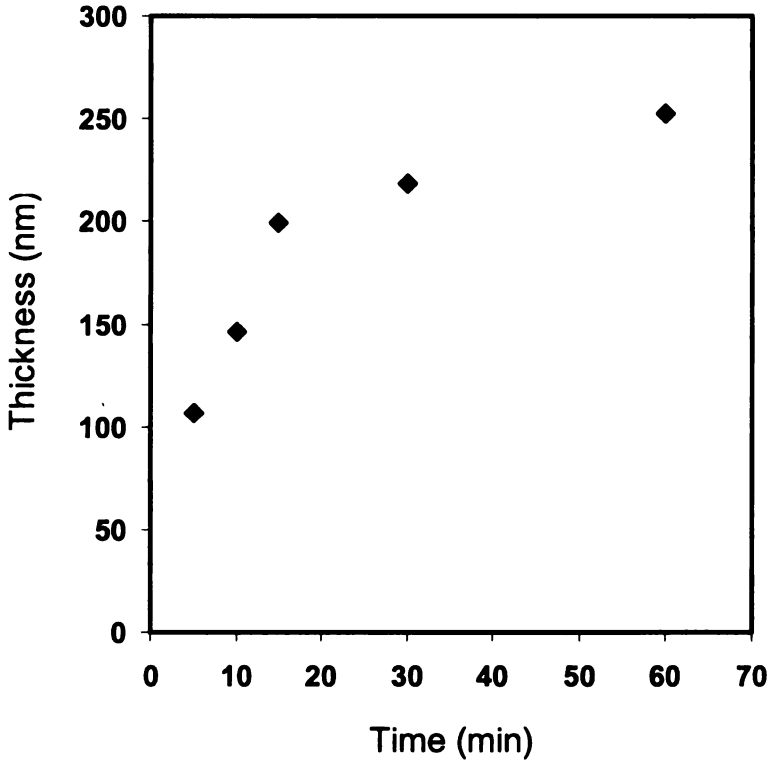

Figure 3.6. Evolution of the ellipsometric film thickness with time for the polymerization of PEGMA(4-5) using Me_4Cyclam as the ligand. Conditions: [M]:[H_2O+DMF] = 1:1; [CuBr] = 2 mM, [$CuBr_2$/(dnNbpy)$_2$] = 0.6 mM, [Me_4Cyclam] = 6 mM.

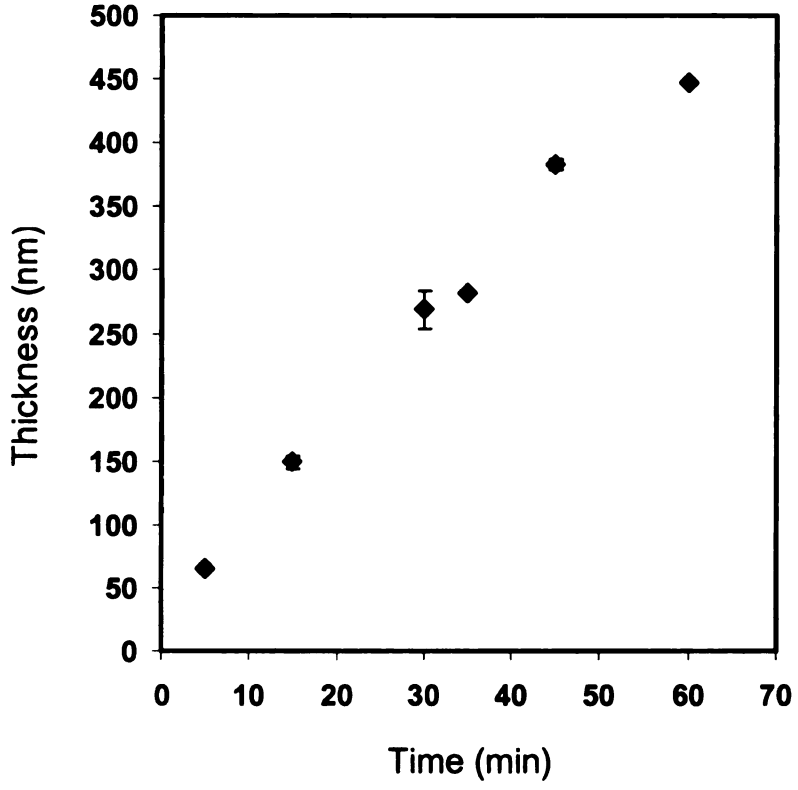

Figure 3.7. Evolution of the ellipsometric film thickness with time for the polymerization of PEGMA(4-5) using HMTETA as the ligand. Conditions: [M]/[H_2O+DMF] = 1:1, [CuBr] = 2 mM, [$CuBr_2$] = 0.6 mM, [HMTETA] = 6 mM. The data points are the average of two independent polymerizations.

very fast, with 100 nm thick films formed in 5 min (Figure 3.6). Using a related ligand, HMTETA, a 5 min polymerization of PEGMA(4-5) using water as a solvent yielded a 60 nm thick film. Remarkably, the linear growth in film thickness with time implies that the polymerization is well-controlled.

Figure 3.8. compares PEGMA polymerizations using the HMTETA and Me_4Cyclam ligands. Both systems rapidly polymerize PEGMA(4-5) (~10 nm/min), however, each system has limitations. Polymerizations using Me_4Cyclam were much less controlled, and the rate of polymerization visibly decreased after 15 min. Polymerization using HMTETA became viscous after 1 h polymerization, which suggests substantial chain transfer. Significant chain transfer has been observed in free-radical[10] and photoiniferter mediated[11] polymerization of PEGMA. The coefficient for chain transfer to PEG [12] is an order of magnitude higher than MMA (1.2×10^{-5}),[13] and is believed to be dominated by of hydrogen abstraction from the ethylene glycol units. Although increases in solution viscosity, and presumably chain transfer, were occasionally seen in the CuBr/bpy system, it is unclear why chain transfer is favored for the HMTETA catalyst. A complication of the Me_4Cyclam system is the marginal solubility of the catalyst. The reaction solution is inhomogeneous and a portion of the CuBr catalyst complex precipitates. When pure DMF is used as the solvent, the HMTETA system fails to generate thick films. Another problem of heterogeneous polymerization is that they provide less uniform films.

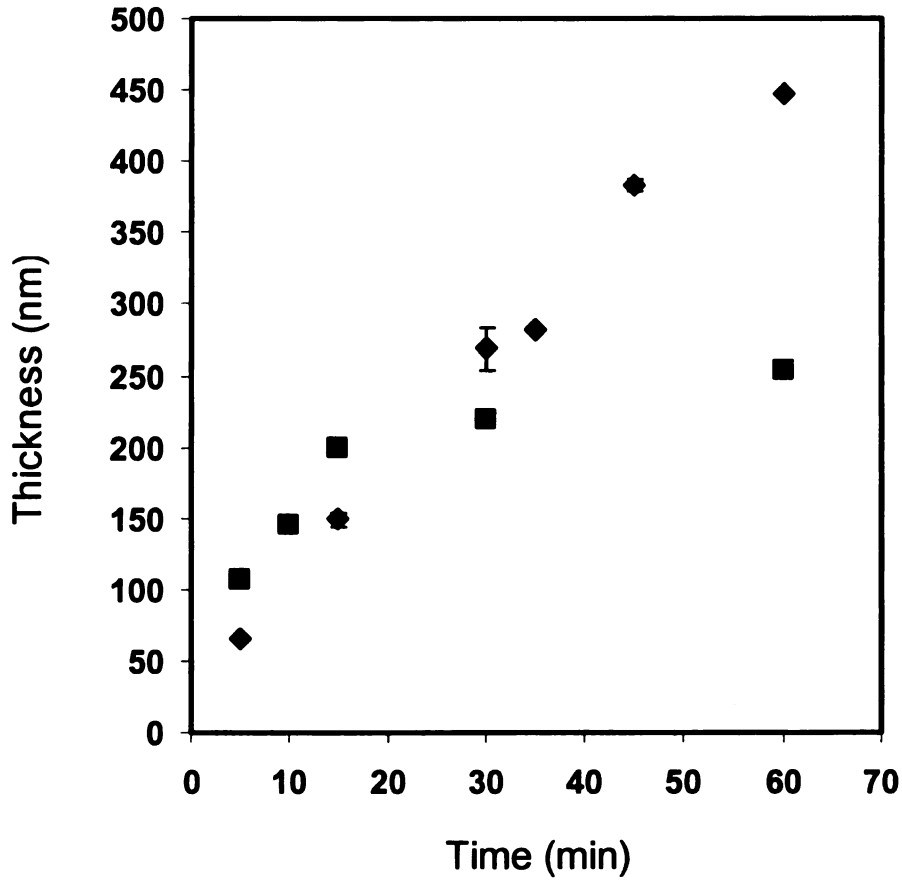

Figure 3.8. Evolution of the ellipsometric film thickness with time for the polymerization of PEGMA(4-5) using HMTETA(♦) and Me_4Cyclam (■) as ligands. The data are re-plotted from Figures 3.6 and 3.7.

Synthesis of PEG-functionalized nanoparticles. Particles with PEO-modified surfaces have applications ranging from stationary phases for chromatographic separations to polymer electrolytes in lithium ion batteries.[14] Initially, comb-like polymer brushes were grown on the surface of silicon wafers since this substrate facilitates film characterization by ellipsometry. Later, PEG-functionalized nanoparticles were prepared by the polymerization of PEGMA from the surface of fumed silica in aqueous media at room temperature.

Growth of polymer brushes on silica wafers. Scheme 3.3 shows the synthetic steps used to grow polymer brushes from silicon wafer surfaces. Traditionally, people use trichlorosilanes to anchor initiators and other organic species on SiO_2 surfaces, but polymerization of trichlorosilanes competes with surface anchoring, complicating quantification of the anchoring step. Therefore, initiators were attached to silicon wafers and silica nanoparticles as monochlorosilanes. To generate initiator layers on SiO_2, clean silicon wafers were placed in an initiator/toluene solution for 24 h. Ellipsometric measurements showed an increase in film thickness (20 ± 3Å) confirming successful attachment of the initiator. Et_3N was occasionally used to accelerate the initiator anchoring reaction.

Surface-initiated ATRP was catalyzed by a mixture of $CuBr/CuBr_2$/bpy in aqueous media at room temperature. Figure 3.9 shows the polymerization of PEGMA(4-5). Thick films (>300 nm) were obtained in 8 h by using a relatively low catalyst concentration ([CuBr] = 2 mM, $[CuBr_2]$ = 0.6 mM, [bpy] = 6 mM). The film thickness-time relationship is linear, indicating a controlled polymerization, and a lower catalyst concentration yielded thinner films. Both are consistent with minimal termination.

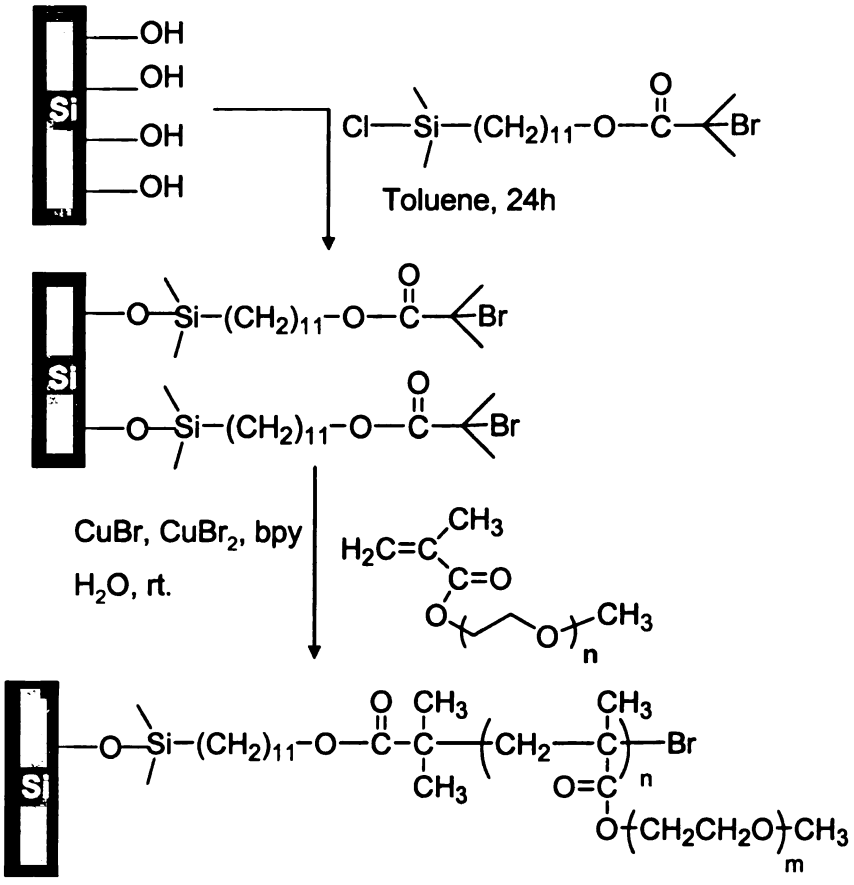

Scheme 3.3. Growth of comb-like PEO polymer brushes from SiO_2 surfaces.

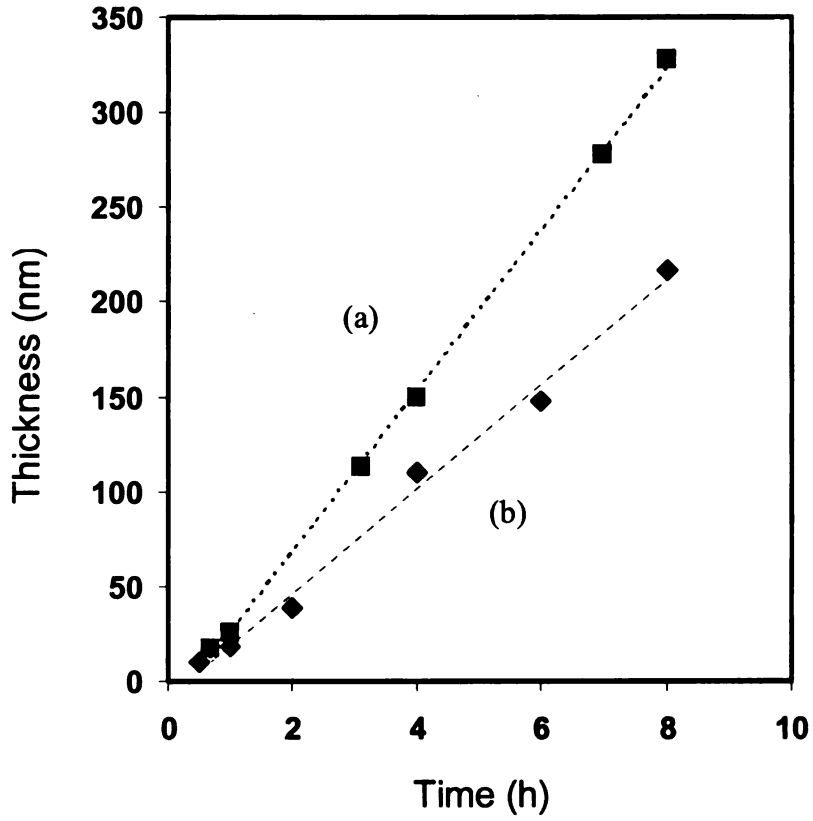

Figure 3.9. Evolution of the ellipsometric film thickness with time for the polymerization of PEGMA(4-5). Conditions: [M]:[H_2O] = 2:1, (a) [CuBr] = 2 mM, [$CuBr_2$] = 0.6 mM, [bpy] = 6 mM; (b) [CuBr] = 1 mM, [$CuBr_2$] = 0.3 mM, [bpy] =3mM.

Synthesis of comb-like polymers on the surface of fumed silica. Growth of PEGMA from nanoparticles (Scheme 3.4) follows the same procedure used for flat SiO_2 surfaces. Activated fumed silica particles were dispersed in a toluene solution of initiator and the reaction mixture was stirred for 24 h. White particles were isolated after filtration, exhaustive Soxhlet extraction, and drying under vacuum. Initiator attachment to fumed silica was confirmed from the C-H stretching (2900 cm^{-1}) and C=O stretching (1725 cm^{-1}) bands in the transmission IR spectrum (Figure 3.4). Considering the 8-9 wt% loss seen in TGA analyses (Figure 3.5), the surface area of A200 (200 m^2/g), and the areal density of silanols on SiO_2 surfaces (1 mmol OH/g), we estimate that ~¼ of the OH groups on the surface reacted with the monochlorosilane initiators.

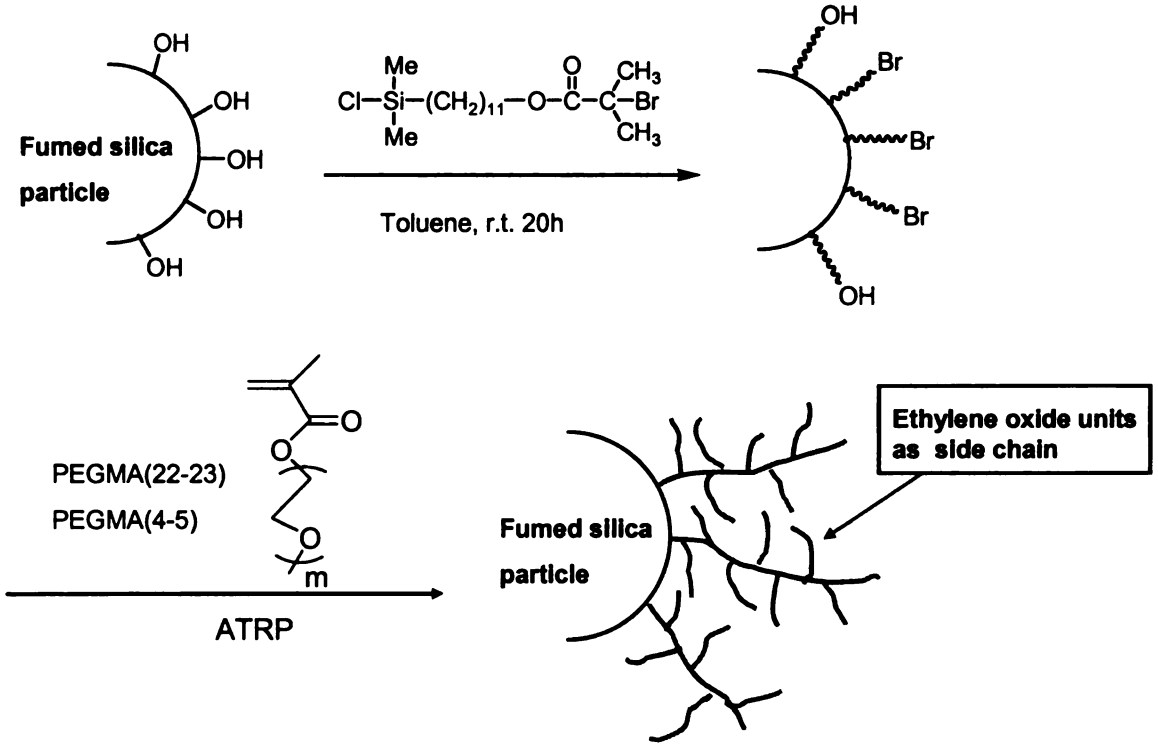

Scheme 3.4. Modification of silica particles by surface-initiated ATRP of PEG-methacrylates

PEGMA(4-5) and PEGMA(22-23) were used as macromonomers for polymerization. Fumed silica with surface anchored initiators was dispersed in a PEGMA/water solution, degassed, and filled with Ar. The catalyst mixture (CuBr, $CuBr_2$, and bpy) was then added to initiate the polymerization. The macromonomer and catalyst concentrations used in the polymerizations are listed in Table 3.1. After 2 h, the polymerization was terminated by exposure to air. The particles were purified, dried, and characterized as before. As shown in Figure 3.11, IR spectra show a large increase in the C=O stretching and CH_2 wagging bands. However, the C-O-C stretching bands of the oxyethylene units overlapped with a strong Si-O-Si peak and were not observed.

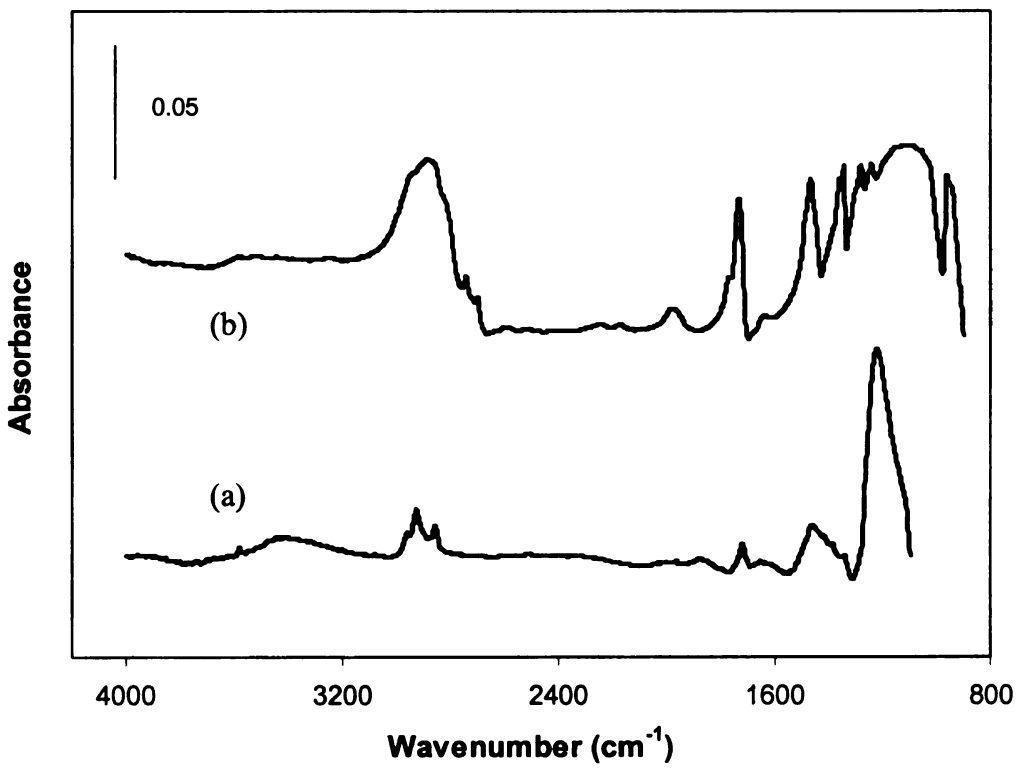

Figure 3.10. FT-IR spectra of (a) initiator anchored fumed silica particles; (b) poly(PEGMA(22-23)) grown from fumed silica particles.

Table 3.1. Reaction conditions for the polymerization of PEGMA(22-23) and PEGMA(4-5) from the surface of fumed silica particles.

Entry	Monomers	[M]	[M]:[I]:[CuBr]:[$CuBr_2$]:[Bpy]	Time (h)
1	PEGMA(22-23)	0.5	300 : 1 : 1.1 : 0.34 : 3.3	2
2	PEGMA(4-5)	0.5	167 :1 : 0.75 : 0.25 :2.5	1.5
3	PEGMA(4-5)	0.8	500: 1: 1.1 : 0.34 :3.3	0.5

TGA analysis indicated an 80% weight loss, as shown in Figure 3.6. To prove that the polymer films are covalently attached to the fumed silica surfaces, two control experiments were performed. First, fumed silica, the macromonomer, and catalyst solutions were mixed under the same condition used for ATRP. After isolating the silica using the washing and drying protocol described earlier, the particles were analyzed by TGA. The weight loss was ~5% (Table 3.2). In the second control experiment, initiator-anchored fumed silica was combined with a monomer/water solution containing $CuBr_2$, but no CuBr catalyst. After stirring for 2 h, the particles were isolated and analyzed by TGA. The 8% weight loss supports covalent anchoring of poly(PEGMA) to the surface, rather than simple physisorption of the macromonomer.

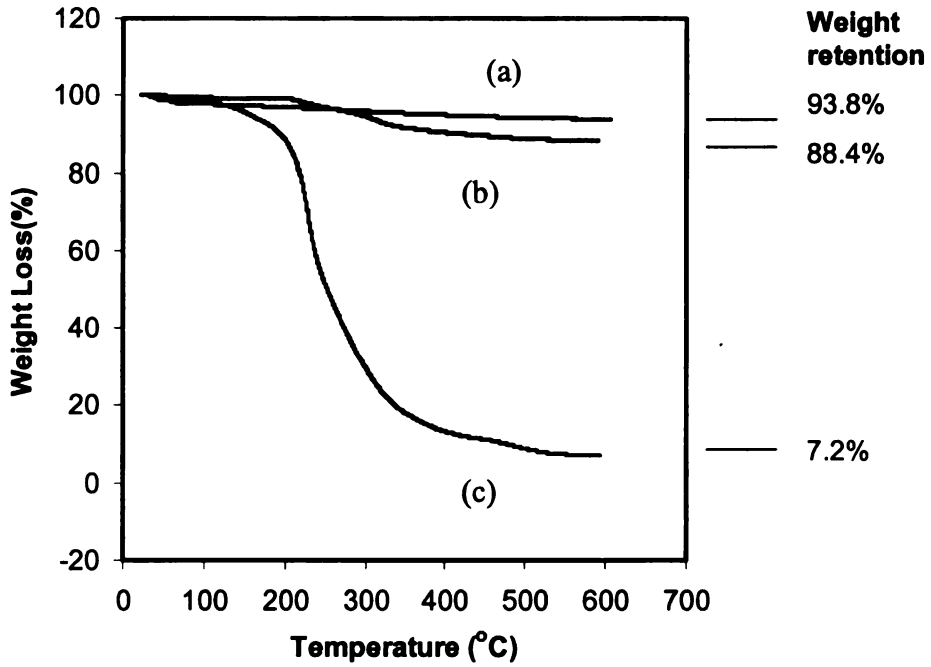

Figure 3.11. TGA analysis of: (a) bare fumed silica; (b) initiator-anchored fumed silica; (c) poly(PEGMA(22-23)) grown from fumed silica.

Table 3.2. Results from TGA control experiments.

Control Experiment	TGA weight loss
Mixture of fumed silica and monomer/catalyst solution	5-6%
Mixture of initiator attached fumed silica with monomer and $CuBr_2$ solution.	8%

Poly(PEGMA)(22-23) will crystallize at room temperature, but it has been proposed that when PEO chains interact with polar groups such as surface silanols, the dipolar and hydrogen bonding interactions in these groups would inhibit crystallization. Because of the high surface area of A200, it is plausible that poly(PEGMA(22-23)) may not crystallize. DSC results indicate that the attached PEGMA(22-23) chains are crystalline with T_m ~ 40 °C. Therefore, shorter macromonomers must be employed for applications where cystallization is deleterious.

Poly(PEGMA(4-5)) modified silica particles were prepared as described for poly(PEGMA(22-23)). These polymerizations are unremarkable, as the two monomers have nearly identical structures. The monomer and catalyst concentrations used for two polymerizations, targeting X_n = ~170 and 500, respectively, are shown in Table 3.1. TGA analysis indicated a 90% weight loss for these materials.

Table 3.3. DSC results of poly(PEGMA) silica particle composites.

Entry	TGA analysis	DSC results			
	Weight Loss	T_m (°C)	ΔH_m (J/g)	T_c (°C)	ΔH_c (J/g)
1	87%	40.04	76.44	-0.83	63.70
2	87%	40.39	71.95	-4.76	58.10

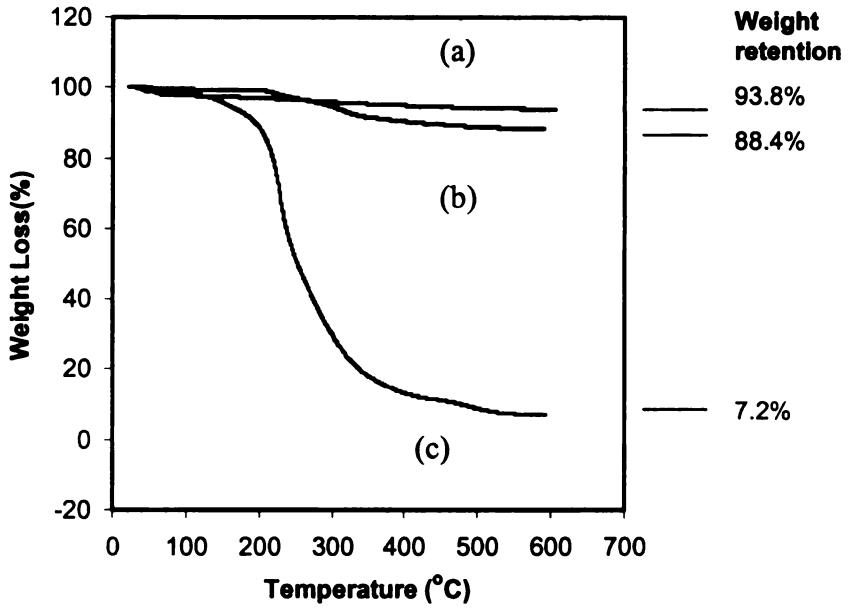

Figure 3.12. TGA analysis of (a) bare fumed silica; (b) initiator-anchored fumed silica; c) poly(PEGMA(4-5)) grown from the fumed silica surface.

Summary and Outlook

Comb-like polymer brushes were successfully grown from the surface of planar substrates (gold and silicon) and silica nanoparticles. Surface-initiated ATRP of PEGMA macromonomers yielded thick films under mild conditions. TGA analyses shows that the grafted polymer comprises ~ 90% of the particle weight. Poly(PEGMA(22-23)) grafted to silica particles is crystalline, however, poly(PEGMA(4-5)) grafted to similar silica particles is amorphous. The fast growth of polymer brushes from a variety of surfaces suggests possible applications in high throughput membrane formation.

References

1. Lee, J. H.; Lee, H. B.; Andrade, J. D., *Prog. Polym. Sci.* **1995,** *20*, 1043-1079.

2. Mrksich, M.; Whitesides, G. M., *ACS Symposium Series* **1997,** *680*, 361-373.

3. Zhu, X. Y.; Jun, Y.; Staarup, D. R.; Major, R. C.; Danielson, S.; Boiadjiev, V.; Gladfelter, W. L.; Bunker, B. C.; Guo, A., *Langmuir* **2001,** *17*, 7798-7803.

4. Sofia, S. J.; Premnath, V.; Merrill, E. W., *Macromolecules* **1998,** *31*, 5059-5070.

5. Feng, W.; Chen, R.; Brash, J. L.; Zhu, S., *Macromol. Rapid. Commun.* **2005,** *26*, 1383-1388.

6. Ma, H. W.; Wells, M.; Beebe, T. P.; Chilkoti, A., *Adv. Func. Mater.* **2006,** *16*, 640-648.

7. Matyjaszewski, K.; Miller, P. J.; Shukla, N.; Immaraporn, B.; Gelman, A.; Luokala, B. B.; Siclovan, T. M.; Kickelbick, G.; Vallant, T.; Hoffmann, H.; Pakula, T., *Macromolecules* **1999,** *32*, 8716-8724.

8. Xia, J. H.; Matyjaszewski, K., *Macromolecules* **1999,** *32*, 2434-2437.

9. Johnson, R. M.; Ng, C.; Samson, C. C. M.; Fraser, C. L., *Macromolecules* **2000,** *33*, 8618-8628.

10. Bo, G.; Wesslen, B.; Wesslen, K. B., *J. Polym. Sci. A: Polym. Chem.* **1992,** *30*, 1799-1808.

11. Luo, N.; Hutchison, J. B.; Anseth, K. S.; Bowman, C. N., *Macromolecules* **2002,** *35*, 2487-2493.

12. Okamura, S.; Katagiri, K.; Motoyama, T., *J. Polym. Sci.* **1960,** *43*, 509-516.

13. Brandrup, J. I., E.H., *Polymer Handbook.* Wiley Interscience: New York, 1975.

14. MacCallum, J. R., Vincent, C.A., *Polymer Electrolyte Reviews-1*. Elsevier Science Publishing Co. Inc.: New York, 1987.

Chapter IV

Crosslinked Polymer Brushes Containing PEO Segments

This chapter describes the synthesis and characterization of crosslinked polymer brushes with poly(ethylene oxide) (PEO) segments. Crosslinked brushes were grown from gold substrates by copolymerization of a macromonomer, poly(ethylene glycol) methyl ether methacrylate (PEGMA), and a crosslinker, bisphenol A ethoxylate dimethacrylate (BisA-EDMA) using surface-initiated ATRP. The crosslink density of the film was estimated from FT-IR measurements and the aqueous swelling of the films, as measured by *in-situ* ellipsometry.

Introduction

PEG coated surfaces are very effective in reducing protein adsorption and cell adhesion, and crosslinked PEG films should be particular well-suited for biological applications,[1, 2] because of the enhanced dimensional stability and mechanical properties of crosslinked polymer films. Moreover, crosslinking inhibits crystallization, and films derived from PEGMA and BisA-EDMA may prove useful for membrane-based gas separations.[3] In addition, since crosslinking seldom goes to 100% conversion, the residual vinyl groups may serve as sites for attaching additional functional groups.[4]

Currently, most crosslinked polymer films are formed by photo-initiated polymerization or conventional free radical polymerization. However, these methods afford limited control over the polymer architecture and often suffer from side reactions.

Surface-initiated ATRP can generate polymer brushes with a range of architectures under mild conditions, but only a few studies address crosslinked polymer brushes. Huang *et al.* previously reported the controlled synthesis of crosslinked polymer films by ATRP of ethylene glycol dimethacrylate (EGDMA) at room temperature. In this study, we extend that work to the copolymerization of a macromonomer (PEGMA) and a crosslinker (BisA-EDMA), and study the relationship between crosslinking density and film properties. The polymers incorporate oligomeric PEO units, which suggests potential medical applications and useful materials for membrane-based separations.

Experimental

Materials. Unless otherwise noted, all materials were obtained from Aldrich. BisA-EDMA, M_n = 1,700 g/mol, was passed through a column packed with a commercial inhibitor removal agent (Aldrich). PEGMA (M_n =1,100g/mol), Cu(I)Br (99.999%), and Cu(II)Br_2 (99.999%) were used as received. 2,2'-Bipyridine (bpy) was recrystallized from hot hexane, and then sublimed under vacuum at 60 °C to afford white crystals. Milli-Q water (18 MΩ), and *N,N*-dimethylformamide (DMF) (HPLC grade, inhibitor free) were used as polymerization solvents.

Characterization methods. Reflectance FT-IR was performed using a Nicolet Magna-IR 560 spectrometer with a PIKE grazing angle of 80 °C. Film thicknesses were measured by a rotating analyzer spectroscopy ellipsometer (M-44; J.A. Woollam) at a 75° angle of incidence. The refractive index and film thickness were calculated simultaneously by the values of Δ and Φ. Film thickness measured under N_2 and water were obtained using a home-built cell with glass windows. After measuring the refractive

index and film thickness of the polymer film in N_2-filled cell, the cell was filled with deionized water. The optical constant of water-swollen film is between 1.33 (the refractive constant of water) and 1.5 (polymer film refractive index).

Synthesis of crosslinked polymer brushes. A stock catalyst solution was prepared in a drybox by adding CuBr (0.043 g, 10 mM), $CuBr_2$ (0.02 g, 3 mM), and bpy (0.14 g, 30 mM) to 30 mL of DMF. The solution was sealed in a flask and transferred to a N_2 filled glovebag. Monomer (PEGMA), crosslinker (BisA-EDMA) and water were added to a Schlenk flask and stirred until homogeneous. The overall concentration of monomer and crosslinker was fixed at 0.4 M, and the monomer to crosslinker ratio was varied to obtain the desired polymer brush composition. For a polymerization using 30 mol% crosslinker, 15.4 g of PEGMA (0.014 mol), 10.8 g of BisA-EDMA (6 mmol), and water (19 mL) were added to a Schlenk flask. The solution was degassed via three freeze-pump-thaw cycles, and back-filled with N_2. A portion of the stock catalyst solution (5 mL) was added to the mixture under N_2, resulting in final catalyst concentrations of [CuBr] = 1 mM, [$CuBr_2$] = 0.3 mM, and [bpy] = 3 mM. The solution was stirred until homogeneous and then was added to a series of vials, each containing one initiator-anchored gold slide. Slides were removed from vials at predetermined times. Each slide was rinsed with a copious amount of water, ultrasonically cleaned in water and ethanol baths, rinsed with ethanol, and dried under a stream of N_2.

Determination of cross-link density of polymer brushes.

(a) The composition of copolymer films.

The composition of the crosslinked films was evaluated by infrared spectroscopy. The C=O stretching band at 1739 cm^{-1} provides information about PEGMA and BisA-EDMA while the band for aromatic C=C stretching at 1608 cm^{-1} is an exclusive marker for BisA-EDMA. The composition of the polymer film is χ mol% crosslinker (BisA-EDMA), and (1- χ) mol% PEGMA. The ratio of two absorption peaks (aromatic C=C stretch and C=O peaks) in the IR spectra of a 100% BisA-EDMA film is:

$$A_{ar\ C\text{-}C} / A_{C=O} = a \qquad (4.1)$$

and for the copolymer films:

$$A'_{ar\ C\text{-}C} / A_{C=O} = b \qquad (4.2)$$

Since, the C=O absorption of peaks for BisA-EDMA and PEGMA (at the same thickness) are comparable, combining equations (4.1) and (4.2) provides χ, the mole fraction of the crosslinker in the film.

$$\chi = b/a$$

The same calculations were made for a series of films polymerized at various crosslinker feeds, and the calculated mole fraction of cross-linker in the polymer, F_2 was plotted as a function of the mole fraction of cross-linker in the feed solution, f_2.

(b) Crosslink density determination.

The cross-link density of polymer films can be estimated from the residual vinyl groups in the polymer film. As PEGMA has only one double bond, any residual double bonds in films must be due to unpolymerized C=C double bonds in the BisA-EDMA crosslinker. As shown in Figure 4.1, a crosslink forms when both vinyl groups of the

crosslinker react; a branch forms when only one vinyl group reacts. The first situation includes cases of "intramolecular" crosslinking, formation of a loop, which is commonly seen in copolymerization of vinyl and divinyl monomers.[5] While loops do not have the same consequences as a regular crosslink, in this study, loops will be counted as crosslinks. Thus, the calculated crosslink density will overestimate the true value.

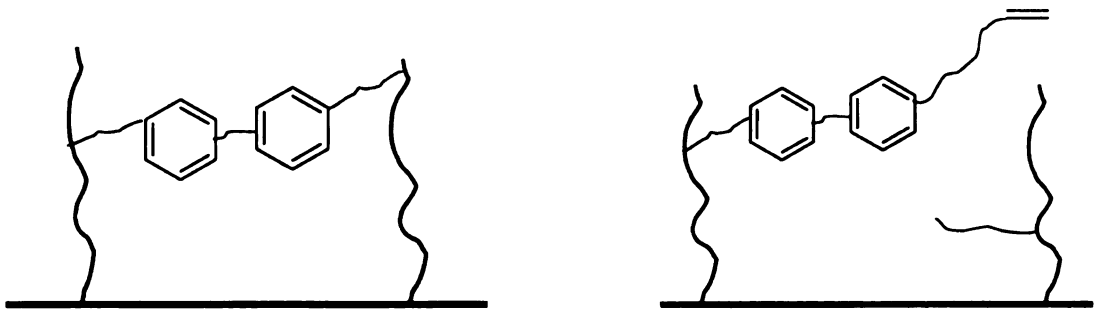

I II

Figure 4.1 Crosslinking and branching in films containing BisA-EDMA

If the probability of crosslinking is y, the probability of branching is 1-y. From the IR spectrum of a BisA-EDMA homopolymer film:

$$A_{C=C} / A_{arC-C} = C_1 \qquad (4.3.)$$

In the copolymer films:

$$A'_{C=C} / A_{arC-C} = C_2 \qquad (4.4.)$$

Combining equations (4.3) and (4.4), the probability of cross-linking (case **I**) is

$$y = 1 - (2C_2/C_1)$$

Taking into account of the actual mole fraction of crosslinker in films (defined as χ), we obtain the crosslinking density in the polymer film, which is defined as:

$$\text{Crosslink density} = \chi \times y$$

Results and Discussion

Synthesis of crosslinked polymer brushes. Scheme 4.1 outlines the synthetic route used to prepare crosslinked polymer brushes. PEGMA and the BisA-EDMA crosslinker were copolymerized from initiators anchored gold surfaces by aqueous surface-initiated ATRP. The preparation of the initiator-anchored gold substrates was described in previous chapters. For surface polymerization, the slides were immersed in an aqueous solution of monomer, crosslinker and the $CuBr/CuBr_2$/bpy catalyst mixture. In each polymerization, the total concentration of monomer and crosslinker is held constant, and the mole ratio of monomer to crosslinker were varied to obtain polymer brushes with different crosslink densities. In some UV-induced polymerizations, it was found that the crosslink density in the polymer increased as the crosslinker concentration increased in the pre-polymer solution.[6-8] Significant chain transfer and the use of sacrificial initiator are incompatible with these polymerizations due to the formation of gels in the solution, which are very difficult to remove from the substrate. After polymerization, polymer films were rinsed with large amounts of water, sonicated in DMF, rinsed with ethanol, and finally dried in a stream of N_2.

FT-IR spectra of the substrates showed a large increase in the ester carbonyl band at 1730 cm^{-1}, appearance of broad C-O-C peaks at 1150 cm^{-1}, and aromatic C=C bands at 1608 cm^{-1} and 1530 cm^{-1} (compare Figure 4.2 trace a & b), confirming the growth of a copolymer layer from the surface. In addition, the C=C stretching band at 1640 cm^{-1} indicates unreacted BisA-EDMA vinyl groups in the copolymer film, which may be used for further derivatization. From the width and position of the absorption peaks, we conclude that the crosslinked polymer film is amorphous.

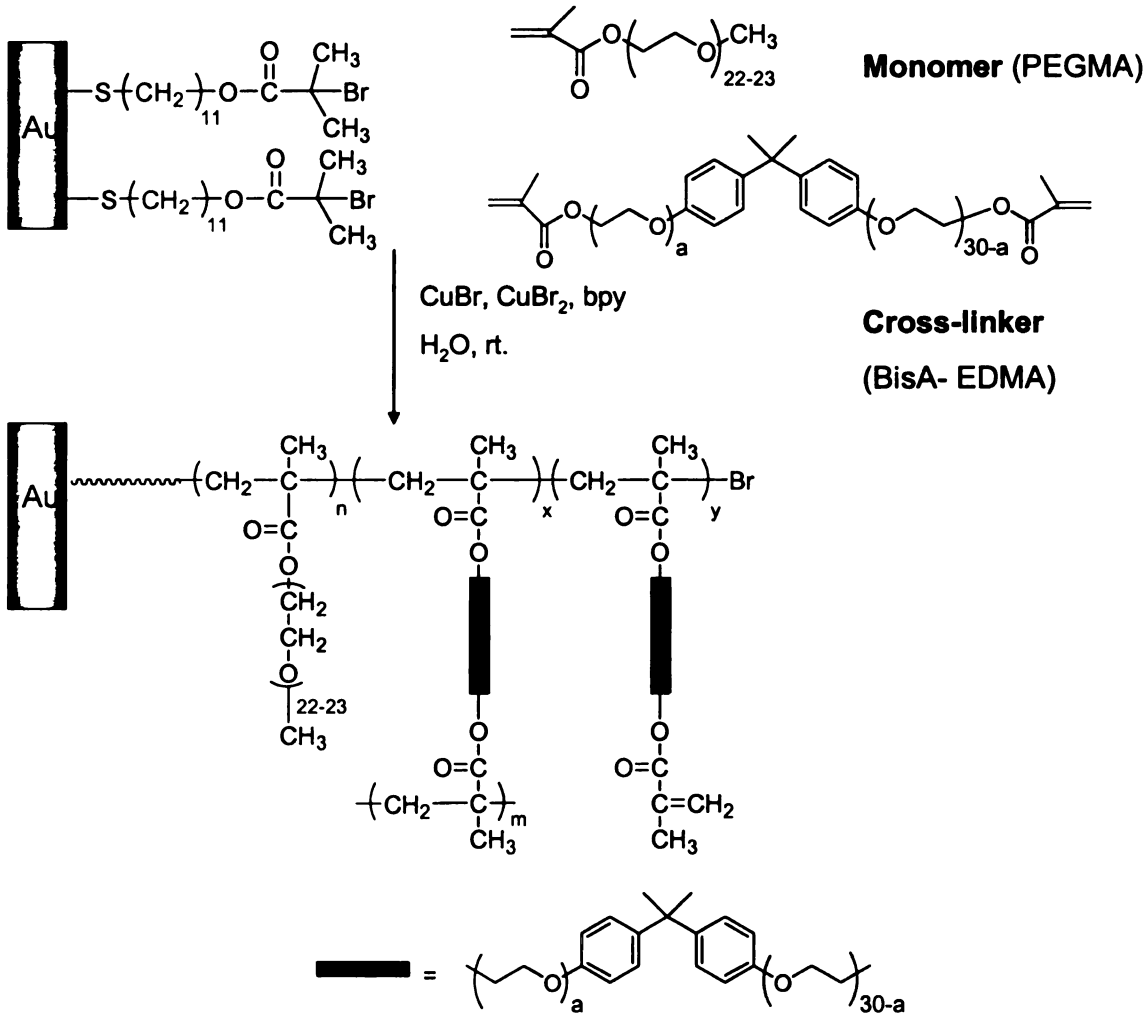

Scheme 4.1. Synthetic route to crosslinked copolymer films grown from gold substrates.

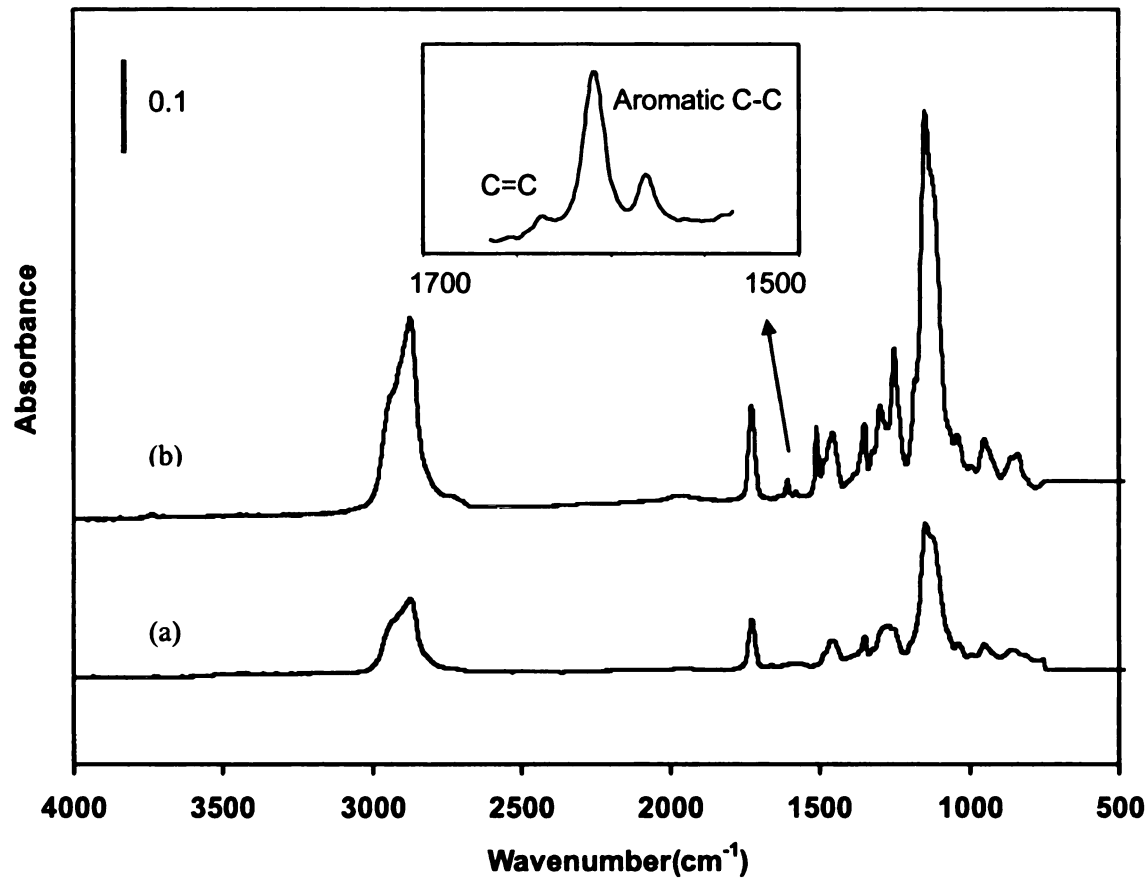

Figure 4.2. Reflectance FT-IR spectra of polymer films grown from an initiator anchored planar Au surface: (a) a poly(PEGMA) film and (b) a crosslinked copolymer film with 30 mol% crosslinker in the feed.

Figure 4.3 shows the evolution of film thickness as a function of reaction time for different feed solution compositions. As the mole fraction of crosslinker added to the polymerization increased, the polymerization rate and film thickness decreased. Homopolymerization of PEGMA yielded a 90 nm thick film in a 4 h polymerization, but the film thickness dropped to 50 nm when the feed composition 50 mol% crosslinker. In addition, the polymerization rate decreased to half of the homopolymer rate. Addition of the BisA-EDMA crosslinker has a negative affect on polymerization, however, the reason is not yet resolved. One possible explanation is that as more crosslinker is incorporated into the film, the polymer chains are more entangled, which makes the terminal Br less accessible to the copper catalyst. Therefore, both polymerization rate and polymer film thickness decrease.

Characterization of crosslinked polymer films. The composition of polymer brushes was estimated by integration of characteristic absorption peaks shown in FT-IR spectra of crosslinked polymer brushes. The mole fraction of crosslinker in the polymer film was inferred from the absorbance of aromatic C=C peak, relative to that of the C=O band (see the experimental section for details). The results from films prepared with various feed compositions are shown in Figure 4.4. The data shows that the feed and film compositions are nearly linearly related, indicating that despite their size and structural differences, incorporation of PEGMA and BisA-EDMA is differences in reactivity or diffusion to the reactive sites surface on the substrate.[9]

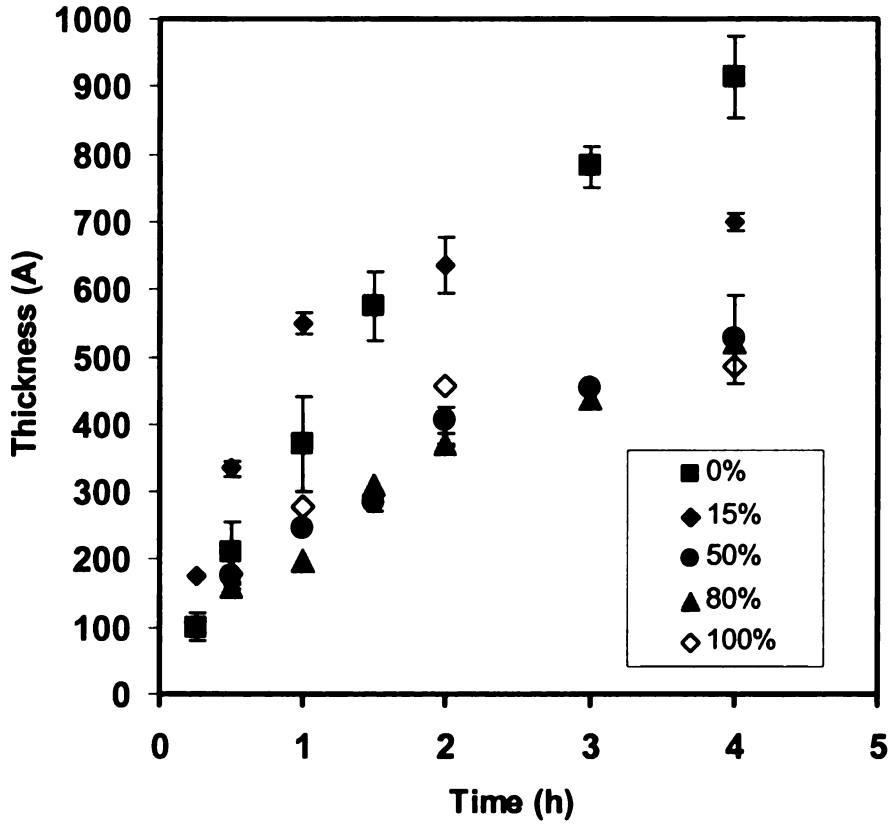

Figure 4.3. Evolution of film thickness with time for the copolymerization of PEGMA and BisA-EDMA. The overall concentration of monomer and crosslinker for all runs is 0.4 M. Catalyst: [CuBr] = 1mM; [$CuBr_2$] = 0.3mM; [bpy] = 3mM. The inset shows the mole % composition of BisA-EDMA in the monomer feed solution.

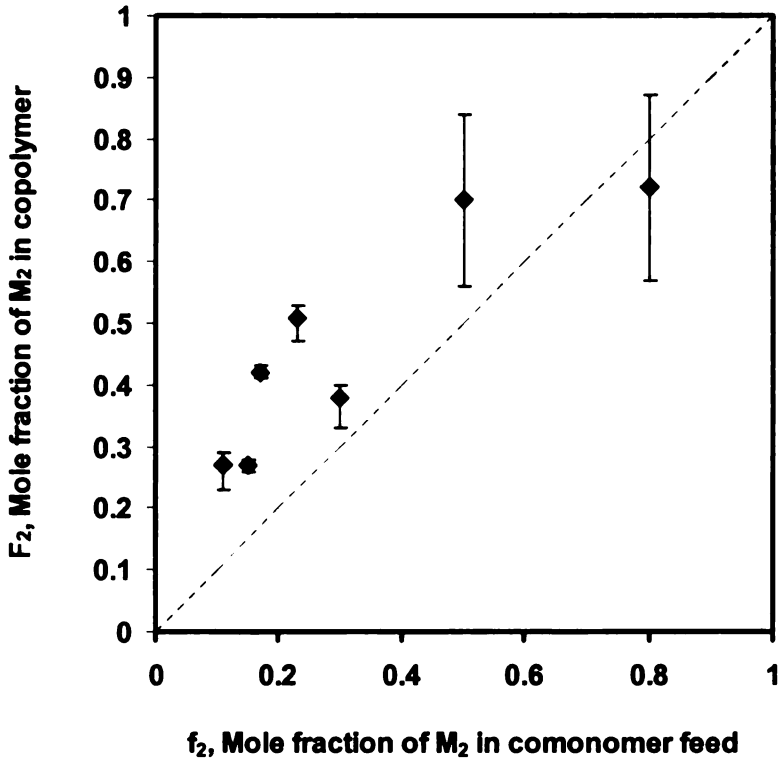

Figure 4.4. The relationship between the feed composition and the measured film composition. Each point is the average of at least three independent samples.

We are interested in quantifying the residual vinyl groups in the film since they may be used for further elaboration of the membranes. As detailed in the experimental section, comparison of the vinyl C=C and the aromatic C=C stretching bands provide information on the fraction of BisA-EDMA double bonds that were not polymerized The data show that the fraction of BisA-EDMA vinyl bonds polymerized is approximately 80%, and independent of the BisA-EDMA composition in the feed. There was, however, significant run to run variation in films prepared with high crosslinker feed ratios.

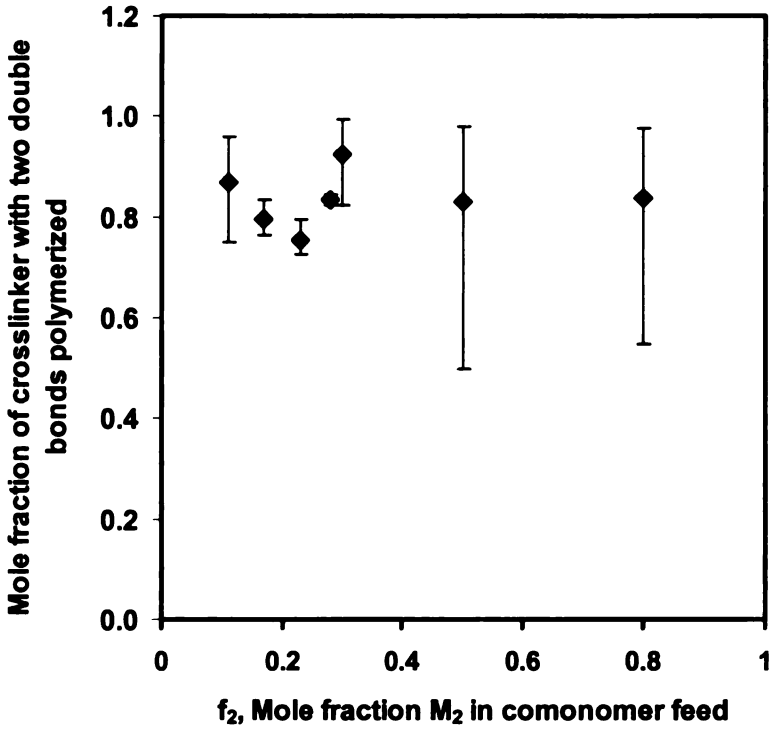

Figure 4.5. The fraction of crosslinkers in which both double bonds participate in the polymerization. Each point is the average of at least three independent samples.

The crosslink density can be defined from the data above:

$$Density(X-link) = \frac{M(x-link)}{M(BisA-EDMA)} \bullet \frac{M(BisA-EDMA)}{M(BisA-EDMA)+M(PEGMA)}$$

$$Density(X-link) = \frac{M(x-link)}{M(BisA-EDMA)+M(PEGMA)} \qquad (4.5)$$

The near linear relationship between the feed and measured compositions, and the nearly constant crosslink efficiency (~80%) imply that the crosslink density should be linearly related to the mole fraction of the crosslinker in the feed, as shown in Figure 4.6. Except for the 80 mol% point, the general trend is a linear relationship, which may reflect some variability in membrane synthesis or the limitations of the IR data.

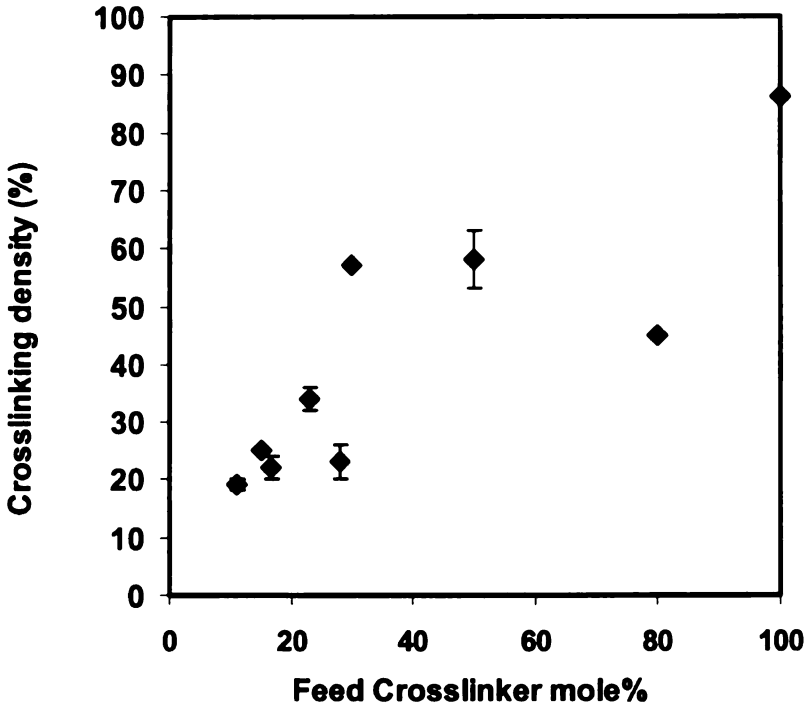

Figure 4.6. Crosslink density *vs.* the mole percentage of crosslinker in the feed.

In addition to estimating the crosslink density, FT-IR spectra also provide information on the morphology of the films. The IR data show that films copolymerized from feed solutions with less than <15 mol% BisA-EDMA are crystalline, but all BisA-EDMA mole fractions >15 mol% produced amorphous films.

Swelling behavior of crosslinked copolymer films. Figure 4.7. shows dry and water swollen thicknesses for polymer films prepared at different crosslinker feed ratios. The dry films ranged from 20-30 nm and correspond to compositions of 0% to 100% poly(BisA-EDMA). In Figure 4.7b, the normalized swelling is plotted as a function of crosslinking density to better illustrate the relationship between film structure and swelling behavior. The swelling ratio is defined as

$$\text{Swelling ratio} = \frac{d(wet) - d(dry)}{d(dry)} \times 100\% \qquad (4.6)$$

where d is the film thickness.

As shown in Figure 4.7b, the swelling ratio decreased with cross-link density and plateaued at >40% crosslink density. The former indicates increasing dimensional stability with crosslinking, which is characteristic of crosslinked films, while 160% swelling may represent the inherent swelling due to the long PEO segments in the two monomers. Qiao *et al.* [10] observed the increased swelling of PEG dimethacrylate network as the length of PEG segments increased.

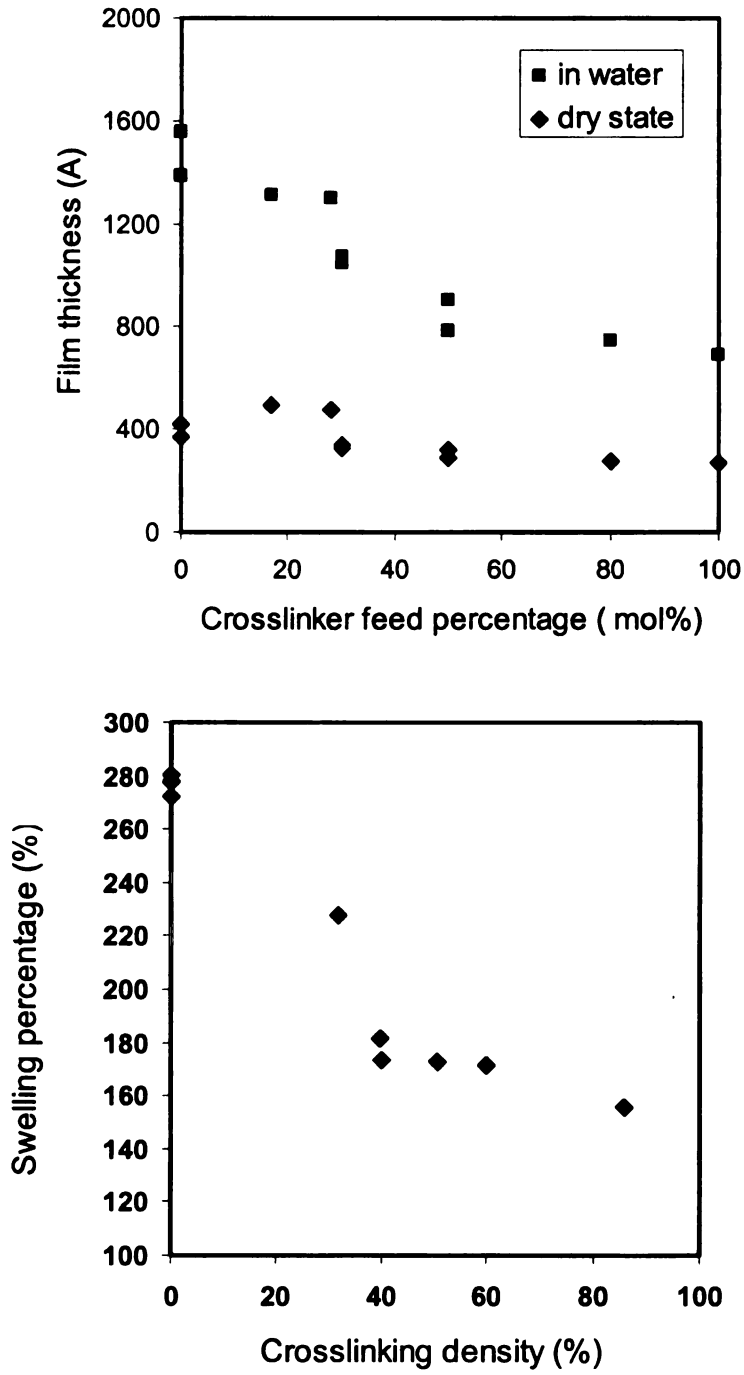

Figure 4.7. a) (Top) thickness of dry and water-swollen films as a function of the mole percentages of crosslinker in the monomers feed solution; b) (bottom) the relationship between the normalized swelling of films and the film crosslink density.

Conclusion and Outlook:

Crosslinked polymer brushes containing PEO segments were grown from the surface of gold substrates using surface-initiated ATRP. The addition of the cross-linker to PEGMA slowed the polymerization rate. Using the aromatic ring of BisA-EDMA as a reference, the film structure and crosslink density were measured by an analysis of the IR spectra of crosslinked films. Aqueous swelling of copolymer films in water decreases with increasing crosslink density, and is nearly constant for crosslink densities >40%. The gas permeation characteristics of crosslinked-polymer membranes grafted on porous alumina supports are described in Chapter V.

References:

1. Nolan, C. M.; Reyes, C. D.; Debord, J. D.; Garcia, A. J.; Lyon, L. A., *Biomacromolecules* **2005,** *6*, 2032-2039.

2. Groll, J.; Amirgoulova, E. V.; Ameringer, T.; Heyes, C. D.; Roecker, C.; Nienhaus, G. U.; Moeller, M., *J. Am. Chem. Soc.* **2004,** *126*, 4234-4239.

3. Lin, H.; Wagner, E. V.; Freeman, B. D.; Toy, L. G.; Gupta, R., *Science* **2006,** *311*, 639-642.

4. Heggli, M.; Tirelli, N.; Zisch, A.; Hubbell, J. A., *Bioconjugate Chem.* **2003,** *14*, 967-973.

5. Matsumoto, A.; Ohashi, T.; Oe, H.; Aota, H.; Ikeda, J. I., *J. Polym. Sci. A: Polym. Chem.* **2000,** *38*, 4396-4402.

6. Baker, J. P.; Hong, L. H.; Blanch, H. W.; Prausnitz, J. M., *Macromolecules* **1994,** *27*, 1446-1454.

7. Elliott, J. E.; Macdonald, M.; Nie, J.; Bowman, C. N., *Polymer* **2004,** *45*, 1503-1510.

8. Kizilay, M. Y.; Okay, O., *Macromolecules* **2003,** *36*, 6856-6862.

9. Odian, G., *Principles of Polymerization.* Wiley-Interscience: New York, 2004.

10. Qiao, C.; Jiang, S.; Dong, D.; Ji, X.; An, L.; Jiang, B., *Macromol. Rapid Commun.* **2004,** *25*, 659-663.

Chapter V

Polymer Membranes for Gas Separation

This chapter describes the development of polymeric membrane materials and studies of gas permeation through membranes, emphasizing the separation of CO_2 from light gases such as H_2 and N_2. Comb and crosslinked polymer brushes containing PEO units were grafted to the surface of porous alumina membrane supports by surface-initiated ATRP. Due to the interactions between CO_2 and the ether oxygens of the ethylene oxide units, the modified membranes are highly permeable to CO_2 and selectively permeate CO_2. For poly(PEGMA) films, the measured permeability of CO_2 is ~300 Barrer with a CO_2 /H_2 selectivity of 14. CO_2 permeability and selectivity decreased as the PEO side chain of the comb polymer was shortened. CO_2 and H_2 permeability, and the CO_2/H_2 permselectivity decreased as more crosslinker was incorporated in the film.

Background

During the last decade, gas separation by polymeric membranes has been widely studied as an alternative to traditional gas separation technology. The emphasis of this research has focused on the recovery of H_2 from petrochemical process streams, removal of CO_2 from hydrocarbon mixtures, and removal of acidic gases from natural gases. [1]

The steady state permeability of gas A, through a film with thickness of l, is defined as:[2]

$$P_A \propto F_A \, l/\Delta p \qquad (1)$$

where F_A is the steady state flux of gas through the film (cm^3 (STP)/cm^2 s), l is the film thickness and Δp is trans-membrane pressure (cmHg). Permeability coefficients are commonly expressed in units of Barrers, where 1 Barrer = 10^{-10} cm^3 (STP) cm/(cm^2 s cmHg). When the upstream pressure (p_1) is much higher than the downstream pressure (p_2), Δp can be approximated as p_1. The permeability of gas A through a polymer matrix can be expressed as the product of the average effective diffusivity, D_A, and the apparent solubility of gas A in the polymer, S_A.[2]

$$P_A = D_A \times S_A \qquad (2)$$

According to this diffusion/solubility model, a penetrant gas dissolves in the high pressure side of the film, diffuses through the film, and then desorbs at the low pressure side of the film. The ideal membrane selectivity for gas A over gas B is expressed as:

$$\alpha\,(A/B) = P_A/P_B = (D_A/D_B) \times (S_A/S_B) = \alpha_D \times \alpha_S \qquad (3)$$

where α_D is the diffusivity selectivity, and α_S is the solubility selectivity.

The gas diffusivity increases with decreasing penetrant (gas) size (lower critical volume or kinetic diameter of the penetrant), increasing polymer chain flexibility (increased free volume), and decreasing polymer chain and penetrant interactions. The penetrant solubility increases with increasing condensability (higher boiling point or critical temperature) and stronger gas-polymer interactions.[3,4] As shown in Table 5.1, the critical volume and kinetic diameter (d_k) are used as a metric for penetrant size. Considering only molecular size, H_2 is smaller and has a higher diffusion coefficient than CO_2. However, CO_2 has a higher boiling point and critical temperature than H_2, and therefore, it is more condensable than H_2.

Many commercially available membranes are based on glassy polymers, and are designed to maximize the gas diffusivity selectivity. Those membranes are more permeable to H_2 than to CO_2, since α_D favors H_2 much more strongly than α_S favors CO_2. One way to improve the permeability of glassy membranes is to increase chain mobility by adding a plasticizer. However, plasticization of glassy polymers would be detrimental to membrane performance. When the polymer absorbs a high concentration of a condensable gas (CO_2), the polymer swells and softens. The diffusion coefficient of large molecule (CO_2) increases more rapidly than small molecule (H_2), resulting in the loss of diffusion selectivity.

Table 5.1. Physical properties of H_2, CO_2, and N_2[5, 6]

	Size		Condensibility		Solubility paramenter
	Critical Volume (cm^3/mol)	d_k (nm)	Boiling point (K)	Critical temperature (K)	δ ($MPa^{0.5}$)
H_2	65.1	0.289	20.4	33.2	6.6
N_2	89.8	0.364	77.4	126.2	5.3
CO_2	93.9	0.330	195	304.2	12.2

Since the diffusivity ratio α_D [=$D(CO_2)/D(H_2)$] is unfavorable, a common strategy for separating CO_2 and H_2 is to design rubbery membranes that have a high solubility ratio α_S [= ($S(CO_2)$/ $S(H_2)$]. A high solubility for CO_2 relative to light gases also is very useful for CO_2/N_2 separation, since their sizes and critical volumes are similar (see Table 5.1.). The solubility of a gas depends on the physical properties of the gas, such as boiling point and critical temperature, but more importantly, solubility is related to polymer/gas

interactions. PEO is perhaps the best material for the separation of CO_2 due to favorable interactions between the ether oxygens and CO_2. Membranes more permeable to CO_2 than H_2 are called "*reverse selective*" membranes. Plasticization, which is detrimental to the glassy polymers, actually benefits PEO-containing reverse selective membranes, since it increases $D(CO_2)/D(H_2)$, yielding a higher CO_2/H_2 selectivity.

High molecular weight PEO is semi-crystalline. The formation of a crystalline phase would reduce the CO_2 gas permeability because only ethylene oxide segments in the amorphous phase could interact with CO_2 and solubilize CO_2. There are several strategies for incorporating PEO segments into polymers while avoiding PEO crystallization including the use of low molecular weight PEO, block copolymers with short PEO blocks, graft and comb polymers with short PEO segments as side chains, and cross-linked PEO networks. PEO-containing monomers commonly used to synthesize such structures are shown in Scheme 5.1. Table 5.2 lists CO_2 permeabilities and CO_2/H_2 selectivities for representative membrane materials. More CO_2/N_2 separation data appear in reference 10.

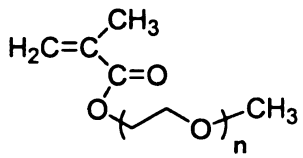

PEGMA

1. n = 4-5

2. n = 8-9

3. n = 22-23

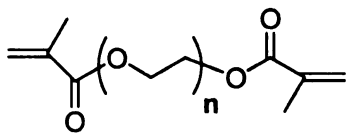

PEGDMA

4. n = 4

5. n = 14

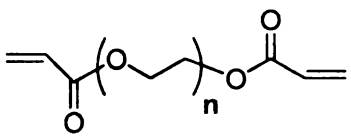

PEGDA

6. n = 4

7. n = 14

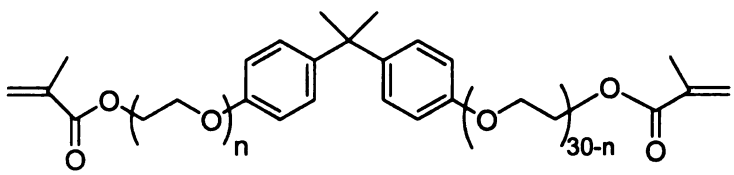

8. BisA-EDMA

Scheme 5.1. Structures of representative PEG (meth)acrylates and PEG di(meth)acrylates used in this study and reported in the literature for membrane separations.

Table 5.2. Representative examples of pure gas CO_2 permeability and CO_2/H_2 selectivity in PEO-containing polymers.

Permeability and Selectivity Polymer		P(CO_2) (Barrer) [b]	α (CO_2/H_2) [c]	Reference
Semi-crystalline PEO		13 (35 °C)	6.7 (1 atm)	Lin[7]
Liquid PEG blend with solid PDMS		N/A	7.5(25 °C)	Lin [8]
PEG soft block and polyimide hard block		66 (35 °C) 120 (35 °C)	7.8 (35 °C) 9.8 (35 °C)	Bonder[9, 10]
Crosslinked PEO films	50 wt% **2**/ 50 wt% **7** [a]	260 (35 °C)	10	Freeman [8]
	70 wt% **2** / 30 wt% **7**	320 (35 °C)	11 (35 °C) 40 (-20 °C)	
	99 wt% **2**	570 (35 °C)	12	
Crosslinked polyethers	PEG di-acrylate (**7**)	70 (23 °C)	9.5	Patel [11-13]
	50/50 w/w PEG di-acrylate/PPG diacrylate	100	5	

[a] The number refers to the structures in Scheme 5.1.

[b] Permeability coefficient: 1Barrer $=10^{-10}$ cm^3 (STP) cm/(cm^2 s cmHg).

[c] Selectivity α (CO_2/H_2) = P (CO_2)/ P(H_2).

Our strategy is to develop composite polymer membranes in which a thin polymer skin is deposited on the surface of a porous aluminum membrane support. Solution casting,[14] and solution coating,[15] plasma polymerization [16, 17] and UV-induced grafting,[18, 19] are the most common ways to prepare composite membranes. The principal challenge in these methods is the difficulty in controlling film thickness. Surface-initiated ATRP allows controlled growth of polymer brushes on the surface, and it may provide access to membranes with well-defined polymer brush skins. In this chapter, we describe the grafting of PEO-containing combs and crosslinked polymer brushes from the surface of porous alumina membrane supports, and examine the CO_2, H_2 and N_2 gases permeability through these membranes.

Experimental

Materials. Poly(ethylene glycol) methyl ether methacrylate (PEGMA, M_n = 300 g/mol and 1,100 g/mol), Cu(I)Br (99.999%), Cu(II)Br_2 (99.999%), tetramethyl-1,4,8,11-tetraazacyclotetradecane (Me_4Cyclam), 4,4'-di-(*n*-nonyl)-2, 2'-bipyridine (dnNbpy) were used as received from Aldrich. Bisphenol A ethoxylate dimethacrylate (BisA-EDMA, M_n = 1,700 g/mol) was passed through a column packed with a commercial inhibitor removal agent (Aldrich) to remove hydroquinone inhibitor. Milli-Q water (18 MΩ), *N,N*-dimethylformamide (DMF) (HPLC grade, inhibitor free) were used as polymerization solvents.

Characterization methods. Field-emission scanning electron microscopy (FESEM, Hitachi s-4700II, acceleration voltage of 15 kV) was used to characterize the film growth on the porous aluminum membrane support. Membranes were freeze-

fractured using liquid N_2 prior to sputter coating with 5 nm gold for cross-sectional image analysis.

Anchoring initiators on the surface of porous alumina membrane support. Porous alumina membranes (0.02 μm) were cleaned in an UV/O_3 chamber for 15 min, washed with anhydrous ethanol and dried with N_2. The membranes were sputter-coated with 5 nm gold, and then were cleaned in the UV/O_3 chamber for an additional 10 min, washed with ethanol and dried under a stream of N_2. A self-assembled initiator monolayer was formed by immersing the gold-coated membrane in a 1 mM ethanolic solution of $[Br\text{-}C(CH_3)_2\text{-}COO(CH_2)_{10}S]_2$ for 24 h. The films were washed with a large amount of ethanol, sonicated in ethanol for 1 min, washed again with ethanol, and finally dried under a stream of N_2. To directly attach initiators to the alumina membrane, the membrane was immersed in a DMF solution of the trichlorosilane initiator (see chapter III) for 24 h, and then the membrane was washed with DMF and anhydrous ethanol, and dried under a stream of N_2 stream. The synthetic scheme is illustrated in Figure 5.2.

Surface-initiated ATRP of poly(PEGMA) films using CuBr/CuBr$_2$/bpy catalyst. A catalyst solution was prepared in an oxygen-free drybox by adding CuBr (0.057 g, 20 mM), $CuBr_2$ (0.045 g, 6 mM) and bpy (0.18 g, 60 mM) to 20 mL of DMF, and then transferring the solution to a N_2-filled glove bag. PEGMA (15 g) and Milli Q water (14 mL) were added to a Schlenk flask and stirred until homogeneous. The flask was connected to a vacuum line and the solution was degassed using three freeze-pump-thaw cycles, back-filled with N_2, and then transferred to the N_2-filled glove bag. A portion of the catalyst solution (1.5 mL) was added to the flask, resulting in catalyst concentrations of [CuBr] = 1 mM, $[CuBr_2]$ = 0.3 mM, and [bpy] = 3 mM. The solution was transferred

into a container holding an initiator-anchored membrane. After 12 h, the membrane was removed from polymerization solution, rinsed with large amount of water and DMF, cleaned in an ultrasonic bath with DMF, washed with anhydrous ethanol, and finally dried under a stream of N_2.

Polymerization of PEGMA using a CuBr/Me$_4$Cyclam/CuBr$_2$(dnNbpy)$_2$ catalyst. In a drybox, $CuBr_2$ and dnNbpy (1:2, mol:mol) were mixed together to form a green complex and stored for future use. A catalyst solution was prepared in an oxygen-free drybox by adding CuBr (0.057 g, 20 mM), $CuBr_2(dnNbpy)_2$ (0.21 g, 10 mM) and $Me_4Cyclam$ (0.1 g, 20 mM) to 10 mL of DMF. The solution was stirred until homogeneous (~ 20 min). A second Schlenk flask was loaded with PEGMA(4-5) (18 g, 0.05 mol) and H_2O (9 mL). The flask was connected to a vacuum line and the solution was degassed using three freeze-pump-thaw cycles, and finally back-filled with N_2. In a N_2-filled glovebag, a portion of the catalyst solution (3 mL) was added into the flask. The final catalysts concentrations were: [CuBr] = 2 mM, $[CuBr_2]$ = $[(dnNbpy)_2]$ = 1 mM, and [$Me_4Cyclam$] = 2 mM. The catalyst solution was added to the monomer solution, causing it to turn brown with the formation of a precipitate. The solution was immediately transferred into a vial containing the initiator-anchored membrane. The membrane was taken out at a predetermined times, ranging from 3 min to 10 min, to control the film thickness. The membrane was rinsed with a large amount of water and DMF, cleaned in an ultrasonic bath with DMF, washed with anhydrous ethanol, and finally dried under a stream of N_2.

Growth of crosslinked copolymer film. A stock catalyst solution was prepared in a drybox by adding CuBr (0.043 g, 10 mM), $CuBr_2$ (0.02 g, 3 mM), and bpy (0.14 g, 30

mM) to 30 mL of DMF. The solution was sealed in a flask and transferred to a N_2 filled glovebag. Monomer (PEGMA), crosslinker (BisA-EDMA) and water were added to a Schlenk flask and stirred until homogeneous. The total concentration of monomer and crosslinker was fixed at 0.4 M, and the monomer to crosslinker ratio was varied to obtain the desired polymer brush composition. For a polymerization with 30 mol% crosslinker, 15.4 g of PEGMA (0.014 mol), 10.8 g of BisA-EDMA (6 mmol), and 19 mL water were added to a Schlenk flask. The solution was degassed via three freeze-pump-thaw cycles, and back-filled with N_2. A portion of the stock catalyst solution (5 mL) was added to the mixture under N_2, resulting in final catalyst concentrations of [CuBr] = 1 mM, [$CuBr_2$] = 0.3 mM, and [bpy] = 3 mM. The solution was stirred until homogeneous and then was transferred into vials containing the initiator-anchored membranes. After a 12 h polymerization, membranes were removed from the solution, rinsed with a copious amount of water, ultrasonically cleaned in a DMF bath, washed with ethanol, and finally dried under a stream of N_2.

Gas permeation measurements. The permeation of gases (CO_2, H_2, and N_2) through the modified membranes was measured using a permeation cell with a pressure relief valve. The permeate flux was measured as a function of gas inlet pressure (5-50 psig) using a soap-bubble flow meter. Measurements were performed for each gas separately in the order H_2, N_2, and CO_2. For each gas, the permeation cell was purged with the gas several times to remove traces of other gases and to establish a stable gas flux. The flowmeter readout was converted to the flux using Eq 4:

$$F = v / A \qquad (4)$$

where F is the flux of the gas (cm^3 (STP)/cm^2 s), v is the flow rate of the gas (mL/min), and A is the area of the membrane (cm^2). Permeability coefficients were calculated according to Eq.1.

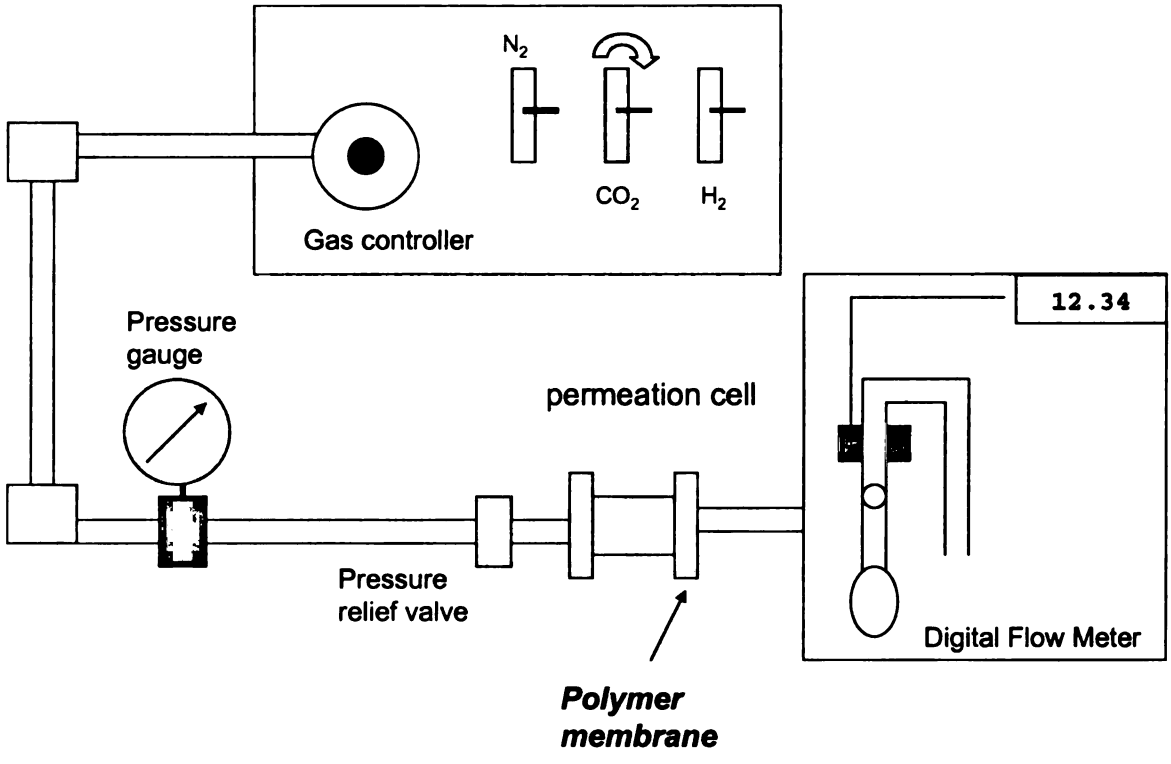

Figure 5.1. Apparatus for gas permeation measurements.

Results and Discussion

Synthesis of and characterization of polymer films

Polymer brushes were grafted from the surface of alumina membrane supports (0.02 μm pore size) using two methods. In the first, the membrane was sputter coated with 5 nm of gold, and then the thiol terminated initiator was attached by forming a self-assembled monolayer. Alternatively, trichlorosilane initiator precursors were directly coupled with OH groups to form Si-O-Si bonds. Using surface-initiated ATRP, PEGMA macromonomers were polymerized from the initiator layers to form comb polymer brushes with PEO side chains. Including a cross-linker (BisA-EDMA, 30-100 mol%) in the monomer pool allowed the growth of cross-linked films with various crosslink densities on the surface of porous alumina membranes.

Figure 5.2 shows transmission FT-IR spectra of polymethacrylates grafted on the surface of a porous alumina membrane support. Characteristic peaks observed in the spectrum, include C-H stretching at 2885 cm^{-1} and ester C=O stretching at 1729 cm^{-1}. The lengths of the PEO side chains in the two polymers are different, hence the different intensity ratios seen for C-H stretching and ester C=O bands. The ethylene oxide C-O-C stretching band is obscured by the Al-O-Al stretching band, located at ~1110 cm^{-1}. Because of the high pore density in the alumina substrates, ellipsometric measurements were not possible on these surfaces, and thus film thicknesses were estimated from the cross-sectional FESEM images. To demonstrate the potential of these materials in gas separations, we examined CO_2, N_2 and H_2 fluxes through these films grown on the surface of porous alumina membranes.

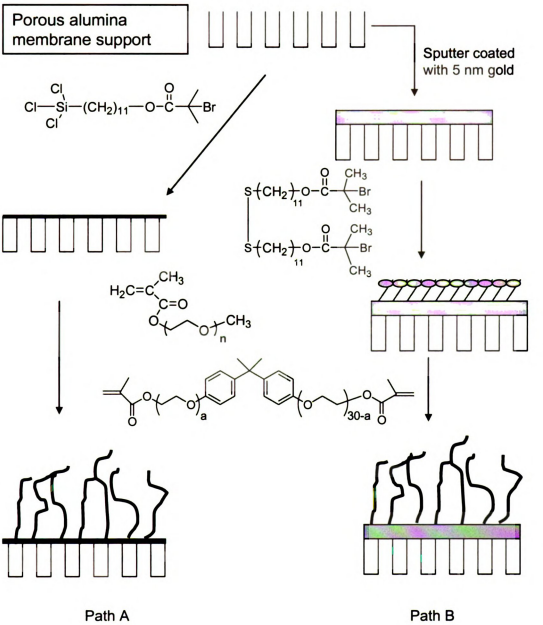

Figure 5.2. Synthesis of composite membranes with polymer skins.

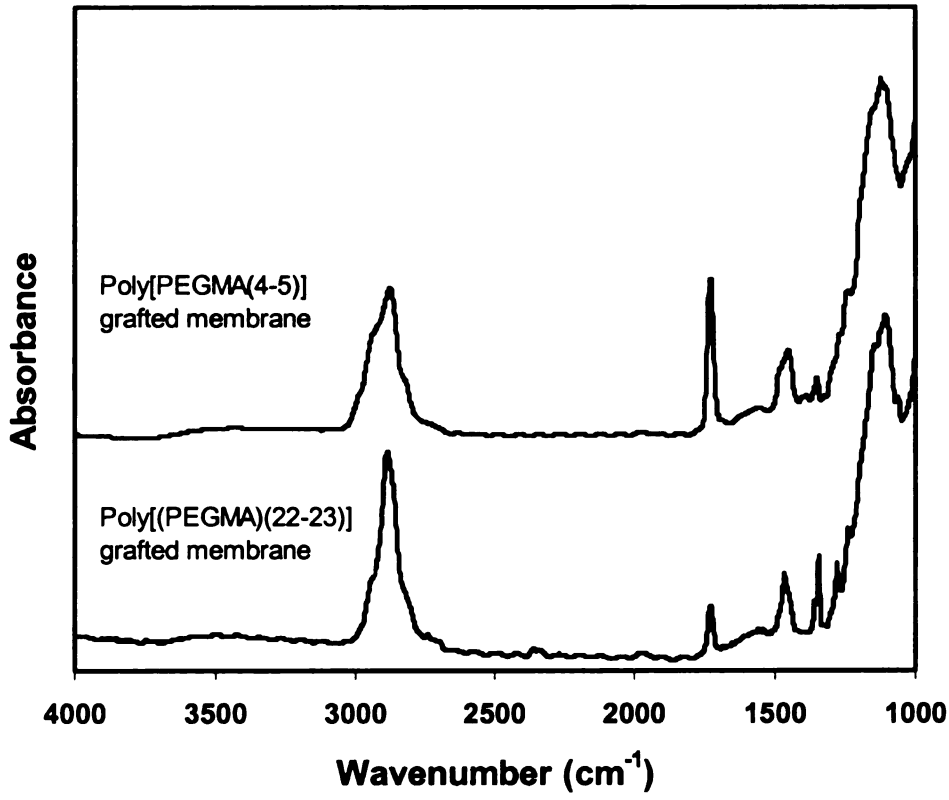

Figure 5.3. Transmittance FT-IR spectrum of poly(PEGMA(22-23)) and poly(PEGMA(4-5)) grafted to porous alumina membrane supports.

Pure gas permeation of poly(PEGMA) brushes.

The PEO side chain of poly(PEGMA(22-23)) contains 22-23 oxyethylene units per monomer repeat, which should provide a sufficient fraction of PEO to give high selectivity. A poly(PEGMA) film prepared by a 12 h surface-initiated ATRP was subjected to gas permeation measurements. As shown in Figure 5.4, this membrane showed a remarkable CO_2/H_2 selectivity of 14. The film thickness estimated from FESEM was ~1000 nm (Figure 5.5), and therefore the film has a CO_2 permeability of

~300 Barrers. This result is very promising when compared to prior work. This selectivity is slightly higher than the value of ~10 for typical crosslinked PEG-acrylates or PEG methacrylates, but the permeability is 4-fold greater.[13, 20]

Although the above results are very promising, this membrane was synthesized from a PEGMA monomer with long PEG side chains. As described in Chapter 2, these chains will eventually crystallize, degrading the membrane permeability. Indeed, later measurements with the same membrane, showed decreased gas flux and a drop in CO_2/H_2 selectivity.

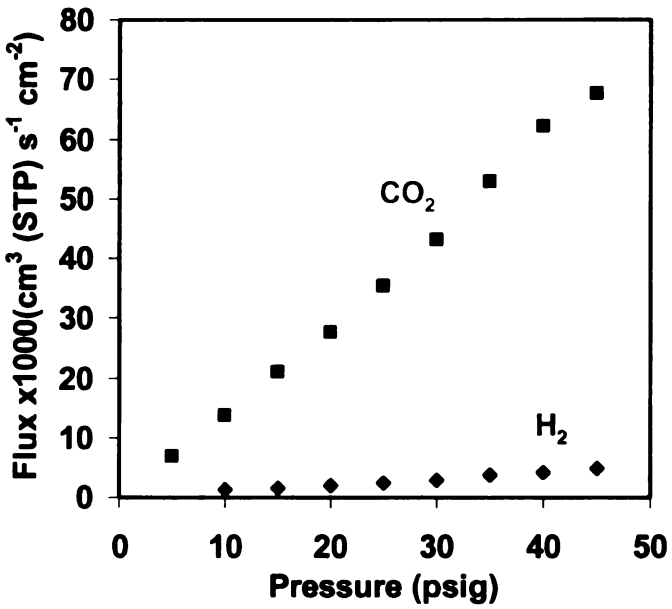

Figure 5.4. Single-gas fluxes of CO_2 and H_2 through films prepared by polymerization of PEGMA(22-23) from porous alumina as a function of trans-membrane pressure drop. The outlet pressure was 1 atm and the measurements were performed at room temperature.

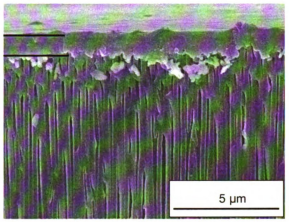

Figure 5.5. FESEM image of the filtrate side of a porous alumina after growth of a poly(PEGMA(22-23)) film from the surface.

The CO_2/H_2 selectivity can be recovered by eliminating film crystallinity. Since PEO is water-soluble, crystalline poly(PEGMA) films should be rendered amorphous by soaking with water. As shown in Figure 5.5 a crystalline film treated with water had a CO_2/H_2 selectivity of ~ 8, and a CO_2 permeability of ~ 75.7 Barrer. These data suggest that the film was partially crystalline. Either the length of time that the film was in water was too short to fully dissolve the crystals, or a small fraction of the PEO side chains quickly crystallized after the film was dried. The results are summarized in Table 5.3.

We also considered the possibility of operating gas permeation above the melting point of poly(PEGMA) (35-40 °C) to achieve high permeability and CO_2/H_2 selectivity, or storing membranes in CO_2 to plasticize the polymer matrix and inhibit crystallization. However, our current lab setup does not permit high temperature measurements and long storage in CO_2. An alternative approach to minimize crystallization is to utilize monomers with fewer ethylene glycol units, although this may result in a decrease in the film selectivity as the fraction of PEO in the film will be lower.

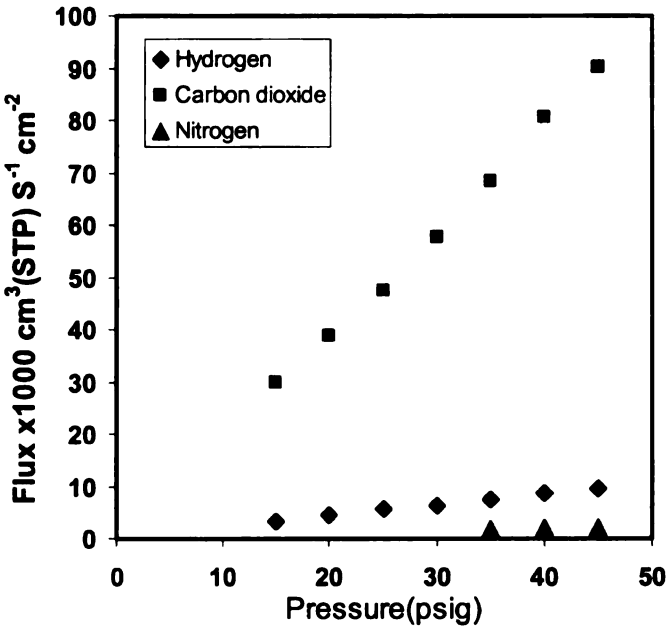

Figure 5.6. Single-gas fluxes of CO_2 and H_2 through a poly(PEGMA(22-23)) grafted membrane as a function of trans-membrane pressure drop. The initially crystalline film was soaked in water, and then measurements were taken after the film was dried.

Two additional macromonomers, PEGMA(4-5) and PEGMA(8-9), were polymerized. As shown in Chapter 2, these poly(PEGMA) films will not crystallize due to their relatively short PEO side chains. A catalyst prepared from CuBr, $CuBr_2$ and Me_4Cyclam was used for the polymerization of PEGMA(8-9). After a 10 min reaction, the membrane was removed from the reaction mixture, washed and dried. Figure 5.7 shows gas flux through a poly(PEGMA(8-9)) membrane. The H_2 gas flux increased linearly with the trans-membrane pressure, while CO_2 increased non-linearly, which suggests membrane plasticization. Considering the film thickness estimated from FESEM is 700 nm (see Figure 5.8), the CO_2 and H_2 permeabilities are ~35 and 4 Barrer,

respectively. The CO_2/H_2 selectivity of ~8 is good, but lower than measured for the previous polyPEGMA films. The decrease of CO_2 gas permeability is likely due to its decreased solubility in the film, since there are fewer ethylene oxide units in the polymer matrix. The H_2 gas permeability also decreased, and in this case, the decreased permeability is due to a decrease in gas diffusivity. Shorter PEO side chains results in more tightly packed polymer backbones, which affects the permeation of H_2. Decreased CO_2 permeability and CO_2/H_2 and CO_2/N_2 selectivity also were observed in poly(PEGMA(4-5)) films. The results are summarized in Table 5.3.

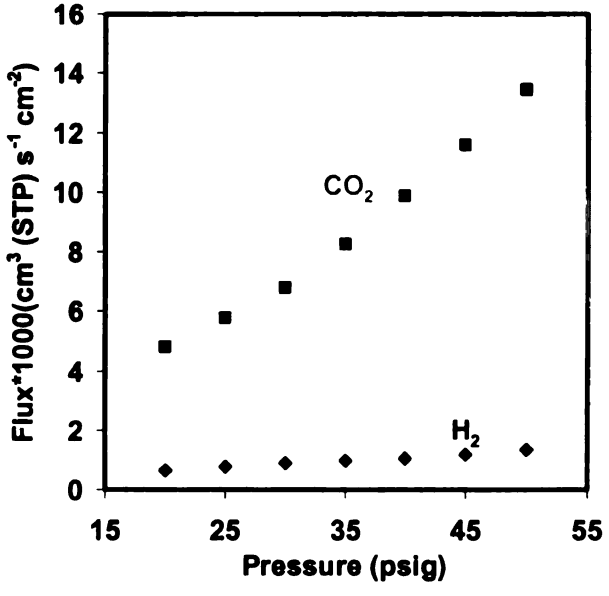

Figure 5.7. Single-gas fluxes of CO_2 and H_2 as a function of trans-membrane pressure drop for permeation through poly(PEGMA(8-9)) films prepared by polymerization from porous alumina.

(a)

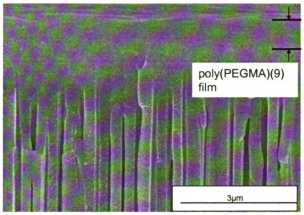

(b)

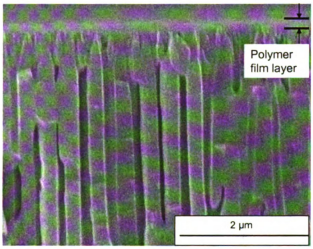

Figure 5.8. FESEM image of the filtrate side of porous alumina after growth of (a) poly(PEGMA(8-9)) and (b) poly(PEGMA(4-5)).

Number of EG units in poly(PEGMA) films	Thickness (nm)	Permeability coefficient (Barrer) [a]			Selectivity [b]	
		CO_2	H_2	N_2	CO_2/H_2	CO_2/N_2
4-5	150	13.6 ± 0.4	5.1	1.7 ± 0.4	2.6	8.9 ± 0.8
8-9	700	36 ± 2	4	N/A	8 ± 1	N/A
22-23	200	76	8.3	2	10	40
22-23	1000	280	20.4	N/A	14	N/A

[a] Permeability coefficients were calculated according to equation (5.1) and (5.3), and

1 Barrer = 10^{-10} cm^3 (STP) cm /(cm^2 s cm Hg). The listed values are the average of the permeability coefficients measured for two different membranes.

[b] The reported selectivities are the average values calculated from two different membranes.

Table 5.3. Summary of gas permeation through poly(PEGMA) films.

Pure gas permeation through crosslinked polymer films (poly(PEGMA-co-BisA-EDMA))

Another strategy for inhibiting crystallization is to use a crosslinked polymer network to frustrate crystallization. Therefore, PEGMA(22-23) was copolymerized with the BisA-EDMA crosslinker, with 30-100 mol% crosslinker in feed solution. The CO_2, H_2, and N_2 fluxes through different films were measured as a function of crosslinking, and are shown in Figure 5.9. FESEM images of a series of crosslinked films are shown in Figure 5.10.

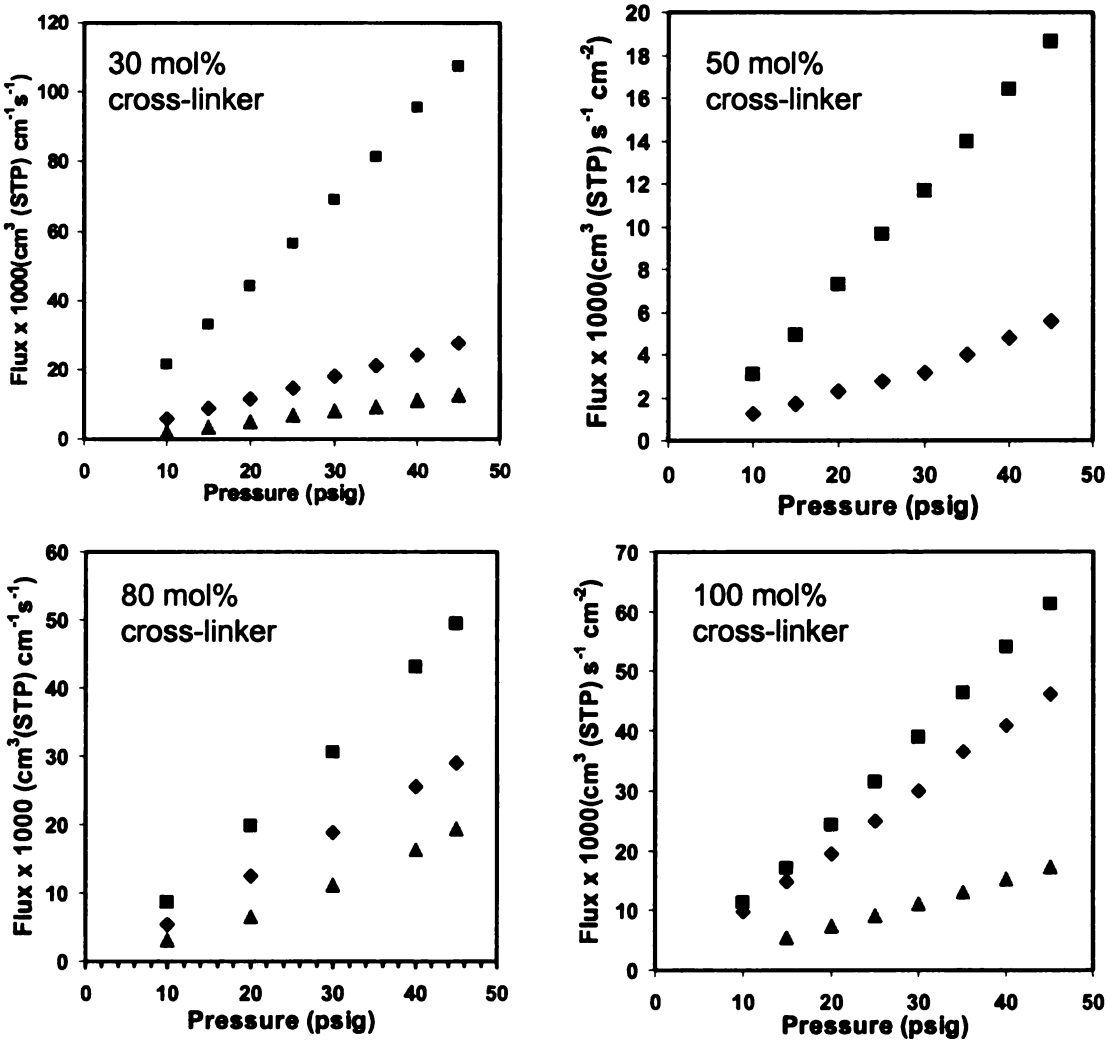

Figure 5.9. Single-gas fluxes of CO_2 (■), H_2 (♦) and N_2 (▲) through cross-linked *co*-polymer films prepared by polymerization of PEGMA(22-23) with a cross-linker (BisA-EDMA) from porous alumina as a function of trans-membrane pressure drop. For the film with 50 mol% crosslinker, the flow rate of N_2 is too low to be measured.

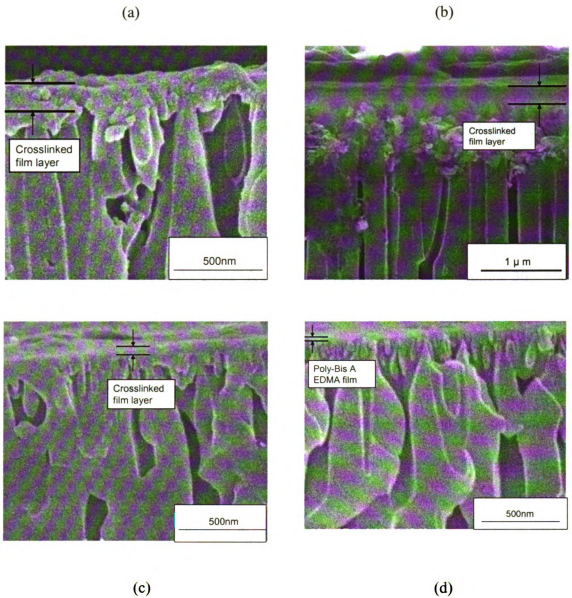

Figure 5.10. FESEM images (cross-sectional) of porous alumina (0.02 μm surface pore diameter) after growth of crosslinked films from BisA-EDMA and PEGMA(22-23). The monomer solution containing (a) 30 mol% crosslinker; (b) 50 mol% crosslinker; (c) 80 mol% crosslinker; and (d) 100 mol% crosslinker (a poly(BisA-EDMA) film).

The CO_2/H_2 and CO_2/N_2 selectivity were calculated from the gas permeability, the gas fluxes, and the film thickness estimated from FESEM images. The results, summarized in Table 5.4, show that the CO_2 permeability decreased from ~ 60 Barrer for the 30 mol% crosslinker film, to 6 Barrer for a 100 mol% BisA-EDMA film. The H_2 and N_2 gas permeabilities show the same trend. BisA-EDMA is approximately 78% ethylene oxide units by weight compared to 91 wt% ethylene oxide units in PEGMA(?-?). Therefore, increasing crosslinking decreases the ethylene oxide content in the polymer films, which decreases the CO_2 solubility in the polymer matrix. In addition, the gas permeability decreased as the crosslink density increased for films containing 30 – 100% BisA-EDMA. These data are somewhat surprising given the aqueous swelling experiments described in chapter IV, which showed that polymer swelling was independent of crosslink density when the BisA-EDMA was > 40%. Freeman and co-workers have pointed out that changes in gas diffusion and permeability in crosslinked polymer systems are more related to changes in the glass transition temperature (T_g) than crosslink density changes.[20] In the BisA-EDMA/PEGMA system, introduction of the crosslinker increased the polymer T_g due to the rigid benzene rings of BisA-EDMA, which likely reduced the free volume of the polymer, and hence affected the gas diffusion through the membrane.

Crosslinker in feed [a]	*Thickness(nm)*	*Calculated gas permeability coefficients (Barrer)* [b]			*Selectivity* [c]	
		CO_2	H_2	N_2	CO_2/H_2	CO_2/N_2
30 mol%	200	58 ± 8	21 ± 4	6.7 ± 0.6	3.2 ± 0.7	8.6 ± 0.2
50 mol%	300	24	7.2	N/A	3.2	N/A
80 mol%	50	9.5 ± 0.3	7.2 ± 1.1	4.5 ± 0.5	1.5 ± 0.3	2.4 ± 0.2
100 mol%	25	6.1	4.8	1.8	1.3	3.4

[a] Crosslinker (BisA-EDMA) mole percentage in the monomer feed solution used in co-polymerization with PEGMA(22-23).

[b] Permeability coefficients were calculated according to equation (5.1) &(5.3), and 1 Barrer = 10^{-10} cm^3 (STP) cm /(cm^2 s cmHg). Listed values are the average of the permeability coefficients measured for two different membranes.

[c] The reported selectivities are the average of the value calculated from two different membranes.

Table 5.4. Gas permeability coefficients and average selectivities for crosslinked poly(PEGMA-co-BisA-EDMA) membranes

The CO_2/H_2 selectivity also decreased as more crosslinker was incorporated in the film, from 3.2 for the polymer film containing 30 mol% crosslinker to about 1.3 for the BisA-EDMA film, which suggests a decrease in CO_2 solubility. The decreased film thickness may contribute to the decreased selectivity. Hirayama *et al.*[21] used plasma irradiation to prepare cross-linked polymer films from PEGMA and BisA-EDMA, and reported that CO_2 permeability decreased as the cross-linker content increased, but the selectivity of CO_2/N_2 remains unchanged. A polymer containing 70 wt% PEGMA exhibited a CO_2 permeability of 260 Barrers, and CO_2/N_2 selectivity of about 48, while poly(BisA-EDMA had a CO_2 permeability of 128 Barrer and a CO_2/N_2 selectivity of 49. However, the films were thick (μm scale), and FESEM images show that our crosslinked films (80 and 100 mol% crosslinker) were 25-50 nm. In these thin films, there may be defects or pinholes cause the decreased selectivity.

Summary

Comb and crosslinked PEO containing polymer brushes were grafted on the surface of porous alumina membrane support using surface-initiated ATRP, and used for the separation of CO_2 from light gases (H_2 and N_2). Preliminary results show that poly(PEGMA) films are promising for separation of CO_2 from light gases, with CO_2/H_2 selectivities as high as 14 and CO_2/N_2 selectivities about 40. Decreased CO_2 permeability and CO_2/H_2 selectivity were observed for membranes prepared from PEGMAs with shorter PEO side chains. The CO_2 permeability and CO_2/H_2 selectivity of crosslinked films prepared by copolymerization of PEGMA with a crosslinker (BisA-EDMA) decreased as the film crosslinking increased. The lower fraction of ethylene oxide units

in the films and an increase in the glass transition temperature with BisA-EDMA content may account for decreased permeability.

References:

1. Baker, R. W., *Membrane Technology and Applications, 2nd Ed.* J. Wiley: New York, 2004.

2. Ghosal, K.; Freeman, B. D., *Polym. Adv. Tech.* **1994,** *5*, 673-97.

3. Stern, S. A., *J. Membr. Sci.* **1994,** *94*, 1-65.

4. Petropoulos, J. H., *Polym. Gas Sep. Membr.* **1994,** 17-81.

5. Reid, R. C., Prausnitz, G. K., Poling, B.E., *The Properties od Gases and Liquids.* McGraw-Hill: New York, 1987.

6. Stannett, V. T., *Diffusion in Polymers.* Academic Press: New York, 1968.

7. Lin, H.; Freeman, B. D., *J. Membr. Sci.* **2004,** *239*, 105-117.

8. Lin, H. Q.; Freeman, B. D., *J. Molecul. Struc.* **2005,** *739*, 57-74.

9. Bondar, V. I.; Freeman, B. D.; Pinnau, I., *J. Polym. Sci. B: Polym. Phys.* **2000,** *38*, 2051-2062.

10. Bondar, V. I.; Freeman, B. D.; Pinnau, I., *J. Polym. Sci. B; Polym. Phys.* **1999,** *37*, 2463-2475.

11. Patel, N. P.; Zielinski, J. M.; Samseth, J.; Spontak, R. J., *Macromol. Chem. Phys.* **2004,** *205*, 2409-2419.

12. Patel, N. P.; Miller, A. C.; Spontak, R. J., *Adv. Func. Mater.* **2004,** *14*, 699-707.

13. Patel, N. P.; Miller, A. C.; Spontak, R. J., *Adv. Mater.* **2003,** *15*, 729-733.

14. Staudt-Bickel, C.; Koros, W. J., *J. Membr. Sci.* **1999,** *155*, 145-154.

15. Yanagishita, H.; Kitamoto, D.; Haraya, K.; Nakane, T.; Okada, T.; Matsuda, H.; Idemoto, Y.; Koura, N., *J. Membr. Sci.* **2001,** *188*, 165-172.

16. Hayakawa, Y.; Terasawa, N.; Hayashi, E.; Abe, T., *J. Applied. Polym. Sci.* **1996,** *62*, 951-954.

17. Ulbricht, M.; Belfort, G., *J. Membr. Sci.* **1996,** *111*, 193-215.

18. Kim, J. H.; Ha, S. Y.; Nam, S. Y.; Rhim, J. W.; Baek, K. H.; Lee, Y. M., *J. Membr. Sci.* **2001,** *186*, 97-107.

19. Pieracci, J.; Crivello, J. V.; Belfort, G., *Chem. Mater.* **2002,** *14*, 256-265.

20. Lin, H. Q.; Freeman, B. D., *Macromolecules* **2005,** *38*, 8394-8407.

21. Hirayama, Y.; Kase, Y.; Tanihara, R.; Sumiyama, Y.; Kusuki, Y.; Haraya, K., *J. Membr. Sci.* **1999,** *160*, 87-99.